

# Development of high performance vinyl acetate monomer (VAM) catalysts

Vom Fachbereich Chemie  
der Technischen Universität Darmstadt

zur Erlangung des akademischen Grades eines

Doktor-Ingenieurs (Dr.-Ing.)

genehmigte

Dissertation

vorgelegt von

Dipl.-Ing. Alice Kyriopoulos

aus Darmstadt

Referent: Prof. Dr. rer. nat. habil. Peter Claus

Korreferent: Prof. Dr. rer. nat. habil. Markus Busch

Tag der Einreichung: 19. Oktober 2009

Tag der mündlichen Prüfung: 14. Dezember 2009

Darmstadt 2009



Πάντες ἄνθρωποι τοῦ εἰδέναι ὀρέγονται φύσει.

Ἀριστοτέλης (384 - 322 π.Χ.)  
[Μεταφυσικά, Βιβλίο Α 980α, 21]

# Acknowledgements

I would like to express my gratitude to Prof. Dr. rer. nat. habil. Peter Claus (Ernst-Berl-Institute for Technical and Macromolecular Chemistry, Technische Universität Darmstadt) for his supervision during my Ph. D. studies at Darmstadt. His group members are also kindly acknowledged for being generally helpful.

Furthermore, I acknowledge Süd-Chemie AG for having provided the fundings and analytical equipment, *i. a.* for wet chemical analysis, XRD and SEM-EDX during my research studies. Special thanks go to Dr. Alfred Hagemeyer for his support in scientific issues and all friendly colleagues.

Thanks also to Dr. Stefan Lauterbach (Institute for Applied Geosciences, Technische Universität Darmstadt) for his help to use EDX as a characterisation method.

Grateful thanks to Dr.-Ing. Christina Roth and her group (Institute for Materials Science, Technische Universität Darmstadt) for their assistance in TEM. Thank you especially for having given me the opportunity to accomplish EXAFS experiments at HASYLAB. In this context I would like to mention also Adam Webb, thanking him for his guidance through these experiments.

## Abstract

---

The focus of this study was to develop high performance catalysts for the synthesis of vinyl acetate monomer (VAM). By systematic variation of different preparation parameters a multitude of shell catalysts consisting of PdAu nanoparticles supported on a bentonite carrier was explored. In order to investigate the influence of these alterations on catalytic performance, a catalyst classification was accomplished in a high-throughput Temkin test unit by comparison with a highly efficient commercial benchmark, referred to as *B*. Due to the applied Temkin reactor concept efficient heat and mass transport was ensured. Thus, the prepared catalysts could be clearly distinguished with regard to their selectivity ( $\pm 0.25\%$ ) and space time yield ( $\pm 5\%$ ) within a wide range of values. Catalyst performances for the selective oxidation of ethylene and acetic acid to VAM revealed that samples synthesised in this study are able to compete with this state-of-the-art plant catalyst. Concerning the selectivity meaningful improvements of almost  $3\%$  were achieved by catalysts based on different KA-Zr carriers (Zr doped bentonite). Gas phase reduction (GPR) at various temperatures was also identified as a promising synthesis step. Although catalysts produced by liquid phase reduction (LPR) achieved on average about  $11\%$  higher activity (*STY*) than the internal standard, outstanding enhancements of up to approximately  $40\%$  were attained via forming gas reduction. A challenging aim of this thesis can be attributed to the characterisation of VAM catalysts. In view of the fact that the most significant differentiation in performance was observed between catalysts prepared using LPR and GPR, samples from each reduction medium were chosen for a detailed characterisation using XRD, TEM and EXAFS. However, high amounts of carrier components compared to low metal concentrations of approximately  $1\text{--}2\text{ wt}\%$  rendered analysis of VAM catalysts with well-established techniques such as XRD and EDX difficult. Valuable information about the local Pd and Au distribution was provided by EXAFS. In agreement with TEM characterisation and Pd dispersion measurements, larger particle sizes were found for the liquid phase reduced catalyst *B* compared to GPR samples processed at  $150^\circ\text{C}$  and  $250^\circ\text{C}$ , respectively. Furthermore, TEM analysis showed that nanoparticles of LPR tend to agglomerate to chain-like framework structures, whereas a distribution of small and isolated particles dominates the GPR catalysts, correlating with the observed higher activity.

---

## Zusammenfassung

---

Das Ziel dieser Arbeit war die Entwicklung von Hochleistungskatalysatoren für die Synthese von Vinylacetatmonomer (VAM). Mittels systematischer Variation verschiedener Herstellungsparameter wurde eine Vielzahl an Schalenkatalysatoren, bestehend aus PdAu-Nanopartikeln auf Bentonitträgern, untersucht. Durch Vergleich derselben mit einem aktuellen kommerziellen Standard, bezeichnet als *B*, konnte in einer Temkin-Hochdurchsatz-Testanlage der Einfluss der Präparationsvariablen auf das katalytische Potenzial festgestellt werden. Aufgrund des angewandten Temkin-Reaktorkonzeptes wurden effizienter Wärme- und Stofftransport sicher gestellt. Dies ermöglichte eine eindeutige Differenzierung der synthetisierten Katalysatoren in Hinsicht auf deren Selektivität ( $\pm 0.25\%$ ) und Raum-Zeit-Ausbeute ( $\pm 5\%$ ) innerhalb eines großen Wertebereiches. Tests der Katalysatoren bei der selektiven Oxidation von Ethylen und Essigsäure zu VAM zeigten, dass die in dieser Arbeit synthetisierten Exemplare mit der industriellen Produktionsreferenz konkurrieren können. Bezüglich der Selektivität wurden signifikante Verbesserungen von nahezu  $3\%$  für Katalysatoren basierend auf verschiedenen KA-Zr Trägern (Zr-dotierter Bentonit) erreicht. Weiterhin konnte die Gasphasenreduktion (GPR) bei verschiedenen Temperaturen als vielversprechende Synthesevariante identifiziert werden. Obgleich in der Flüssigphase reduzierte (LPR) Katalysatoren durchschnittlich ungefähr  $11\%$  höhere Aktivitäten (Raum-Zeit-Ausbeute) erzielten als der interne Standard, so wurden hervorragende Steigerungen bis nahezu  $40\%$  mittels GPR realisiert. Eine große Herausforderung dieser Arbeit bestand in der Charakterisierung der VAM-Katalysatoren. Da die größten Unterschiede in den katalytischen Eigenschaften zwischen LPR und GPR beobachtet wurden, sind jeweils Proben zur detaillierten Charakterisierung mittels XRD, TEM und EXAFS untersucht worden. Doch hohe Trägermengen verglichen zu niedrigen Metallkonzentrationen von ungefähr  $1\text{--}2\text{ Gew.}\%$  erschwerten hierbei die Analyse der VAM-Katalysatoren mittels XRD und EDX. EXAFS erwies sich als vielversprechende Methode, da wertvolle Informationen zur Aufklärung der lokalen Verteilung von Pd und Au gewonnen werden konnten. In Übereinstimmung mit TEM-Untersuchungen und Pd-Dispersionsmessungen wurden größere Partikel für den in der Flüssigphase reduzierten Katalysator *B* nachgewiesen im Vergleich zu den bei  $150\text{ }^{\circ}\text{C}$  beziehungsweise  $250\text{ }^{\circ}\text{C}$  hergestellten Proben der GPR. Ferner zeigten TEM-Analysen, dass Nanopartikel in der LPR zur Agglomeration tendieren, was in kettenförmigen Strukturen resultiert. Dagegen dominiert im Falle von GPR eine feine Verteilung kleiner isolierter Partikel, was in direktem Zusammenhang mit der gemessenen höheren Aktivität steht.

---

This thesis was carried out in collaboration with Süd-Chemie AG under the supervision of Professor Dr. rer. nat. habil. Peter Claus from the Ernst-Berl-Institute for Technical and Macromolecular Chemistry, University of Darmstadt, from December 2006 until June 2009.

Parts of this dissertation have been already published, presented in conferences or are associated with patent applications:

#### *Patents and patent applications*

- A. Hagemeyer, A. Kyriopoulos, S. Obermaier (Inventor status recognised after publication; Süd-Chemie AG), Method for producing a shell catalyst using a base or acid mixture, DE 102007025324 A1, **2008** and WO 08151731 A1, **2008**.
- A. Hagemeyer, A. Kyriopoulos, G. Mestl, P. Scheck (Süd-Chemie AG), VAM shell catalyst, method for producing the same and use thereof, DE 102007025444 A1, **2008** and WO 08145389 A2, **2008**.
- A. Hagemeyer, A. Kyriopoulos, G. Mestl, P. Scheck (Süd-Chemie AG), “Katalysatorträger, Verfahren zu seiner Herstellung sowie dessen Verwendung”, German patent application pending.
- E. Haberkorn, K. H. Hable, A. Hagemeyer, R. Kerscher, A. Kyriopoulos, P. Scheck (Süd-Chemie AG), “Mesoporöser und essigsäureresistenter KA-Zr-Träger”, German patent application pending.
- A. Hagemeyer, A. Kyriopoulos, G. Mestl, S. Neumann, P. Scheck (Süd-Chemie AG), “Schalenkatalysator, Verfahren zu seiner Herstellung sowie Verwendung”, German patent application pending.

#### *Poster presentation*

- T. Schulz, A. Kyriopoulos, M. Lucas, P. Claus: “Laborreaktor für die Untersuchung von Gasphasenreaktionen industrieller Katalysatoren in Originalgröße” in *42. Jahrestreffen Deutscher Katalytiker*, Weimar, Germany, **2009**, 101-102.
- T. Schulz, A. Kyriopoulos, M. Lucas, A. Hagemeyer, G. Mestl, P. Claus: “Laboratory reactor for studying gas-phase reactions of real-size industrial catalysts” in *EuropaCat IX*, Salamanca, Spain, **2009**, 258.

#### *Oral presentation*

- T. Schulz, A. Kyriopoulos, M. Lucas, A. Hagemeyer, G. Mestl, P. Claus: “Laborreaktor zur Untersuchung von Gasphasenreaktionen intakter Katalysatorformlinge” in *Jahrestreffen Reaktionstechnik 2009*, Würzburg, Germany, **2009**, 32-33.

# Table of Contents

<b>1</b>	<b>State of the Art</b>	<b>1</b>
<b>2</b>	<b>Aims and Approaches</b>	<b>9</b>
<b>3</b>	<b>Experimental procedures</b>	<b>13</b>
3.1	Synthesis sequence of VAM catalysts . . . . .	13
3.2	Parameter variation of proprietary synthesis recipes . . . . .	18
3.2.1	Carrier selection . . . . .	18
3.2.1.1	Low specific surface support (KA 0) . . . . .	22
3.2.1.2	Zr-based KA carriers . . . . .	23
3.2.2	Precipitation with base mixtures . . . . .	25
3.2.3	Liquid phase versus gas phase reduction . . . . .	26
3.3	Scale-up of laboratory synthesis . . . . .	28
3.4	Method development for precious metal analysis . . . . .	31
3.5	VAM-Temkin test unit . . . . .	33
<b>4</b>	<b>Performance results and data reduction</b>	<b>38</b>
4.1	Catalyst screening . . . . .	38
4.2	Characterisation of VAM catalysts . . . . .	47
4.2.1	Wet chemical analysis (ICP-OES, AAS) . . . . .	47
4.2.2	Optical microscopy . . . . .	51
4.2.3	CO chemisorption . . . . .	55
4.2.4	BET measurements . . . . .	57
4.2.5	X-ray powder diffraction (XRD) . . . . .	57
4.2.6	Energy dispersive X-ray spectroscopy (EDX) . . . . .	65
4.2.7	Scanning electron microscopy (SEM)-EDX mapping . . . . .	67
4.2.8	Transmission electron microscopy (TEM) . . . . .	72
4.2.9	Extended X-ray absorption fine structure spectroscopy (EXAFS) . . . . .	78
4.3	Summary of results . . . . .	90
<b>5</b>	<b>Final discussion</b>	<b>91</b>
<b>6</b>	<b>Outlook</b>	<b>99</b>
<b>7</b>	<b>References</b>	<b>103</b>
	<b>Appendices</b>	<b>110</b>

# List of Figures

1.1	Schematic comparison of palladium monomer pairs in different atomic configurations for VAM synthesis. . . . .	3
2.1	Motivation of this work schematically summarised in form of pillars. . .	10
3.1	Schematic overview of unit operations for VAM catalyst synthesis via IW method. . . . .	14
3.2	Progress of impregnation by adding carrier spheres which continuously absorb the noble metal solution. . . . .	15
3.3	Conversion of noble metals to corresponding hydroxides. . . . .	15
3.4	Liquid phase reduction of metal hydroxides to metallic state with simultaneous formation of hydrogen. . . . .	16
3.5	Gas phase reduction furnace used for conversion of noble metal hydroxides to the metallic state. . . . .	16
3.6	Closed loop flow system pumping double distilled water through the catalyst precursor in order to wash out chlorides. . . . .	17
3.7	Time saving fluidised-bed dryer used for VAM catalyst synthesis. . . .	18
3.8	Molecular structure of montmorillonite. . . . .	19
3.9	Pore diameter distribution via BJH method for different KA carriers at 77.15 K and an equilibration interval of 20 s. . . . .	21
3.10	Shell formation for different stoichiometric excesses of NaOH. . . . .	25
3.11	Temperature control for gas phase reduction of catalyst <i>EX8139</i> by measurements at different oven positions. . . . .	31
3.12	Design of modules used in the TUD reactor. . . . .	34
3.13	Flow chart of VAM-Temkin test unit. . . . .	36
3.14	Start-up protocol for flows during test procedure to evaluate different VAM catalysts. . . . .	37
4.1	Comparison of VAM selectivity at varying temperatures for the liquid phase reduced catalysts with different NaOH/Na <sub>2</sub> SiO <sub>3</sub> mixtures as precipitating agent, studied at a reactor flow of 250 NmLmin <sup>-1</sup> and a pressure of 8 bar. The selectivity data of the benchmark <i>B</i> is also shown for this test library. . . . .	39
4.2	Comparison of VAM selectivity for several gas phase reduced catalysts using reduction temperature variation. The selectivity data of the benchmark <i>B</i> is also shown. . . . .	40
4.3	Experimental data set of selectivity for catalyst <i>EX6152</i> . According to the linear fit a VAM selectivity of 95.62 % is obtained at 50 % O <sub>2</sub> conversion. . . . .	41

4.4	Comparison of selectivity at 50 % O <sub>2</sub> conversion for all synthesised catalysts relative to the benchmark <i>B</i> . . . . .	42
4.5	Comparison of activity for the liquid phase reduced catalysts with different NaOH/Na <sub>2</sub> SiO <sub>3</sub> mixtures as precipitating agent. The <i>STY</i> data of the benchmark <i>B</i> used in this test library is also shown. . . . .	44
4.6	Comparison of activity for several gas phase reduced catalysts using reduction temperature variation. The <i>STY</i> data of the benchmark <i>B</i> is also shown. . . . .	45
4.7	<i>STY</i> comparison relative to the reference <i>B</i> measured at 145 °C process temperature. . . . .	46
4.8	Images of catalyst hemispheres for a) <i>B</i> and b) <i>EX8082</i> showing that too high concentrations of Zr in the carrier impair shell formation. . . .	53
4.9	Influence of structural dimensions of the base on shell thickness illustrated for NaOH and Na <sub>2</sub> SiO <sub>3</sub> . . . . .	54
4.10	Silicon monocrystal purchased by Bruker for holding the sample without self-generated reflections during analysis. . . . .	58
4.11	XRD data obtained from fresh catalysts <i>B<sub>f</sub></i> (blue) and <i>EX7273<sub>f</sub></i> (red) for 2θ range of 5-70°. . . . .	59
4.12	Identification of reflections for XRD pattern of fresh catalyst <i>B<sub>f</sub></i> . . . .	59
4.13	Identification of reflections for XRD pattern of fresh catalyst <i>EX7273<sub>f</sub></i> . . .	60
4.14	XRD pattern resulting from VAM catalyst carrier KA 160 lot 7073. . .	61
4.15	Identification of reflections for XRD pattern of catalyst <i>B<sub>f</sub></i> after subtraction of carrier profile. . . . .	61
4.16	Identification of reflections for XRD pattern of catalyst <i>EX7273<sub>f</sub></i> after subtraction of carrier profile. . . . .	62
4.17	Identification of reflections for XRD pattern of spent catalyst <i>B<sub>s</sub></i> . . . .	63
4.18	Identification of reflections for XRD pattern of spent catalyst <i>EX7273<sub>s</sub></i> . . .	63
4.19	XRD patterns of fresh and spent catalysts for species <i>B</i> and <i>EX7273</i> : <i>EX7273<sub>s</sub></i> (magenta), <i>EX7273<sub>f</sub></i> (red), <i>B<sub>s</sub></i> (turquoise) and <i>B<sub>f</sub></i> (blue). . . .	64
4.20	EDX analysis for different locations on catalyst <i>B</i> (left) and their corresponding spectra (right). . . . .	66
4.21	SEM-EDX mapping indicating the distribution of elements throughout the catalyst shell for <i>EX7804</i> . . . . .	68
4.22	Influence of Zr concentration in the carrier on distributions of Pd, K and Au. . . . .	70
4.23	Influence of the precipitating agent on Pd, K and Au dispersion. . . .	70
4.24	Distribution of Pd, K and Au for catalysts reduced in liquid and gas phases. . . . .	71
4.25	TEM images for fresh catalyst <i>B<sub>f</sub></i> reduced in liquid phase. . . . .	72
4.26	Particle size distribution of catalyst <i>B<sub>f</sub></i> . . . . .	73
4.27	TEM images for fresh catalyst <i>EX7273<sub>f</sub></i> reduced at 150 °C in gas phase. . .	74
4.28	TEM images for fresh catalyst <i>EX7275<sub>f</sub></i> reduced at 250 °C in gas phase. . .	74
4.29	Particle size distributions of gas phase reduced catalysts <i>EX7273<sub>f</sub></i> and <i>EX7275<sub>f</sub></i> . . . . .	74
4.30	Particle morphologies for catalysts a) <i>B<sub>f</sub></i> and b) <i>EX7273<sub>f</sub></i> reduced in different media. . . . .	75

4.31	Representative micrographs for the spent catalyst $B_s$ . . . . .	76
4.32	Particle size distribution of the spent catalyst $B_s$ . . . . .	76
4.33	Representative micrographs for the spent catalyst $EX7273_s$ . . . . .	77
4.34	Particle size distribution of the spent catalyst $EX7273_s$ . . . . .	77
4.35	Different structures for bimetallic PdAu nanoparticles: Core-shell (left) and 3:1 alloy (right). . . . .	79
4.36	Experimental setup for EXAFS measurements in transmission mode using a Pd or Au foil as reference. . . . .	79
4.37	Normalised absorption spectra of catalysts $B$ (blue), $EX7273$ (green) and $EX7275$ (red) for the Au $L_3$ edge at 11.919 keV. . . . .	80
4.38	Normalised absorption spectra of catalysts $B$ (blue), $EX7273$ (green) and $EX7275$ (red) for the Pd $K$ edge at 24.350 keV. . . . .	81
4.39	Transmission EXAFS spectra $k\chi(k)$ of studied catalysts $B$ (blue), $EX7273$ (green) and $EX7275$ and the Pd reference foil. . . . .	82
4.40	Fourier transforms $ \chi(R) $ of $k^3\chi(k)$ for catalysts $B$ (blue), $EX7273$ (green) and $EX7275$ (red) with regard to the Au edge. . . . .	83
4.41	Fourier transforms $ \chi(R) $ of $k^3\chi(k)$ for catalysts $B$ (blue), $EX7273$ (green) and $EX7275$ (red) with regard to the Pd edge. . . . .	84
4.42	Refined EXAFS function (red) and calculated model (black) for catalyst $EX7275$ achieved by modulation in $k$ space with regard to the Au edge. . . . .	85
4.43	Structural difference between the three catalysts determined by EXAFS analysis. . . . .	89
5.1	Model of structural arrangement in the case of the benchmark synthesised by LPR. . . . .	96
6.1	SEM-EDX mapping indicating the distribution of elements in the catalyst shell for a sample synthesised by coating. . . . .	101
6.2	SEM-EDX mappings for catalysts synthesised via a) IW method and b) coating technology, indicating different Pd distributions in the shell. . . . .	101
A.1	Exemplary chromatogram of the detected components for the VAM reaction. . . . .	110
B.1	Comparison of selectivity between the VAM catalyst $EX7307$ based on the KA 0 carrier ( $BET = 106 \text{ m}^2\text{g}^{-1}$ ) and the reference $B$ synthesised with the higher surface area support KA 160 ( $BET = 161 \text{ m}^2\text{g}^{-1}$ ). . . . .	112
B.2	VAM selectivity for several catalysts synthesised with different KA-Zr carriers compared to the performance of benchmark $B$ . . . . .	113
B.3	Comparison of selectivity for VAM catalysts precipitated with NaOH or $\text{Na}_2\text{SiO}_3$ using GPR during synthesis. The selectivity data of the benchmark $B$ is also shown. . . . .	114
B.4	VAM selectivity of catalysts reduced at different temperatures in gas phase compared to the corresponding data of benchmark $B$ . . . . .	115
C.1	Comparison of activity between the VAM catalyst $EX7307$ based on KA 0 carrier and the reference $B$ . . . . .	116
C.2	VAM $STY$ for catalysts synthesised with different KA-Zr carriers compared to the performance of benchmark $B$ . . . . .	117

C.3	Comparison of activity for VAM catalysts precipitated with NaOH or Na <sub>2</sub> SiO <sub>3</sub> using GPR during synthesis. The activity data of the benchmark <i>B</i> is also shown. . . . .	118
C.4	VAM <i>STY</i> comparison of catalysts reduced at different temperatures in gas phase to the corresponding data of benchmark <i>B</i> . . . . .	119

# List of Tables

3.1	KA 160 and KA 0 carriers for VAM catalyst synthesis, produced by SCAG Moosburg. . . . .	20
3.2	Average pore diameters obtained by BJH method for lots 7073 and 6599 of carrier KA 160 and lot 1812 of KA 0. . . . .	21
3.3	Compounds for VAM catalyst synthesis based on charge 1812 of KA 0 carrier; all net weights are represented in g. . . . .	22
3.4	Parameters for VAM catalyst synthesis based on charge 1812 of KA 0 carrier. . . . .	23
3.5	KA-Zr supports for VAM catalyst preparation produced by SCAG Moosburg. . . . .	23
3.6	Compounds for VAM catalyst synthesis based on different KA-Zr carriers; all net weights are represented in g. . . . .	24
3.7	Parameters for VAM catalyst synthesis based on different KA-Zr carriers. . . . .	24
3.8	Compounds for VAM catalyst synthesis based on different base mixtures in the precipitation step; all net weights are represented in g. . . . .	26
3.9	Parameters for VAM catalyst synthesis based on different base mixtures in the precipitation step. . . . .	27
3.10	Compounds for VAM catalyst synthesis based on GPR using different bases in the precipitation step; all net weights are represented in g. . . . .	27
3.11	Parameters for VAM catalyst synthesis based on GPR using different bases in the precipitation step. . . . .	28
3.12	Compounds for VAM catalyst plant trials <i>B</i> and <i>D</i> based on different reduction media; all net weights are represented in kg. . . . .	30
3.13	Temperature variation for GPR of <i>D</i> catalysts. . . . .	30
4.1	Average results of absolute selectivity calculated at 50 % O <sub>2</sub> conversion for catalysts of the base mixture series and the reference <i>B</i> including a relative comparison of these values. . . . .	41
4.2	Averaged absolute <i>STY</i> results measured at 145 °C process temperature for catalysts of the base mixture series and the applied benchmark <i>B</i> including their relative comparison. . . . .	45
4.3	Analytical results for <i>EX7307</i> based on KA 0 carrier compared to the reference <i>B</i> . . . . .	48
4.4	Analytical results for VAM catalysts with different KA-Zr carriers as support. . . . .	49
4.5	Analytical results of VAM catalysts synthesised with base variations. . . . .	50
4.6	Analytical results of VAM catalysts reduced in gas phase using different bases. . . . .	50

4.7	Analytical results for VAM catalysts obtained by plant certification trials, varying in reduction medium and temperature. . . . .	51
4.8	Comparison of shell thicknesses for VAM catalysts based on KA 0 and KA 160 carrier. . . . .	52
4.9	Shell thicknesses for VAM catalysts synthesised with different KA-Zr supports. Samples with blurred shells are displayed in red colour. . . .	53
4.10	Shell thicknesses for VAM catalysts using different NaOH/Na <sub>2</sub> SiO <sub>3</sub> mixtures and LPR. . . . .	53
4.11	Shell thicknesses for VAM catalysts synthesised via GPR and diverse bases. . . . .	55
4.12	Shell thicknesses for VAM catalysts obtained by plant certification trials, varying in reduction medium. . . . .	55
4.13	Measured Pd dispersion $D_{Pd}$ and resulting mean particle size $d$ for different base mixtures and variation in reduction medium. . . . .	56
4.14	BET surface areas for the carrier of benchmark $B$ synthesised by LPR, differing between the fresh and spent sample; all BET values are represented in [m <sup>2</sup> g <sup>-1</sup> ]. . . . .	57
4.15	Simulation parameters using a constant Debye-Waller factor $\Delta\sigma^2$ for the obtained EXAFS data of catalysts $B$ , $EX7273$ and $EX7275$ . . . . .	86
4.16	Debye-Waller factors $\Delta\sigma^2$ for different pairs of calculated model systems; the error is estimated to be $\pm 5\%$ . . . . .	86
4.17	Alternative parameters resulting from simulations with Pd-Au as additional scattering path for the obtained EXAFS data of catalysts $B$ . . .	88
4.18	Representative comparison between distances $R$ obtained by EXAFS model fitting and values of literature; all results are represented in Å. .	88
4.19	Main differences in performance and further characteristics of catalysts produced via LPR and GPR. . . . .	90
A.1	GC peak areas measured for VAM catalyst $EX6315$ and for the inert material. . . . .	111
A.2	GC peak areas normalised to methane. . . . .	111

# Abbreviations

AAS	Atomic absorption spectrometry
<i>B</i>	Benchmark
BET	Brunauer, Emmett, Teller
BJH	Barrett, Joyner, Halenda
<i>C</i>	Conversion
DESY	Deutsches Elektronen-Synchrotron
<i>Dev</i>	Deviation
DFT	Density functional theory
EDX	Energy dispersive X-ray spectroscopy
EXAFS	Extended X-ray absorption fine structure
<i>F</i>	Flow rate
FT	Fourier transformation
FWHM	Full width at half maximum
GC	Gas chromatography
GOF	Goodness of fit
GPR	Gas phase reduction
HASYLAB	Hamburger Synchrotronstrahlungslabor
HREM	High resolution electron microscopy
ICDD	International Centre for Diffraction Data
ICP-OES	Inductively coupled plasma optical emission spectrometry
IR	Infrared
IW	Incipient wetness
LOI	Loss on ignition
LPR	Liquid phase reduction
<i>N</i>	Coordination number
<i>R</i>	Interatomic distance
<i>S</i>	Selectivity
SEM	Scanning electron microscopy
STEM	Scanning transmission electron microscopy
<i>STY</i>	Space time yield
TEM	Transmission electron microscopy
VAM	Vinyl acetate monomer
XRD	X-ray diffraction

# Chapter 1

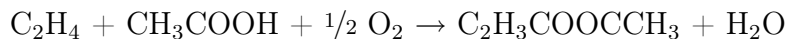
## State of the Art

Vinyl acetate monomer (VAM) has attracted enormous interest over the last few decades as a chemical intermediate for the production of various polymers, such as polyvinyl acetate and polyvinyl alcohol used in adhesives, lacquers and laminate films. The global production of VAM was about five million tonnes in 2003 [1]. Since then purchasing of VAM has considerably increased. Economic evaluations in 2008 revealed a price of approximately 1,500 euros per tonne [2].

In the 1930's the traditional procedure of industrial VAM synthesis was based on gas phase conversion of acetylene and acetic acid over a carbon supported zinc acetate catalyst. Since the discovery of the Wacker process by Smidt *et al.* [3], Moiseev and co-workers [4] extended this operation to make VAM by employing ethylene and acetic acid catalysed via palladium salts. Due to this novel approach, acetylene has increasingly been replaced by the corresponding and economically more favourable alkene.

In the same era, apart from the homogeneous liquid phase technique also described in [5], synthesis was already alternatively realised in the gas phase by acetoxylation of ethylene with acetic acid and oxygen. In 1968 heterogeneously catalysed conversion to VAM was concurrently developed by Hoechst [6] and Bayer [7] over palladium based catalyst species. Varying in components and preparation methods, the catalysts designed by Hoechst arose from impregnating a spherical silica support of 5 mm in diameter with palladium, cadmium and potassium acetates. According to US patent 3,658,888 [8], acetate of palladium was reduced in a second step to its metallic state. In

contrast to this synthesis method, Bayer and later on Du Pont [9] created shell catalyst spheres applying palladium and gold chlorides with subsequent reduction followed by impregnation of the entire catalyst precursor with potassium acetate. The commercial process to produce VAM via gas phase acetoxylation of ethylene is outlined below:



For both of the previously mentioned reaction phases a form of palladium acetate represents the active catalytic component [10, 11]. Shetty *et al.* [12] compared the effect of acetates of lithium, sodium and potassium on the reaction rate of VAM. They observed that VAM formation did not occur for the first promoter. However, significant improvement was revealed for potassium acetate, also in contrast to sodium as the promoting alkali metal.

Furthermore, journal and patent literature show that gold as an additive improves the intrinsic selectivity of VAM catalysts [13], resulting in an increase of the production rate [14]. Preparing palladium and palladium-gold alloy catalysts on high surface area silica, Han *et al.* [15] discovered highly dispersed, surface gold enriched alloy particles via transmission electron microscopy including energy dispersive X-ray spectroscopy (TEM-EDS) and by X-ray diffraction (XRD). Variations in adsorption data were assigned to decreasing ethylene coverage for alloy catalysts. A coexisting increase in surface capacity for oxygen was therefore proposed to be responsible for the reactivity in these bimetallic catalysts. Due to the improved properties after addition of gold to palladium catalysts for VAM synthesis, modification of electronic configuration as well as geometric effects were assumed to influence catalyst performance [16]. For instance, enhancements in selectivity of 94 % and two times higher VAM formation rate could be achieved compared to the gold absent analogue. Here a silica supported palladium-gold catalyst was used. The surface composition of the bimetallic system was studied by low energy ion scattering spectroscopy (LEISS), confirming the preferential surface enrichment in gold [17, 18]. This element plays an important role in isolating the palladium sites in order to facilitate the coupling of surface species forming VAM. Hence, addition of gold could improve catalytic selectivity by inhibiting undesirable by-products like carbon monoxide and dioxide, as well as surface carbon.

Comparing atomic configurations of palladium substituents on Au(100) and Au(111) surfaces, VAM formation preferentially occurs in the first system [19]. The distance between two palladium atoms in a monomer pair calculated for Au(100) ( $4.08 \text{ \AA}$ ) is assumed to be favoured compared to a couple of Pd monomers in Au(111) ( $4.99 \text{ \AA}$ ), shown in figure 1.1. Since the optimum distance between two active centers was estimated to be  $3.3 \text{ \AA}$ , the coupling of ethylene and acetate surface species only occurred for the lower distance in case of Pd on Au(100).

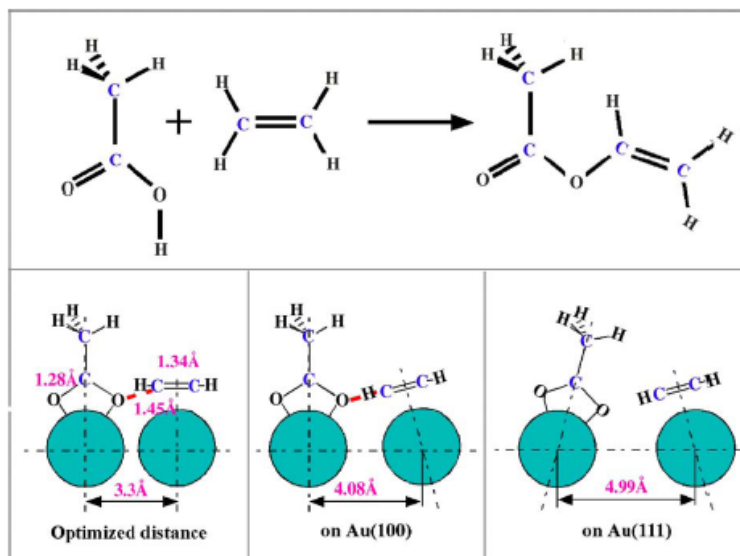


Figure 1.1: Schematic comparison of palladium monomer pairs in different atomic configurations for VAM synthesis [19].

The geometric effect of these bimetallic surfaces was investigated via density functional calculations by Gotsis *et al.* [20]. It was found that palladium second neighbours existed rather than first neighbours on both surfaces, due to a lower ensemble formation energy. Provine *et al.* [21] also studied the effect of gold and potassium acetate on the performance of VAM catalysts. Considering four different catalyst systems (Pd; Pd, Au; Pd, KOAc; Pd, Au, KOAc), they confirmed the enhancement of both VAM formation and desorption rates. Moreover, the ability of potassium acetate to keep acetic acid on the catalyst surface was highlighted in that paper. This conclusion supported previous observations from isotopic transient kinetic experiments carried out by Crathorne *et al.* [22]. They reported that potassium acetate promotes formation of an about three monolayers thick liquid film of acetic acid and water, enabling high

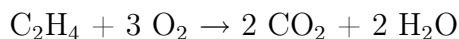
Pd-OAc surface coverage. Temperature programmed desorption (TPD) experiments also proved that acetic acid retention is not only influenced by potassium acetate, but also by palladium loadings and surface area respectively. The role of a silica supported Pd-Au-KOAc catalyst to manufacture VAM was schematically summarised in [21].

Two distinctive mechanisms are proposed for the palladium based synthesis of VAM in the gas phase. The first, suggested by Nakamura and Yasui [10, 23] as well as Moiseev *et al.* [24], assumes that palladium remains in its metallic state providing adsorption sites for the feed components to form VAM. Ethylene, vinyl and acetate moieties and finally VAM are expected to be present on the palladium surface. In this process activation of the C-H bond in ethylene is part of the rate limiting step, followed by rapid reaction of the vinyl intermediate with acetic acid to give the favoured product. Contrary to this mechanistic scheme, scientists like Samanos *et al.* [25], Zaidi [26] and van Helden *et al.* [27] propose that palladium exists throughout the reaction in terms of alkali metal acetate complexes. According to this mechanism, coordinated ethylene is inserted into the Pd-OAc bond followed by decomposition of these complexes to form VAM and palladium metal. In this case, simultaneously occurring ethylene insertion and  $\beta$  C-H bond activation are both proposed as rate limiting. The two reaction pathways of this mechanism are assumed to occur consistent with the established homogeneous system [28]. While evidence for both sequences exists, some effort was made to reveal the predominant nature of the reaction pathways via density functional theory (DFT). Rate determining elementary steps were calculated by Neurock *et al.* [29] for small homogeneous  $\text{Pd}^{2+}$  and for larger  $\text{Pd}^0$  clusters, represented by  $\text{Pd}_3\text{O}_3$  and  $\text{Pd}_{18}$  cluster models. As concluded from these results, the most endothermic paths are assigned to ethylene insertion and C-H bond activation. Another approach using isotopically labeled reactants to identify the mechanism for VAM formation was presented by Stacciola *et al.* [30]. A series of infrared (IR) spectra on a Pd(111) surface provided clear evidence of an acetoxylethyl-palladium intermediate, which can only be rationalised for the second mechanism proposed above. Moreover, different reaction rates after treating the palladium surface with ethylene and its deuterated analogues ( $\text{C}_2\text{D}_4$ ,  $\text{CH}_2\text{CD}_2$ ,  $\text{CHDCHD}$ ) proved that  $\text{CHDCHD}$ , containing hydrogen at  $\beta$  position, reacted faster compared to  $\text{CH}_2\text{CD}_2$  due to less blocking of ethylene adsorption

by the corresponding intermediate.

Particular emphasis has also been placed upon the deactivation of palladium carrier catalysts for VAM synthesis. Abel and co-workers [31] noted that the kinetics of deactivation are in accordance with sintering assisted by formation of mobile palladium acetate species. They observed via scanning transmission electron microscopy and energy dispersive X-ray analysis (STEM-EDX) larger palladium crystallites for deactivated VAM catalysts compared to their fresh analogues not exposed to reaction conditions. Macleod *et al.* [32] came to similar conclusions for palladium-gold alloys of commercial PdAuK/SiO<sub>2</sub> VAM catalysts by XRD and high resolution electron microscopy (HREM) with EDX. Ageing caused higher average particle sizes of 12 nm compared to fresh specimens containing of 5 nm particles, although significant change in alloy composition was not observed. Sintering discovered by these scientists involved the migration of individual alloy particles and did not implicate coalescence of palladium acetate species [31]. Limited sintering during the reaction was observed via TEM and XRD analyses for palladium particles, supported on a high surface area silica (600 m<sup>2</sup>g<sup>-1</sup>) [33]. According to the kinetic examination by Han *et al.*, a decrease in particle size results in increasing reactivity, selectivity and activation energy. Based on this dependence, the VAM reaction is determined to be structure-sensitive favouring smaller rather than larger palladium particles. In 2006 Kumar *et al.* [34] compared previous investigations in their research group [33] to a Pd(100) single crystal. They observed similar size influences and kinetic parameters for Pd(100) compared to the supported Pd catalysts. Deactivation of commercial VAM catalysts after sintering was also detected by Smejkal *et al.* [35], but was additionally assigned to a significant loss of acetate during reaction. In that study decomposition of a palladium acetate intermediate was revealed by electron paramagnetic resonance (EPR) measurements.

Besides the growth of palladium particles on a high surface area SiO<sub>2</sub> during reaction, which was obvious in XRD and TEM characterisation, Han *et al.* [36] also investigated the total oxidation of ethylene to carbon dioxide:



Understanding CO<sub>2</sub> formation represents a key to improve the selectivity of the VAM

reaction. Therefore, numerous studies were conducted in order to avoid this by-product. Since the change of ethylene combustion kinetics in the presence and absence of acetic acid was not observed by Han and co-workers [36], this implied that  $\text{CO}_2$  formation primarily resulted from ethylene. Stacchiola *et al.* [37] confirmed this conclusion by detecting ethylidene formed on the surface. In addition, they queried whether acetic acid would also be a source of  $\text{CO}_2$  formation, as previously assumed by Crathorne *et al.* [22]. As the total oxidation of alkenes can occur in two different ways [38], Kumar *et al.* [39] suggested via kinetic measurements on Pd(100) that the direct mechanism was prevalent for ethylene combustion, due to dependence of carbon deposition on  $\text{O}_2$  pressure. According to this route,  $\text{CO}_2$  and  $\text{H}_2\text{O}$  form by oxygen breaking a C-H bond of ethylene.

Significant influence on catalytic productivity and selectivity was also attributed to pore morphology [40]. Assuming a reaction controlled process, Coppens and Froment illustrated, using model simulations, that productivity rates of VAM vary by a factor of seven when comparing pores shaped like short fractals to others similar to smooth cylinders, but of equal length. It is of noteworthy importance that almost all studies hitherto investigating the mechanism of VAM reaction do not disclose realistic catalytic systems. Hence, further work will be necessary to provide a kinetic understanding for commercial VAM catalysts.

In the past ambitious efforts were made to increase activity and selectivity by developing new catalysts. Most information on VAM catalyst synthesis can be found preferentially in patent literature. Only a small fraction of the numerous patents will be referenced in this context. Based on  $\text{Na}_2\text{PdCl}_4$  and  $\text{HAuCl}_4$ , applied in the first impregnation stage as precursors, differences were claimed for the precipitation step using potassium hydroxide [41] and sodium hydroxide or its metasilicate [42]. In addition, the use of mixtures of two or more bases in this step are claimed by Süd-Chemie AG (SCAG) [43, 44]. The reduction to Pd and Au metal is also the subject of several patents. In EP 1106247 B1 for example it is described to occur in the liquid phase using hydrazine [45]. Besides, the emphasis in patent literature lies on reduction in the gas phase. For this case ethylene and hydrogen, also combined with nitrogen, were applied at different temperatures to reduce both metals in VAM catalysts, as stated in

[46–49]. In order to avoid high sodium amounts, resulting in lower catalytic activity, washing was carried out according to Bartley [42] employing a batch like technique instead of column wash. Additionally, water was replaced by a potassium acetate solution for washing. This cation exchange was also declared as a second wash procedure to remove sodium impurities in US patent 5,189,004 [50].

Special attention also has been given to the silica support properties. The use of shell catalysts for highly efficient VAM production, involving carriers of specific surface areas less than  $130\text{ m}^2\text{g}^{-1}$  [51, 52] as well as between 160 and  $175\text{ m}^2\text{g}^{-1}$ , is stated elsewhere [53]. Moreover, a pending German patent application [54] discloses a mesoporous support containing zirconia. Based on synthesis with this carrier, the activity of catalysts remains constant over a longer period of VAM reaction due to acetic acid resistance. Besides, incorporation of zirconium can also be accomplished by impregnation with adequate salts [55]. However, this results in only temporarily high activities.

Throughout history, synthesis of these catalysts was realised via an initial impregnation with metal salts. For this preparation method, Debellefontaine and Besombes-Vailhé [56] emphasised the inhomogeneity of precipitation, making any interpretation of transfer phenomena difficult. In order to avoid inhomogeneities, a new innovative technology method to make VAM catalysts is reported in [57]. Coating gold and palladium precursors on the carrier during the first step of synthesis led to optimised metal distribution in the catalyst shell. In future this innovative approach is intended to be subject of further research, but it will not be regarded in detail for this thesis.

However, the synthesis of VAM catalysts represents only one part of continuing scientific efforts. A comparison under industrial conditions is likewise necessary for further development. As a result technological progress has been made, based on a small bench scale reactor [58], representing a new screening unit. According to Temkin and Kul'kova, a fixed bed reactor applied in industry to produce VAM, can be simulated by a tube exceeding the grain diameter at least by a factor of ten in inner diameter and by a factor of 30 in length. Thus, a process-near model system can be designed. However, large VAM catalyst amounts will be needed for testing. Arvindan *et al.* [59] developed an apparatus suited for generating kinetic knowledge even for small quantities of commercial catalysts, while keeping hydrodynamics, heat and mass transfers

equivalent to larger scales. This invention facilitated evaluation of spherical catalyst particles with a diameter between 3 and 8 mm, applicable to VAM forming species. Recently, a laboratory reactor used to study gas phase acetoxylation of ethylene was described in [60–63], similar to the assembly used in this work. For both test systems, operating conditions (8-10 bar, 140-150 °C) were chosen in order to simulate pilot or industrial fixed-bed reactors. Repeatable performance measurements of high precision were realised for different catalysts. Furthermore, hot spots due to the high exothermicity of the VAM reaction, leading to undesired products, could be inhibited. As regards synthesis, screening and characterisation of VAM catalysts, the aims and approaches of this thesis will be outlined in the following chapter.

# Chapter 2

## Aims and Approaches

As shown in the previous chapter, many efforts have been made to date in order to synthesise VAM catalysts with regard to high performances. This interest can be attributed to enormous cost savings in the industrial VAM production resulting already from improvements in selectivity of about 1%. Based on the known patent literature (*cf.* chp. 1), the development of novel VAM catalysts with higher performances compared to state-of-the-art analogues is therefore the motivation of this work. Since synthesis describes only one part on the way to reach this goal, screening and characterisation of the VAM catalysts will additionally provide a basis in order to obtain a scientific understanding of this catalytic system. Figure 2.1 summarises these three aspects, presented as pillars, while giving further information about the respective activities.

In general, correlations between the performance and characteristics of catalysts are frequent subjects in literature [64]. The intention in this work is therefore to synthesise a multitude of VAM catalysts under systematic variation of process parameters, based on the incipient wetness (IW) method (fig. 4.1). With regard to the carrier, oxides of silicium, aluminium, titanium and zirconium are only some of the commercially available supports used in catalyst synthesis. Since alumina and titania dissolve in acetic acid, these carriers are not applicable for VAM production. However, small concentrations of these oxides embedded in the carrier are allowable [53, 65]. Although several different carriers are claimed in patent literature on VAM catalysts, the products

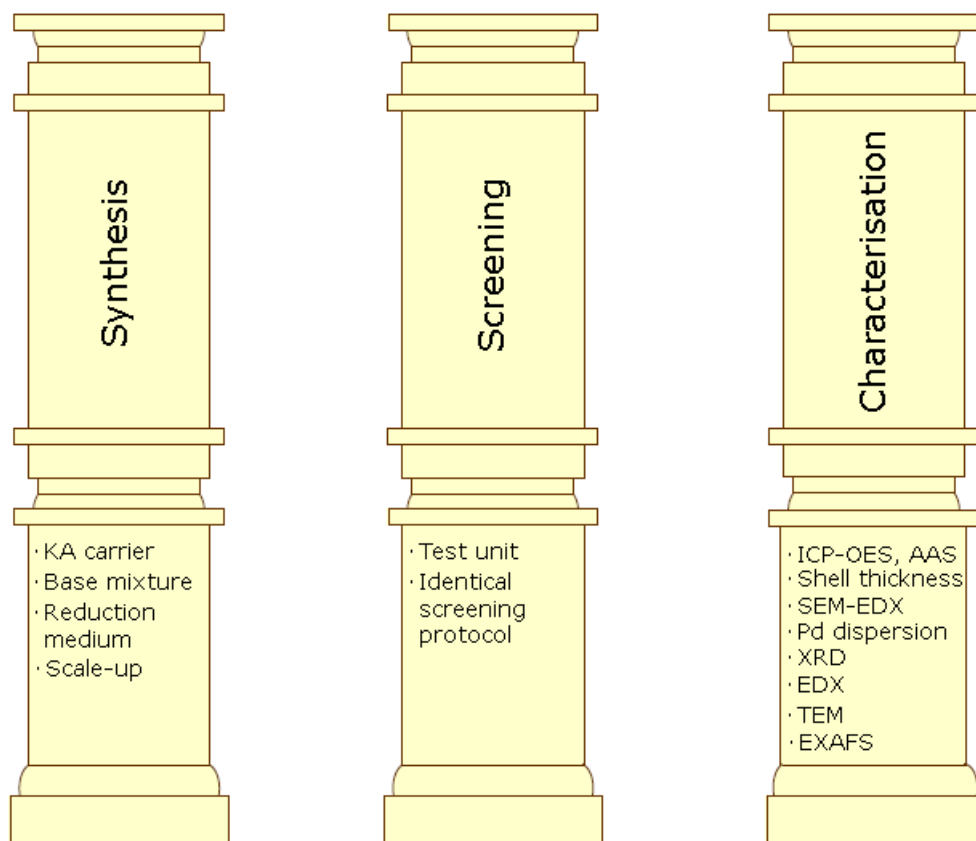


Figure 2.1: Motivation of this work schematically summarised in form of pillars.

used in this study are based on the proprietary KA carrier of Süd-Chemie AG. This expert knowledge can be considered as an enormous advantage for possible variation in carrier properties. Apart from the KA 160, which is purchased for industrial VAM production plants, a similar carrier with lower specific surface area (KA 0) will be employed for VAM catalyst synthesis in order to study the effect of larger pore sizes on the selectivity  $S$  and space time yield  $STY$ . Based on patent literature using zirconium oxide as support [55, 65, 66], Zr containing KA [54] will be regarded as a third carrier type since it is more resistant to acetic acid. Apart from Zr, Rh [66] and V [67] are optional components to improve the catalyst performance.

Additionally to the carriers, a variation in bases will be applied by using NaOH and  $\text{Na}_2\text{SiO}_3$ , which is supposed to influence the precipitation of metals. Both bases are claimed in patents, such as [42]. Different values of shell thicknesses are as well expected when applying base mixtures varying in components and concentrations for this macroscopic characteristic. For thinner shells, the favoured diffusion of educt and

product components results in higher selectivities. Thus, the shell thickness is suggested as one of the most important characteristics of VAM catalysts. It is of high interest to determine the optimum value, since both extrema can lead to undesirable consequences such as total combustion (too thin) or a decrease in selectivity (too thick).

With regard to the reduction of the hydroxides to Pd and Au metal during the IW synthesis, two different methods will be subject of the herein presented studies. Since a strong interaction exists between the metals and the KA carrier surface, reduction in gas phase at temperatures of several 100 °C is supposed to result in small metal particles. The reduction of VAM catalysts with  $\text{NaH}_2\text{PO}_2$  in the liquid phase would probably lead to different particle diameters. In correlation to the  $S$  and  $STY$ , metal particle sizes are expected to play an important role on the microscopic scale.

Apart from systematic variation in synthesis, screening of the obtained VAM catalysts will be a further objective of this thesis. Since catalyst testing in a common benchscale tube reactor results in less performance due to inefficient mass and heat transport, a screening unit based on the Temkin reactor concept [58] will be used to optimise the measurements. Only those screenings provide the basis to interpret the obtained  $S$  and  $STY$  data with regard to the employed synthesis route and the characterisation results.

In order to establish an understanding for the catalytic performance, characterisation will be a third aim of this research. Those activities will be carried out for a selection of catalysts revealing notable differences in  $S$  and  $STY$ . Besides wet chemical analysis of Pd, Au,  $\text{K}^+$  and  $\text{Cl}^-$  concentrations via atomic absorption spectrometry (AAS) and inductively coupled plasma optical emission spectrometry (ICP-OES), other properties like the previously mentioned shell thickness of VAM catalysts will be studied. The investigation on the microscopic scale will be accomplished by several analytical methods. X-ray powder diffraction (XRD) is expected to give information about the elements and phases present in VAM catalysts. It is of high interest to compare the position and intensity of diffraction lines to answer the following questions: Do alloy compositions of palladium and gold exist? In which oxidation state is palladium present? Which average particle sizes can be expected? Furthermore, the elementary composition can be determined by energy dispersive X-ray spectroscopy (EDX). Ad-

ditionally, transmission electron microscopy (TEM) and Pd dispersion are expected to reveal average diameters of the metal particles. TEM will also be used to determine the particle size distribution in several VAM catalysts. As a final technique extended X-ray absorption fine structure spectroscopy (EXAFS) will be employed to confirm the previously obtained particle sizes. Moreover, EXAFS is known to provide information about average metal coordinations and distances between precious metal atoms, but it can also give details about possible PdAu alloy compositions.

As a conclusion, the results on catalyst selectivity and space time yield will show whether a synthesised species has the potential to be used for VAM production, and which of the analysed VAM catalysts represents an optimum. By means of the sophisticated analytical methods described above, correlations between catalyst features-particle composition, size as well as structure- and performance data will be revealed.

# Chapter 3

## Experimental procedures

### 3.1 Synthesis sequence of VAM catalysts

Preparation of VAM catalysts using an incipient wetness method was carried out by a sequence of individual operations described subsequently and summarised in figure 3.1. In this scheme, components mixed together during a synthesis step are marked in green. Red colour in precipitation and reduction stages implies alternative chemicals, *i. e.* only one of the presented options was used for a particular sample. Thus, a variety of different catalyst specimens could be obtained. It should be pointed out that detailed information on synthesis conditions employed for each catalyst preparation, for example the compound amounts, will be given in sections 3.2 and 3.3.

In the first stage of synthesis metal precursor solutions of sodium tetrachloropalladate ( $\text{Na}_2\text{PdCl}_4$ ) and chloroauric acid ( $\text{HAuCl}_4$ ) were mixed with deionised water [9] in a rotary evaporator. The spherical catalyst support was then rapidly added while stirring continued. The carrier pores were filled with the provided solution within a one hour time frame until they got dry. This process is illustrated by the photographs in figure 3.2.

Subsequently the precursor noble metal salts were precipitated by adding the impregnated spheres to an alkaline solution of sodium hydroxide ( $\text{NaOH}$ ), sodium metasilicate ( $\text{Na}_2\text{SiO}_3$ ) [9, 42] or to a base mixture of both [43, 44]. Fixation to obtain the corresponding hydroxides required about 16-25 hours. The conversion is illustrated by the

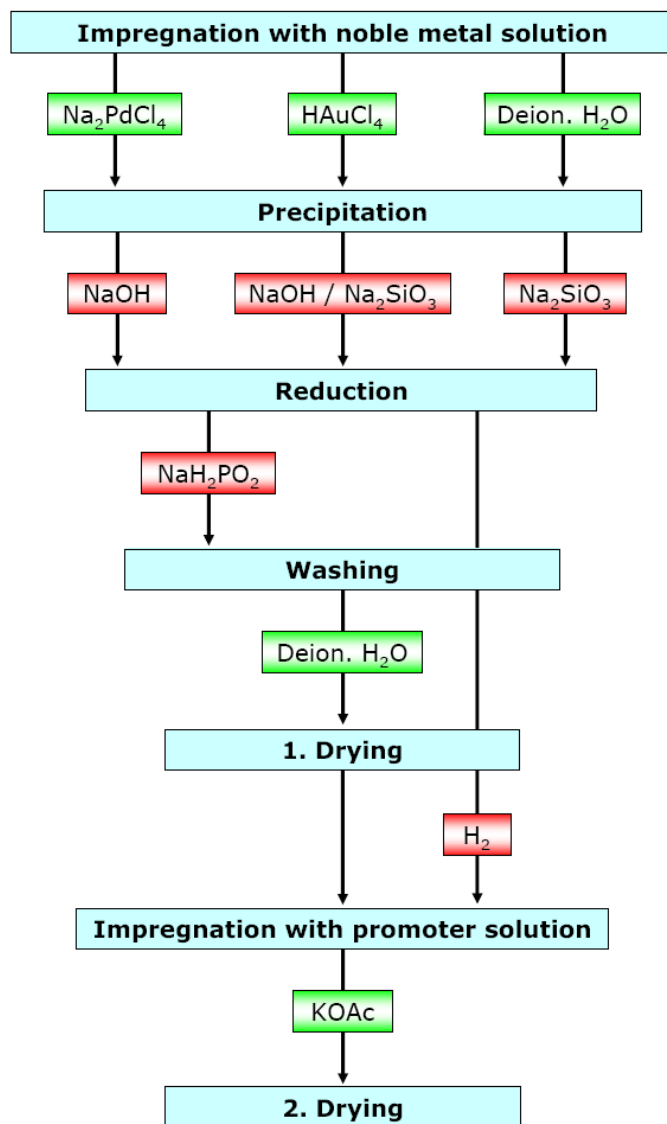


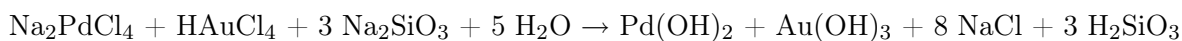
Figure 3.1: Schematic overview of unit operations for VAM catalyst synthesis via IW method.

chemical equations given below. Figure 3.3 depicts this step resulting in precipitation of hydroxides. It is assumed that the change in colour is due to gold formation induced by light exposure.

a)  $\text{NaOH}$ :



b)  $\text{Na}_2\text{SiO}_3$ :



Reduction either in liquid or gas phase represents the third step of VAM catalyst synthesis. For both media the fixation solution was decanted prior to reduction. In the case of liquid phase reduction (LPR), carrier spheres were exposed at room temperature to a solution of sodium hypophosphite ( $\text{NaH}_2\text{PO}_2$ ) for two hours (fig. 3.4) [57]. During this period the noble metal hydroxides were transformed into the active metal states, specified by the following reaction equation.

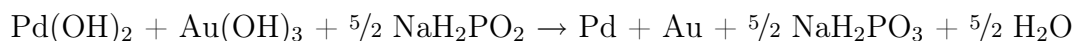


Figure 3.2: Progress of impregnation by adding carrier spheres which continuously absorb the noble metal solution.

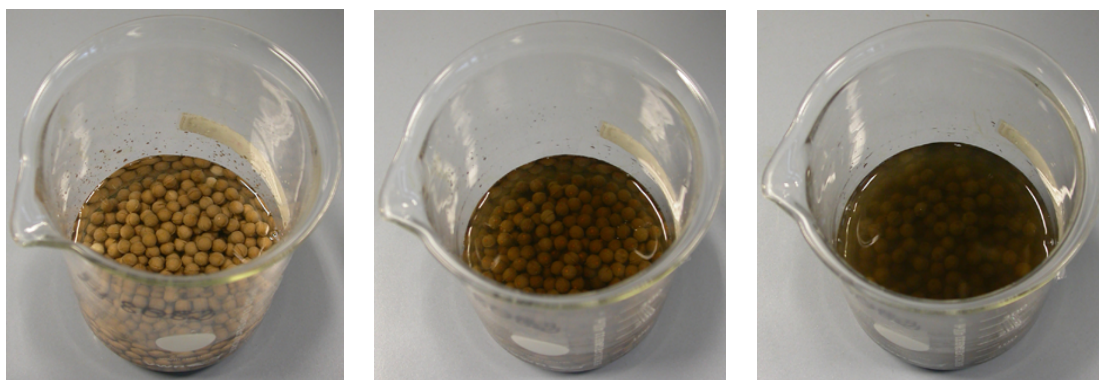


Figure 3.3: Conversion of noble metals to corresponding hydroxides.

In case of gas phase reduction (GPR), hydroxides were converted by exposing the spheres for five hours to a gas mixture of 5 %  $\text{H}_2$  and 95 %  $\text{N}_2$  [46–49]. This operation was carried out, depending on the catalyst amount, either in a small furnace (fig. 3.5)

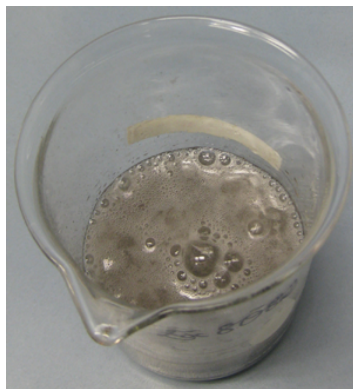


Figure 3.4: Liquid phase reduction of metal hydroxides to metallic state with simultaneous formation of hydrogen.

at 200 °C or in a 1 L bench scale reduction oven at temperatures between 100 and 450 °C. The reaction occurring during GPR can be described as follows:

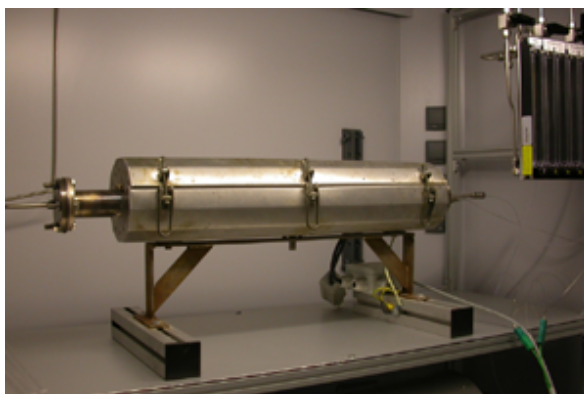
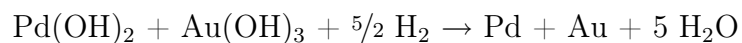
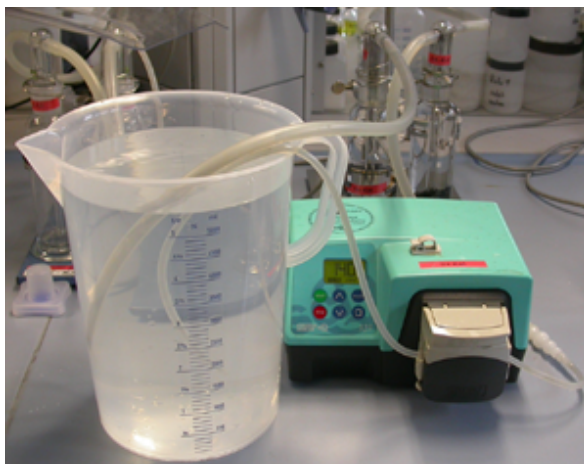


Figure 3.5: Gas phase reduction furnace used for conversion of noble metal hydroxides to the metallic state.

Concerning the washing and drying step [9], equal process parameters were applied for both reduction routes. However, for GPR these synthesis operations were carried out prior to reduction (*cf.* fig. 3.1). For the liquid phase analogue, washing was conducted subsequent to reduction. The hypophosphite solution was decanted and then washing was realised by pumping double distilled water in a closed flow system with 140 rounds per minute through the spheres (fig. 3.6). This operation is necessary to free the

catalyst from deactivating chlorides. It was completed within a 20 minutes time frame, when the conductivity of the wash water was below  $2\mu\text{S}$ .



**Figure 3.6:** Closed loop flow system pumping double distilled water through the catalyst precursor in order to wash out chlorides.

After washing the catalyst spheres were dried in order to empty the pores before final impregnation with potassium acetate could occur [9]. At the beginning of this work spheres were dried in an appropriate cabinet over night. However, this drying method resulted in irregularly coloured spheres indicating inhomogeneous impregnation. In order to avoid this effect, a fluidised-bed dryer (fig. 3.7) was implemented for drying. The colour of catalyst spheres was henceforward uniform. Furthermore, it led to a tremendous gain of time since drying at  $90^{\circ}\text{C}$  required less than two hours, depending on the moisture of the catalyst.

For completion of VAM catalyst synthesis, the dried spheres were impregnated with a solution of potassium acetate (KOAc), which was homogeneously distributed on the spheres by continuous agitation. Potassium acetate plays an important role for this catalytic system since it keeps acetic acid on the catalyst surface. After total absorption of the KOAc solution, the catalyst spheres were allowed to stay at room temperature for one hour. Finally the VAM catalyst was dried again using the same parameters as before.

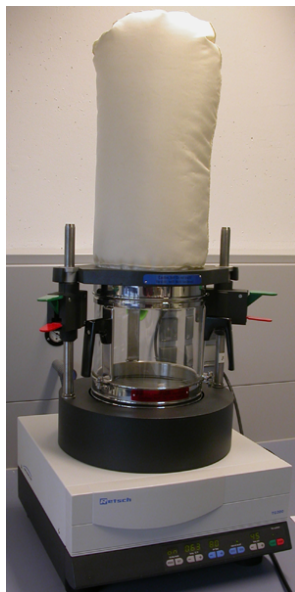


Figure 3.7: Time saving fluidised-bed dryer used for VAM catalyst synthesis.

## 3.2 Parameter variation of proprietary synthesis recipes

### 3.2.1 Carrier selection

Selection of an adequate carrier is one of the most important tasks at the beginning of development efforts for high performance VAM catalysts. Carrier properties subject to optimisation are outlined in the following discussion.

Süd-Chemie AG has been producing the so-called KA carriers for many years. This expert knowledge can be considered as an enormous advantage for VAM catalyst synthesis. The carriers, also purchased by other companies to produce VAM catalysts, are manufactured in Moosburg. The KA support used herein is a bentonite mainly consisting of natural phyllosilicate montmorillonite, as shown in figure 3.8. Layers of the structural unit represented by  $\text{SiO}_4$  tetrahedra are electrostatically bonded by octahedral layers, where a cation-like foremost  $\text{Al}^{3+}$  is enclosed by a hydroxide group and oxygen respectively. Montmorillonite is assigned to the smectite family, a 2:1 clay mineral containing two tetrahedral layers sandwiching one central octahedral layer.

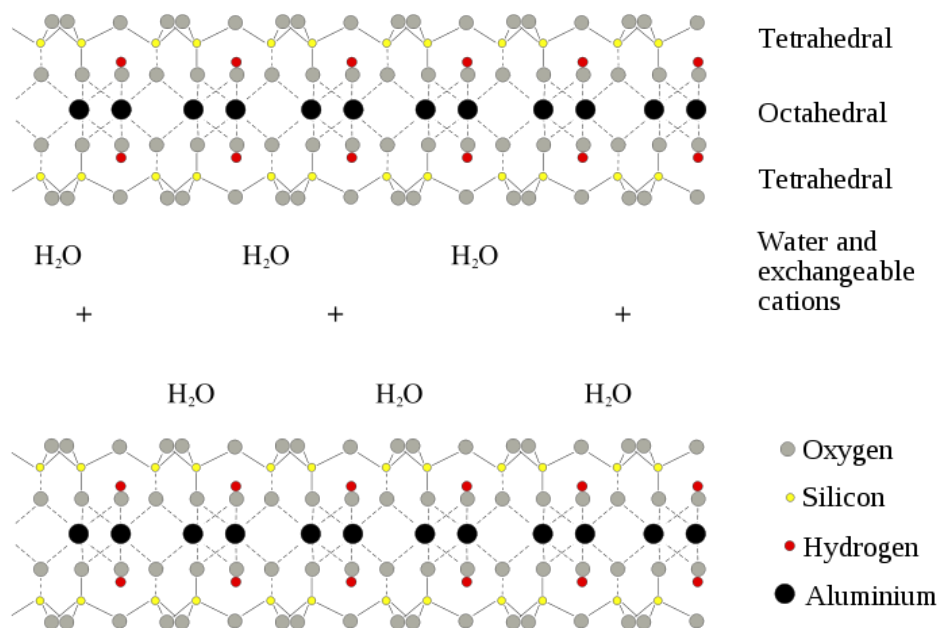


Figure 3.8: Molecular structure of montmorillonite.

In order to give an overview on representative VAM carriers, three species are listed in table 3.1. Nomenclature of carriers is according to their specific surface areas, for example KA 160 ( $\text{BET} \approx 160 \text{ m}^2\text{g}^{-1}$ ) and KA 0 ( $\text{BET} \approx 100 \text{ m}^2\text{g}^{-1}$ ). For most of the experiments carried out within this work, charge 7073 of KA 160 was chosen as the catalyst support due to its higher wet capacity compared to charge 6599, which was expected to enable optimisation of VAM catalyst synthesis. In addition to KA 160, syntheses were accomplished for two further carrier types (KA 0 and KA-Zr). Details for VAM catalyst preparations based on these SCAG carriers will be given separately in the following two sections.

A significant difference between these three carriers can be seen in their porosity characteristics. In principle high wet capacities result from big pores going along with low specific surface areas as exemplified by charge 1812 (KA 0). Typical wet capacities average between  $0.58$  and  $0.62 \text{ Lkg}^{-1}$ . Two of the below mentioned carrier lots exceed this typical value showing outstanding wet capacity due to a relatively low specific surface area. Large values of wet capacity are generally preferred for VAM synthesis in order to avoid highly concentrated solutions. In addition, bigger pores provide higher selectivities due to minimised diffusion limitation and improved mass transport. Figure 3.9 summarises the pore diameter distribution for each carrier obtained via the

Table 3.1: KA 160 and KA 0 carriers for VAM catalyst synthesis, produced by SCAG Moosburg.

Carrier	KA 160	KA 160	KA 0
Charge	7073	6599	1812
Specific surface [ $\text{m}^2\text{g}^{-1}$ ]	161	164	106
Wet capacity [ $\text{Lkg}^{-1}$ ]	0.664	0.592	0.695
Crush strength [N]	56	86	52
Bulk density [ $\text{gL}^{-1}$ ]	545	583	528
$\text{Cl}^-$ [ppm]	190	100	115
$\text{SiO}_2$ [wt %]	91.8	91.8	95.1
$\text{Al}_2\text{O}_3$ [wt %]	3.60	3.30	0.95
$\text{Fe}_2\text{O}_3$ [wt %]	0.47	0.46	0.11
$\text{TiO}_2$ [wt %]	0.30	0.30	0.22
$\text{MgO}$ [wt %]	0.22	0.23	0.06
$\text{CaO}$ [wt %]	0.15	0.12	0.06
$\text{K}_2\text{O}$ [wt %]	0.54	0.64	0.16
$\text{Na}_2\text{O}$ [wt %]	0.35	0.27	0.17

BJH method [68]. The average pore diameters resulting from those figures are included in table 3.2.

Although carrier KA 0 reveals an outstanding wet capacity due to big pores, its use is limited by the low crush strength. High mechanical strength is considered as desirable for practical reasons, even though for chemical purposes corresponding smaller pores represent a disadvantage as explained before. Besides, since catalysts are sold by weight in kg and not by volume, low bulk densities are favoured due to cost reasons. Among the carriers KA 160 charge 7073 provides an excellent combination of mechanical stability (higher than KA 0), elevated wet capacity and low bulk density (compared to KA 160 charge 6599).

During carrier fabrication hydrochloric acid is used as washing agent, in order to eliminate metal impurities in the pores. This operation results in residual amounts of chloride in the support. Its concentration has to be kept as low as possible due to

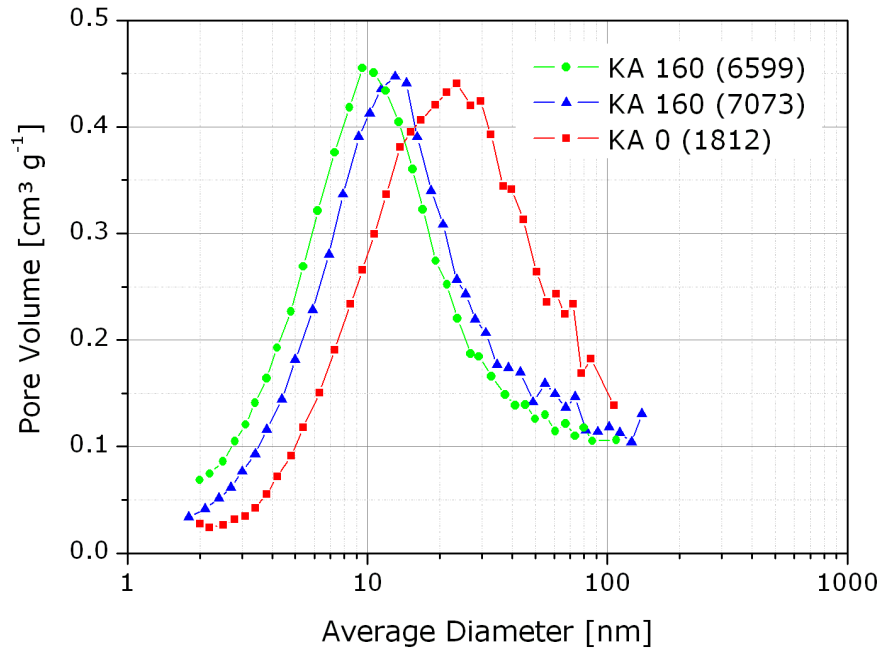


Figure 3.9: Pore diameter distribution via BJH method for different KA carriers at 77.15 K and an equilibration interval of 20 s.

Table 3.2: Average pore diameters obtained by BJH method for lots 7073 and 6599 of carrier KA 160 and lot 1812 of KA 0.

Carrier	KA 160	KA 160	KA 0
Charge	7073	6599	1812
Average pore diameter [nm]	10.7	9.4	15.6

the poisonous effect of chloride on VAM production. Since the chloride specification limit is between 200 and 300 ppm, all values listed in table 3.1 are comparatively low. Apart from crush strength, this concentration reflects the biggest difference between both KA 160 carriers.

Further differences between the two superior carrier species are represented by the concentrations of  $\text{SiO}_2$  and  $\text{Al}_2\text{O}_3$ . In this regard, low values of  $\text{Al}_2\text{O}_3$  were desirable as it is soluble in AcOH whereas  $\text{SiO}_2$  is chemically resistant. The effect of other oxides on VAM synthesis is unknown.

### 3.2.1.1 Low specific surface support (KA 0)

In this paragraph a catalyst synthesis based on carrier KA 0 will be presented in order to provide a basis for comparison to the higher specific surface analogue KA 160 described subsequently. Details for the preparation of a 65 g VAM catalyst by using KA 0 as support are presented in the following tables. Table 3.3 reveals the components and corresponding net weights applied for experiment number (*EX No.*) *EX7307*. In the subsequent table 3.4 details of single operation parameters during this synthesis are listed. For all experiments presented in this work, the herein mentioned chemicals were used. Both noble metal precursor solutions  $\text{Na}_2\text{PdCl}_4$  (16-18 wt % Pd) and  $\text{HAuCl}_4$  (38-42 wt % Au) utilised for initial impregnation were purchased from Heraeus. For precipitation a 0.3-0.5 M NaOH solution was applied, based on 1 M stock solution supplied by Riedel-de Haen. Apart from these chemicals, a 10 wt % solution of  $\text{NaH}_2\text{PO}_2$  provided by Fluka was used for LPR of the catalyst precursor. Finally for promoter impregnation, KOAc purchased from Merck was used to prepare a 1-2 M stock solution.

Table 3.3: Compounds for VAM catalyst synthesis based on charge 1812 of KA 0 carrier; all net weights are represented in g.

<i>EX No.</i>	Compound	Net weight [g]
<i>7307</i>	1. $\text{Na}_2\text{PdCl}_4$	3.18
	2. $\text{HAuCl}_4$	0.61
	3. $\text{H}_2\text{O}$	41.12
	4. NaOH	106.05
	5. $\text{NaH}_2\text{PO}_2$	86.72
	6. KOAc	27.29
	7. $\text{H}_2\text{O}$	18.55
	8. KA 0	65.02

As previously mentioned, aside from VAM catalyst synthesis based on support KA 0, most of the preparations presented in this work were accomplished with charge 7073 of

Table 3.4: Parameters for VAM catalyst synthesis based on charge 1812 of KA 0 carrier.

Impregnation	Precipitation	LPR	Washing	1. Drying	2. Drying
t [min]	t [h]	t [h]	t [h]	t [min]	t [min]
T	T	T	s [ $\mu$ S]	T [ $^{\circ}$ C]	T [ $^{\circ}$ C]
100	22.0	2	8.0	50	40
RT	RT	RT	1.9	90	90

KA 160 carrier. These catalyst syntheses will be described with regard to parameter variation during single operations in section 3.2.2 and subsequently.

### 3.2.1.2 Zr-based KA carriers

Another carrier species was produced by SCAG, based on zirconium, for VAM catalyst synthesis. Due to its acetic acid resistance [54], the incorporation of zirconium in the KA carrier is more favoured than using pure zirconium dioxide as support [65, 66] or impregnating the adequate metal salts [55]. The concentration of Zr in the employed KA carriers varied between 2 and 19 wt % as table 3.5 indicates. Their BET surface areas were in the range of the previously presented KA carriers, outlined in section 3.2.1.

Table 3.5: KA-Zr supports for VAM catalyst preparation produced by SCAG Moosburg.

KA-Zr...	10V1-3	10V1-4	10V1-3+4+	20V1-4	8V1-5	11V1-4
Zr [wt %]	5-7	4-6	3-5	17-19	2-4	8-12
Specific surface [ $\text{m}^2\text{g}^{-1}$ ]	158	144	124	132	125	133

One objective of this work was to find out which Zr carrier led to the best performing VAM catalyst. Therefore catalysts were synthesised with each of the above Zr carriers as support (tab. 3.6 and 3.7). Since, unlike KA carriers, pure  $\text{ZrO}_2$  is lacking defects and anchor points, metal complexes cannot be adsorbed during impregnation. Hence, formation of an adsorption shell is not possible with  $\text{ZrO}_2$  as support, although embedded in the bentonite carrier it may occur. Section 4.2.2 will reveal for which KA-Zr carriers shell formation was achieved.

Table 3.6: Compounds for VAM catalyst synthesis based on different KA-Zr carriers; all net weights are represented in g.

<i>EX No.</i>	<i>7303</i>	<i>7304</i>	<i>7305</i>	<i>7306</i>	<i>7804</i>	<i>8082</i>
KA-Zr...	10V1-3	10V1-4	10V1-3+4+	20V1-4	8V1-5	11V1-4
1. Na <sub>2</sub> PdCl <sub>4</sub>	3.19	3.17	3.19	3.17	1.96	3.23
2. HAuCl <sub>4</sub>	0.61	0.62	0.63	0.62	0.38	0.63
3. H <sub>2</sub> O	35.97	37.39	38.97	39.63	24.40	31.14
4. NaOH	100.26	100.26	100.28	100.27	61.70	100.28
5. NaH <sub>2</sub> PO <sub>2</sub>	86.71	86.71	86.73	86.72	53.38	86.72
6. KOAc	27.30	27.31	27.30	27.30	16.81	27.30
7. H <sub>2</sub> O	16.59	14.84	16.40	17.03	10.53	8.59
8. KA-Zr	65.00	65.00	65.03	65.03	40.01	65.04

Table 3.7: Parameters for VAM catalyst synthesis based on different KA-Zr carriers.

	<i>EX No.</i>	<i>7303</i>	<i>7304</i>	<i>7305</i>	<i>7306</i>	<i>7804</i>	<i>8082</i>
Impregnation	t [min]	130	70	85	65	95	60
	T	RT	RT	RT	RT	RT	RT
Precipitation	t [h]	21.0	20.0	22.5	21.5	21.5	22.3
	T	RT	RT	RT	RT	RT	RT
LPR	t [h]	2	2	2	2	2	2
	T	RT	RT	RT	RT	RT	RT
Washing	t [h]	6.5	6.5	6.5	6.5	4.0	4.5
	s [ $\mu$ S]	1.4	0.6	1.2	1.4	1.5	1.6
1. Drying	t [min]	70	70	70	70	60	60
	T [ $^{\circ}$ C]	90	90	90	90	90	90
2. Drying	t [min]	70	70	70	70	60	60
	T [ $^{\circ}$ C]	90	90	90	90	90	90

### 3.2.2 Precipitation with base mixtures

In most of the patent literature a solution of NaOH is commonly applied for precipitation.  $\text{Na}_2\text{SiO}_3$  of the same molar concentration purchased from Alfa Aesar will be presented in this work as an alternative base used in the fixation step. Appropriate bases are characterised by high metal retention and low carrier degradation. Since the acid KA carrier can be more seriously attacked by stronger bases like KOH, NaOH is preferred for fixation in this study. Furthermore, less alkaline solutions decrease metal loss during precipitation, since pH values higher than 8 lead to dissolution of precious metals. Sodium metasilicate is therefore expected to minimise metal loss compared to NaOH.

Based on general experience, thin and uniform shells of about  $200\text{ }\mu\text{m}$  thickness are suited for achieving high catalyst selectivities. Besides, Pd and Au distribution in the shell should be homogeneous. The conventional precipitation with stoichiometric excess of 200-210% often leads to thick and irregular shells. On the one hand, high stoichiometric excess is necessary for precipitating a maximum amount of chlorides in order to achieve high metal retention for catalysts. But on the other hand, it leads to rapid diffusion into the spheres precipitating noble metal chlorides more in the interior zones of the shell. Back diffusion of soluble metal precursors to near to the surface areas can not occur in this case. Hence, thick shells would result in materials as illustrated in figure 3.10.

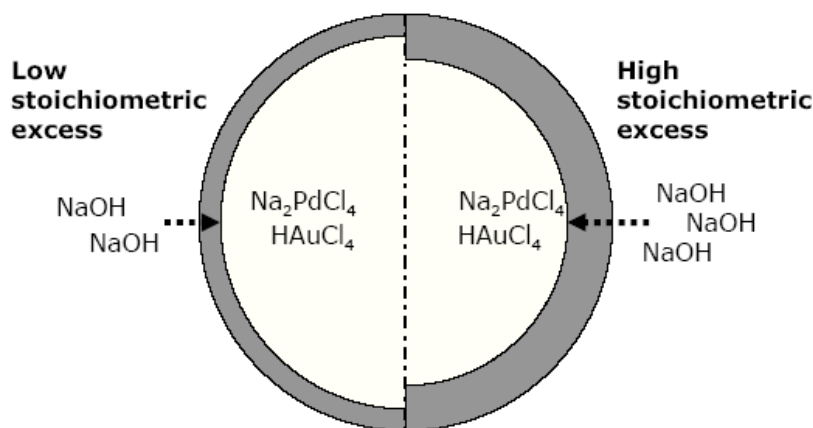


Figure 3.10: Shell formation for different stoichiometric excesses of NaOH.

In order to slow down base diffusion into the spheres, all experiments presented herein were accomplished with a lower stoichiometric excess of 170-190 %. This resulted in thinner shells (*cf.* sec. 4.2.2) which enable precursor back diffusion. With the aim of studying the influence of  $\text{Na}_2\text{SiO}_3$  on shell thickness and catalyst performance, a series of experiments with different ratios of  $\text{NaOH}/\text{Na}_2\text{SiO}_3$  was carried out. The following tables (tab. 3.8 and 3.9) give details of synthesised samples with an increasing amount of  $\text{Na}_2\text{SiO}_3$  in the precipitation step.

Table 3.8: Compounds for VAM catalyst synthesis based on different base mixtures in the precipitation step; all net weights are represented in g.

<i>EX No.</i>	<i>6152</i>	<i>6312</i>	<i>6313</i>	<i>6314</i>	<i>6315</i>
$\text{NaOH}/\text{Na}_2\text{SiO}_3$	100/0	70/30	50/50	30/70	0/100
1. $\text{Na}_2\text{PdCl}_4$	0.97	0.97	0.97	0.97	0.98
2. $\text{HAuCl}_4$	0.18	0.18	0.20	0.19	0.19
3. $\text{H}_2\text{O}$	11.54	11.52	11.51	11.52	11.54
4. $\text{NaOH}/\text{Na}_2\text{SiO}_3$	28.48	19.94/4.27	14.24/7.11	8.54/9.97	14.25
5. $\text{NaH}_2\text{PO}_2$	26.68	26.67	26.68	26.67	26.70
6. KOAc	8.41	8.42	8.40	10.65	8.41
7. $\text{H}_2\text{O}$	4.60	4.46	4.31	5.81	4.31
8. KA 160	20.03	20.07	20.02	20.01	19.99

### 3.2.3 Liquid phase versus gas phase reduction

Apart from the previously mentioned catalysts precipitated with base mixtures prior to LPR, analogous samples were prepared using  $\text{NaOH}$  or  $\text{Na}_2\text{SiO}_3$  during fixation, but applying GPR (tab. 3.10, 3.11). The catalyst spheres were exposed at a temperature of 200 °C for five hours to a gas mixture of 5 %  $\text{H}_2$  ( $F_{\text{H}_2} = 250 \text{ NmLmin}^{-1}$ ) and 95 %  $\text{N}_2$  ( $F_{\text{N}_2} = 4750 \text{ NmLmin}^{-1}$ ). Systematic variation of this synthesis parameter was a major focus in this study, since the reduction medium is supposed to have a high influence on the performance of VAM catalysts. Further relevant catalysts, reduced via forming gas, will be presented in section 3.3.

Table 3.9: Parameters for VAM catalyst synthesis based on different base mixtures in the precipitation step.

	<i>EX No.</i>	<i>6152</i>	<i>6312</i>	<i>6313</i>	<i>6314</i>	<i>6315</i>
Impregnation	t [min]	65	55	25	58	47
	T	RT	RT	RT	RT	RT
Precipitation	t [h]	22.5	22.0	21.5	20.5	21.0
	T	RT	RT	RT	RT	RT
LPR	t [h]	2	1.7	2	2	2
	T	RT	RT	RT	RT	RT
Washing	t [h]	5.0	5.0	5.0	5.5	4.0
	s [ $\mu$ S]	1.2	1.2	1.1	1.1	0.7
1. Drying	t [min]	40	40	40	40	40
	T [ $^{\circ}$ C]	90	90	90	90	90
2. Drying	t [min]	40	40	40	40	40
	T [ $^{\circ}$ C]	90	90	90	90	90

Table 3.10: Compounds for VAM catalyst synthesis based on GPR using different bases in the precipitation step; all net weights are represented in g.

<i>EX No.</i>	<i>6318</i>	<i>6316</i>
Precipitation agent	NaOH	Na <sub>2</sub> SiO <sub>3</sub>
1. Na <sub>2</sub> PdCl <sub>4</sub>	1.96	1.97
2. H <sub>2</sub> AuCl <sub>4</sub>	0.37	0.38
3. H <sub>2</sub> O	22.79	22.78
4. NaOH or Na <sub>2</sub> SiO <sub>3</sub>	56.96	28.47
5. KOAc	16.85	16.83
6. H <sub>2</sub> O	8.63	8.67
7. KA 160	40.01	40.02

Table 3.11: Parameters for VAM catalyst synthesis based on GPR using different bases in the precipitation step.

	<i>EX No.</i>	<i>6318</i>	<i>6316</i>
Impregnation	t [min]	112	60
	T	RT	RT
Precipitation	t [h]	20.0	21.0
	T	RT	RT
GPR	t [h]	5	5
	T [°C]	200	200
Washing	t [h]	8.0	7.5
	s [ $\mu$ S]	4.5	2.4
1. Drying	t [min]	40	40
	T [°C]	90	90
2. Drying	t [min]	40	40
	T [°C]	90	90

### 3.3 Scale-up of laboratory synthesis

Plant certification trials using about 60 kg carrier were performed in the precious metal plant in order to optimise VAM catalyst production parameters. Scaling-up the laboratory recipes included all of the unit operations mentioned in section 3.1.

Prior to production, emphasis is especially on quality control. Specification limits have to be respected for all chemicals used in production, but also for the catalyst precursors resulting from each unit operation. Since for example platinum and silver are detrimental for VAM catalysts, concentrations are restricted to 100 ppm in the noble metal solutions. During prearrangement before plant production, the physicochemical characteristics were also determined, for comparison with the finally resulting catalyst. These quality features were included in a production control plan. Apart from tolerances, test systems and analytical sampling frequencies were also specified in this document, accompanied by information concerning quality control samples for further

analysis. To achieve an optimum procedure, several particulars, such as homogeneous moistening of spheres after noble metal impregnation were also taken into consideration. In order to ensure that no unimpregnated carrier spheres remained in the large scale mixer, visual control was carried out prior to the subsequent precipitation step.

As in the single preparation steps, quality control played an important role for the VAM catalyst produced. The following parameters, defined in work instructions, had to be determined to complete a successful plant trial:

- Concentrations of Pd, Au, K and Cl
- Residual moisture content
- Sphere diameter
- Attrition
- Wet capacity
- Crush strength
- Shell thickness
- Catalytic performance

Two of the conducted test productions referred to as *B* and *D* (tab. 3.12) will be discussed in detail, in order to study the difference between LPR and GPR. After impregnation for 60-90 minutes and subsequent precipitation at room temperature requiring 15-19 hours, LPR for the *B* catalyst precursor and washing for the *D* analogue prior to GPR were conducted. Comparison of final conductivities of wash water for both trials revealed that the value for *B* ( $4.6\ \mu\text{S}$ ) was lower than for *D* ( $16.3\ \mu\text{S}$ ), although the washing time was four hours shorter. The lower final conductivity for *B* is therefore assumed to be associated with carrying out the reduction in liquid phase. In this case chlorides can diffuse into the sodium hypophosphite solution, decreasing the amount in the spheres. For catalysts reduced in gas phase, this additional contact with a solution medium is not provided.

Reduction of *D* precursor was achieved via forming gas (5 %  $\text{H}_2$ , 95 %  $\text{N}_2$ ) streaming in a 1 L bench scale reduction oven with a flow of  $1200\ \text{NLh}^{-1}$  achieving a gas hourly space velocity of about  $2400\ \text{h}^{-1}$  ( $m_D \approx 0.5\ \text{kg}$ ). Due to the large amount of catalyst

Table 3.12: Compounds for VAM catalyst plant trials *B* and *D* based on different reduction media; all net weights are represented in kg.

<i>Plant trial</i>	<i>B</i>	<i>D</i>
Reduction	LPR	GPR
1. Na <sub>2</sub> PdCl <sub>4</sub>	2.89	3.12
2. HAuCl <sub>4</sub>	0.61	0.64
3. H <sub>2</sub> O	39.38	37.05
4. NaOH	113.89	84.83
5. NaH <sub>2</sub> PO <sub>2</sub>	86.72	-
6. KOAc	27.30	<i>cf.</i> tab. 3.13
7. H <sub>2</sub> O	16.59	<i>cf.</i> tab. 3.13
8. KA 160	65.00	65.00

precursor received from test production, a diversified investigation using different reduction temperatures for subsequent performance evaluation was possible. Table 3.13 represents the multiplicity of reduction temperature varied catalysts.

Table 3.13: Temperature variation for GPR of *D* catalysts.

<i>EX No.</i>	<i>8140</i>	<i>7273</i>	<i>7274</i>	<i>7275</i>	<i>8136</i>	<i>8137</i>	<i>8138</i>	<i>8139</i>
t [h]	5	5	5	5	5	5	5	5
T [°C]	100	150	200	250	300	350	400	450
1. KOAc [g]	93.16	93.39	93.35	93.41	111.96	119.89	138.52	136.44
2. H <sub>2</sub> O [g]	39.13	39.23	39.20	39.25	47.05	50.37	58.20	57.32
3. <i>D</i> precursor [g]	20.69	20.75	20.76	20.72	23.46	25.88	30.79	30.32

Figure 3.11 displays temperature versus time during the reduction process exemplified by catalyst *EX8139*. Temperature was controlled in several positions in the oven (upper, middle and lower sections) in addition to control of the gas stream temperature. For each catalyst sample the heating rate was 2 °Cmin<sup>-1</sup> until the reduction temperature was reached. Reduction was completed after five hours. The samples were then cooled down to 30 °C at a constant rate of 5 °Cmin<sup>-1</sup>. Subsequent to GPR

catalyst species were impregnated with specific amounts of KOAc and deionised water (tab. 3.13). Drying at 90 °C for 40-60 minutes completed each synthesis.

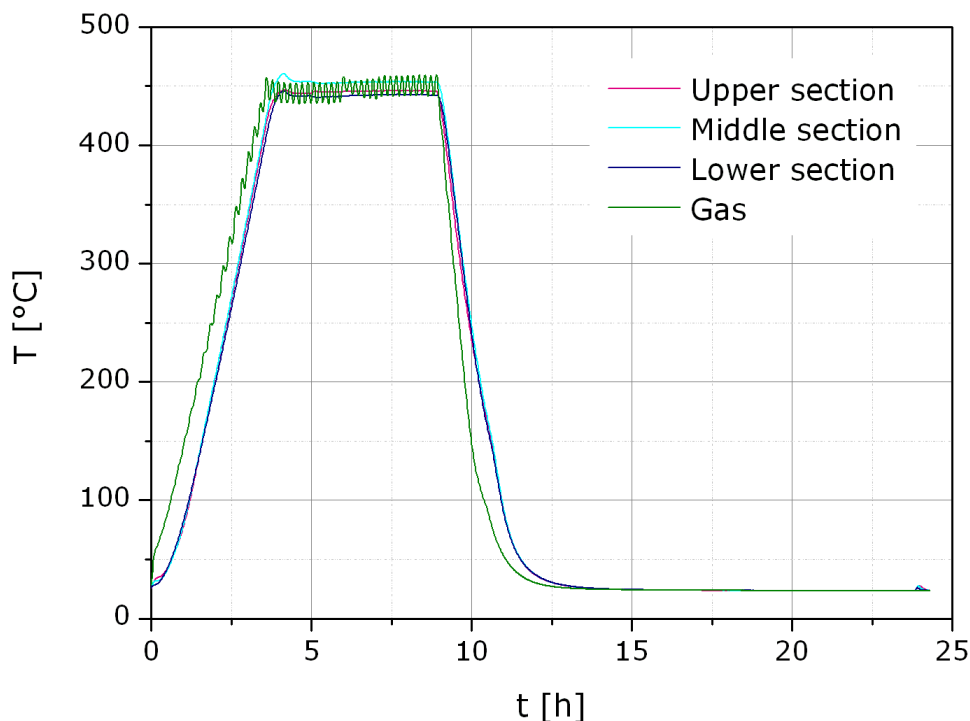


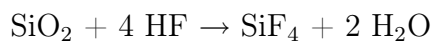
Figure 3.11: Temperature control for gas phase reduction of catalyst *EX8139* by measurements at different oven positions.

### 3.4 Method development for precious metal analysis

Since performance correlates strongly with the amount of noble metal in the final catalyst, all previously synthesised samples were wet-chemically analysed in order to determine the elemental composition. These results were also used to quantify the metal loss after precipitation and LPR. This paragraph emphasises the chronological improvement of VAM catalyst analysis, whereas the analytical results are presented in section 4.2.1.

Prior to analysis approximately 2-4 g of catalyst spheres were pulverised for ten minutes in a mill until a homogeneous powder was obtained. The analytical challenge consisted in selection of a suitable decomposition agent for this sample composition, enabling dissolution of its components. Hydrofluoric acid was chosen as agent for the

KA carriers since SiO<sub>2</sub>, representing the largest portion, could be completely removed as silicon tetrafluoride (see below). In a second step aqua regia was employed, providing equal solubilities for the noble metals and potassium.



In detail, 200 mg of sample were brought into solution by application of 4 mL hydrofluoric acid mixed with an equal volume of aqua regia, aided by boiling in water bath. Subsequently, concentrations of Pd, Au and K were determined by atomic absorption spectrometry (AAS; Thermo Solar). Although the resulting values were reproducible with adequate accuracy, a systematic error seemed to occur. Discrepancies were observed when comparing the results with those generated at another SCAG facility and external laboratories, respectively.

For this reason a second method using both chemicals consecutively instead of simultaneously was developed to analyse the SCAG proprietary VAM catalysts: 4 mL of hydrofluoric acid was added to 200 mg of powder and heated for two hours at 160 °C. Thus, silica evaporated in form of silicon tetrafluoride (as shown in the above equation). This step was repeated for the dry residue in a volumetric flask in order to ensure that no silica remained.

Then the remaining material was dissolved in 12 mL of aqua regia, heated at 160 °C for about ten minutes. To this solution an ionisation buffer was added in order to optimise detection of Pd and K. Since the spectrometers are more sensitive to atoms, analytical results can be improved due to the higher amount of Pd and K in their elementary state. Au exists preferably in its metallic state due to its high ionisation potential [69]. The buffer contained 1 mL of a 20 wt % CsCl solution and 1 mL of Schinkel's solution, consisting of CsCl (5-8 gL<sup>-1</sup> Cs) and LaCl (95-105 gL<sup>-1</sup> La). Both chlorides induced a shift of the reactants between an ionic and metallic state during measurement, illustrated by the chemical equations below. Ionisation of Cs freed one electron which could be used to form K<sup>0</sup>. A similar reaction occurred for La and Pd.



After adding deionised water the solution was heated for further ten minutes at 20 °C before analysing. Concentrations of Pd and Au were measured via AAS, as outlined before. In contrast, potassium was determined by using inductively coupled plasma optical emission spectrometry (ICP-OES; Spectro Modula). Values obtained by this advanced method were higher compared to results of the conventional analysis. Several possible explanations exist for this apparent increase of concentration. Since the remaining silica in the flame and plasma respectively can cause a temperature decrease, complete evaporation of silica after reaction to SiF<sub>4</sub> improves measurements both via AAS and ICP-OES. Due to the different excitation conditions at lower temperatures compared to the calibration standard, smaller concentrations would be measured. In addition, since only atoms can be identified via flame and plasma, employing an ionisation buffer helps by shifting the equilibrium from ions towards the more favoured atoms. This adjustment also leads to higher intensities, giving more precise and reproducible values. Furthermore, potassium is now detected via ICP-OES instead of AAS, achieving better results in the high concentration range, of about 60 mgL<sup>-1</sup>.

Another procedure which has further improved the analytical values derives from considering the ignition loss. For this additional step, loss on ignition (*LOI*) of the samples was obtained by calcination at 950 °C for three hours to dry the sample and remove all volatiles. The *LOI* value can be calculated as follows:

$$LOI[\%] = 100 - (m_{final} \cdot 100 / m_{initial}) \quad (3.1)$$

Based on this value, *LOI*-free concentration results can then be obtained by the equation below. It should be taken into account that all analytical results reported in this work are *LOI*-free.

$$c_{LOI-free}[\%] = 100 \cdot c_{analytic} / (100 - LOI) \quad (3.2)$$

### 3.5 VAM-Temkin test unit

The commercial test unit used in this study for evaluation of the high performance VAM catalysts will be the subject of this section. Since further information is available in [70],

only a brief overview will be provided in the following. In order to simulate an industrial fixed bed reactor with high throughput, a system of seven parallel reactor tubes was constructed. Each reactor consists of four modules with eight cavities, respectively. This design is based on the Temkin concept [58] and similar to the one described by the technical chemistry group of TU Darmstadt [60–63] (fig. 3.12), but varies in the number of cavities. In consequence, instead of 40 catalyst spheres, a total number of 32 per tube can be used for test purposes. However, the parallelisation of reactors in the unit used for this study represents a major advantage compared to the other system. The reactor tubes can be loaded with five different catalysts, which are tested under identical process conditions, referred to as a “library” in the following discussion. In general, the sixth reactor is loaded with the benchmark catalyst ( $B$ ) and the seventh with the unloaded KA carrier beads (dummy).  $B$  was chosen as a reference since it is similar to the state of the art catalyst employed in industry.



Figure 3.12: Design of modules used in the TUD reactor [60–62].

Contrary to a bench scale reactor where only a small part of the inserted catalyst spheres has contact to the reactor wall, this is enabled for each sphere placed in the separate cavities of this reactor. Due to the small distance between spheres and reactor wall, the reaction gas stream can pass over the beads from cavity to cavity. This ensures an efficient heat transport and avoids hot spots. For bench scale tests the formation of hot spots is reduced by mixing the catalyst spheres with silicon carbide or glass beads. However, this has detrimental influence on the mass transport during VAM reaction.

In summary, the advantages of this VAM Temkin test unit are:

- Efficient heat and mass transport
- Low pressure drop across the reactor
- Direct comparison due to parallelisation of reactors
- Testing with low amount of catalyst is possible

Figure 3.13 gives an overview of the experimental setup. All reactor tubes were arranged in an oil bath thermostat ensuring isothermal conditions. Pressure in the reactors was controlled by a back pressure valve. For testing feeds of different gases (ethylene, nitrogen, carbon dioxide and methane) were mixed prior to reaching the vaporiser. Acetic acid was then added to this gas mixture. Finally oxygen was added after the vaporiser in order to prevent concentrations exceeding the explosion limit. Subsequently the gas mixture was distributed via flow restrictors among the reactors. For the same safety reasons as outlined above, reactor effluents were diluted with nitrogen. For analysis via gas chromatography (GC) a small amount from each reactor flow outlet was successively sampled by a multi-position valve. Remaining flows not necessary for analysis were conducted to a condenser which was periodically emptied.

The gas flows during the first five hours of the overall testing protocol, including gradual addition of individual test components, are shown in figure 3.14. After having achieved the steady state test flow conditions for all required components, a catalyst activation phase of 16 hours followed. Subsequently VAM formation was studied via GC analysis within a 5.5 hour time frame at constant temperature (140 °C). The reactors were analysed one by one in strict rotation, in order to generate data for all tested catalysts. Each measurement was repeated three times. After completion of data for 140 °C, the temperature was set to 145 °C. The measurements were started after a five hour equilibration period. Thus, isothermal conditions could be ensured. This sequence was continued for 150 °C and finally again for 140 °C to check for deactivation. These temperatures were selected to achieve performance results at operating O<sub>2</sub> conversions of 40-60 % used in industrial VAM production plants.

Methane was chosen as normalisation standard since it is not involved in VAM formation and is added in industrial processes to increase the explosion limit of oxygen

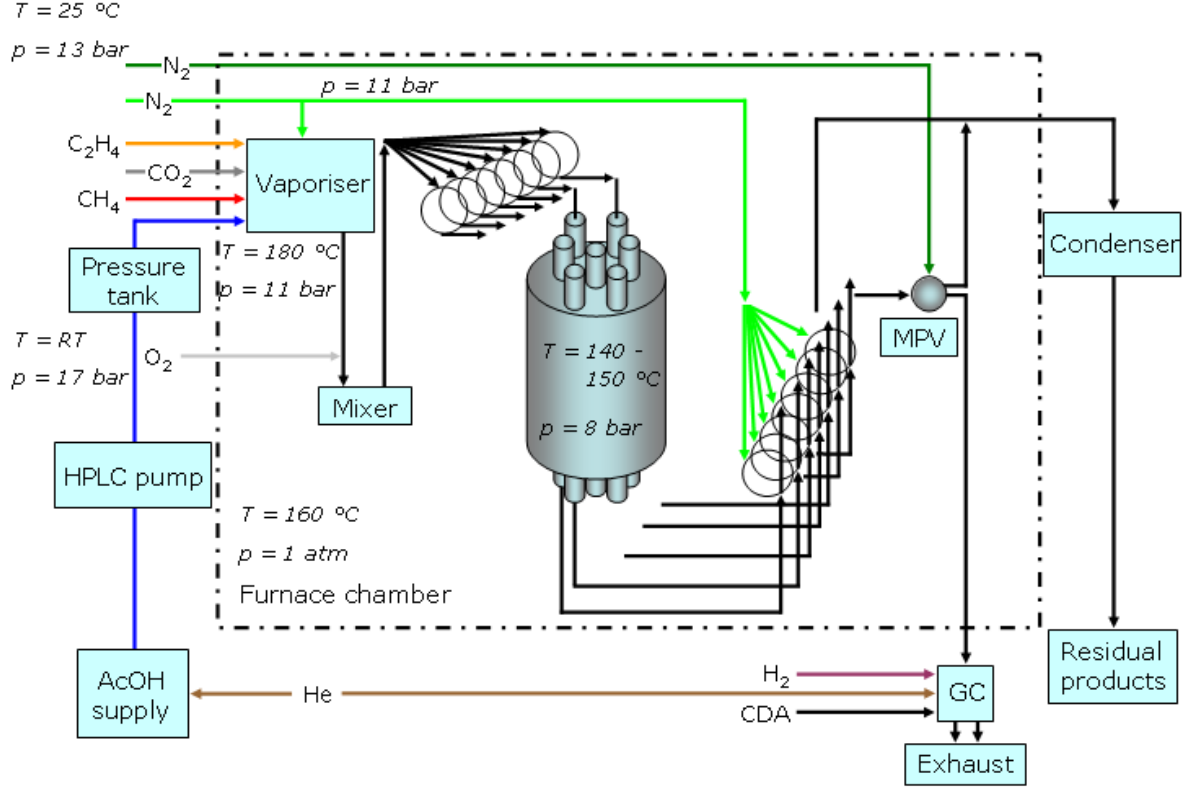


Figure 3.13: Flow chart of VAM-Temkin test unit.

from 6 % to 8 %. For comparison of all synthesised catalysts, GC results from the inert material (labelled with index 0) in reactor seven were used as a reference for determination of conversion ( $C$ ), selectivity ( $S$ ) and space time yield ( $STY$ ), as outlined below. The relative concentration derived from GC peak areas of a component  $i$  ( $O_2$  or VAM), normalised to methane, is labelled with  $c_{i,methane}$  in the following equations. Both a chromatogram example and a sample calculation of the performance results are given in appendix A.

$$C_{O_2} = \frac{c_{O_2,methane}^0 - c_{O_2,methane}}{c_{O_2,methane}^0} \quad (3.3)$$

Assuming that the ethylene combustion discussed in chapter 1 is the only competitive reaction occurring during VAM formation, selectivity for the favoured product can be calculated as presented below:

$$S_{VAM} = \frac{c_{VAM,methane}}{c_{VAM,methane} + 1/2 \cdot c_{CO_2,methane}} \quad (3.4)$$

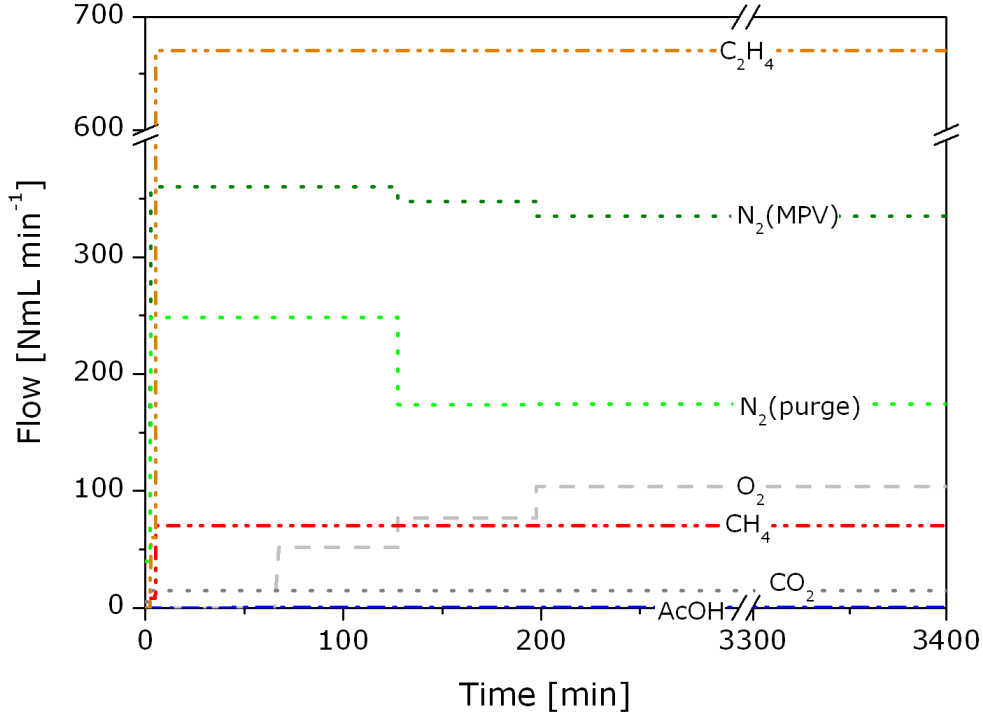


Figure 3.14: Start-up protocol for flows during test procedure to evaluate different VAM catalysts.

In order to represent the catalyst productiveness, space time yield was additionally calculated based on the catalyst amount used during screening.

$$STY_{VAM} = \frac{\dot{n}_{VAM}}{V_{S,cat}} = c_{VAM, methane} \cdot c_{methane}^0 \cdot \frac{M_{VAM}}{V_m} \cdot \frac{n_{cat} \text{ L}^{-1}}{n_{cat,R}} \quad (3.5)$$

The bulk volume ( $V_{S,cat}$ ) was obtained by filling a cylinder of 1 L volume completely with catalyst spheres. Subsequently the added spheres were counted ( $n_{cat}$ ) resulting in  $6431 \text{ L}^{-1}$ . As previously mentioned the number of spheres for each reactor ( $n_{cat,R}$ ) was 32. Performance of VAM catalysts was studied at a total reactor flow of  $250 \text{ NmLmin}^{-1}$  and 8 bar for several temperatures. Validation of this VAM-Temkin test unit was conducted in a previous work [70]. Due to the presented Temkin concept, the calculated error of measurement is relatively low regarding both selectivity ( $\pm 0.25 \%$ ) and space time yield ( $\pm 5 \%$ ). The resulting  $C$ - $S$  and  $C$ - $STY$  master curves will be shown in section 4.1.

# Chapter 4

## Performance results and data reduction

### 4.1 Catalyst screening

In order to classify all synthesised catalysts used for the selective oxidation of ethylene and acetic acid to VAM, selectivities and space time yields were measured according to section 3.5 at varying temperatures. The obtained selectivity master curves for different catalyst series, reduced in the liquid phase (squares) (*cf.* section 3.2.2) or in the gas phase (points) (*cf.* section 3.3) are shown as examples in figures 4.1 and 4.2 compared to the previously mentioned reference *B* (triangles). Due to the advantages of the used VAM-Temkin test unit, especially in heat and mass transport (*cf.* section 3.5), selectivities could be measured with an accuracy of  $\pm 0.25\%$ . Additional master curves illustrating the selectivity of catalysts mentioned in this thesis are summarised in appendix B. Concerning all further results it should be noted that even the benchmark catalyst *B* is already significantly better in performance than other comparable state-of-the-art catalysts.

As expected, an increase in process temperature and  $\text{O}_2$  conversion, respectively, leads to lower VAM selectivity. Comparison within the catalysts synthesised using base mixtures by LPR (fig. 4.1) reveals similar selectivities within the estimated error range of  $\pm 0.25\%$ . However, it can be seen that catalysts *EX6152* and *EX6312* are

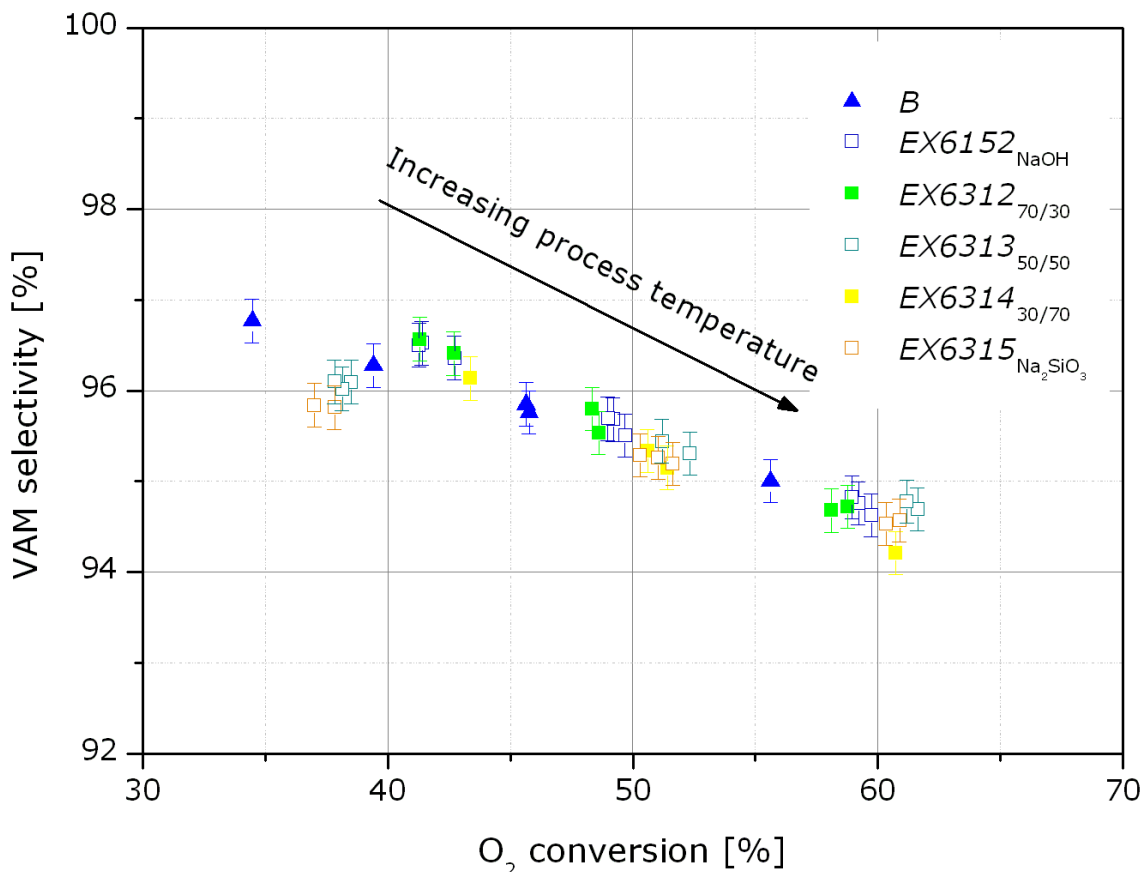


Figure 4.1: Comparison of VAM selectivity at varying temperatures for the liquid phase reduced catalysts with different NaOH/Na<sub>2</sub>SiO<sub>3</sub> mixtures as precipitating agent, studied at a reactor flow of 250 NmLmin<sup>-1</sup> and a pressure of 8 bar. The selectivity data of the benchmark  $B$  is also shown for this test library. The flows in NmLmin<sup>-1</sup> of all test components are as follows:  $F_{CO_2} = 15$ ,  $F_{N_{2,purge}} = 174$ ,  $F_{N_{2,MPV}} = 335$ ,  $F_{CH_4} = 70$ ,  $F_{C_2H_4} = 670$ ,  $F_{AcOH} = 0.54$ ,  $F_{O_2} = 104$ .

slightly more selective than the analogues precipitated with Na<sub>2</sub>SiO<sub>3</sub> enriched agents. Furthermore, it was revealed that according to these results, no significant advantage compared to  $B$  can be achieved by applying base mixtures for precipitation.

Using GPR to synthesise VAM catalysts seems to be more promising, when compared to the liquid phase reduced benchmark  $B$  (fig. 4.2). Catalyst  $EX8138$  ( $T_{red} = 400^\circ\text{C}$ ), in particular, shows outstanding selectivity compared to the analogues reduced at other temperatures, which are among themselves rather similar. This result can be explained by increasing mobility of unselective Pd atoms and small clusters resulting in agglom-

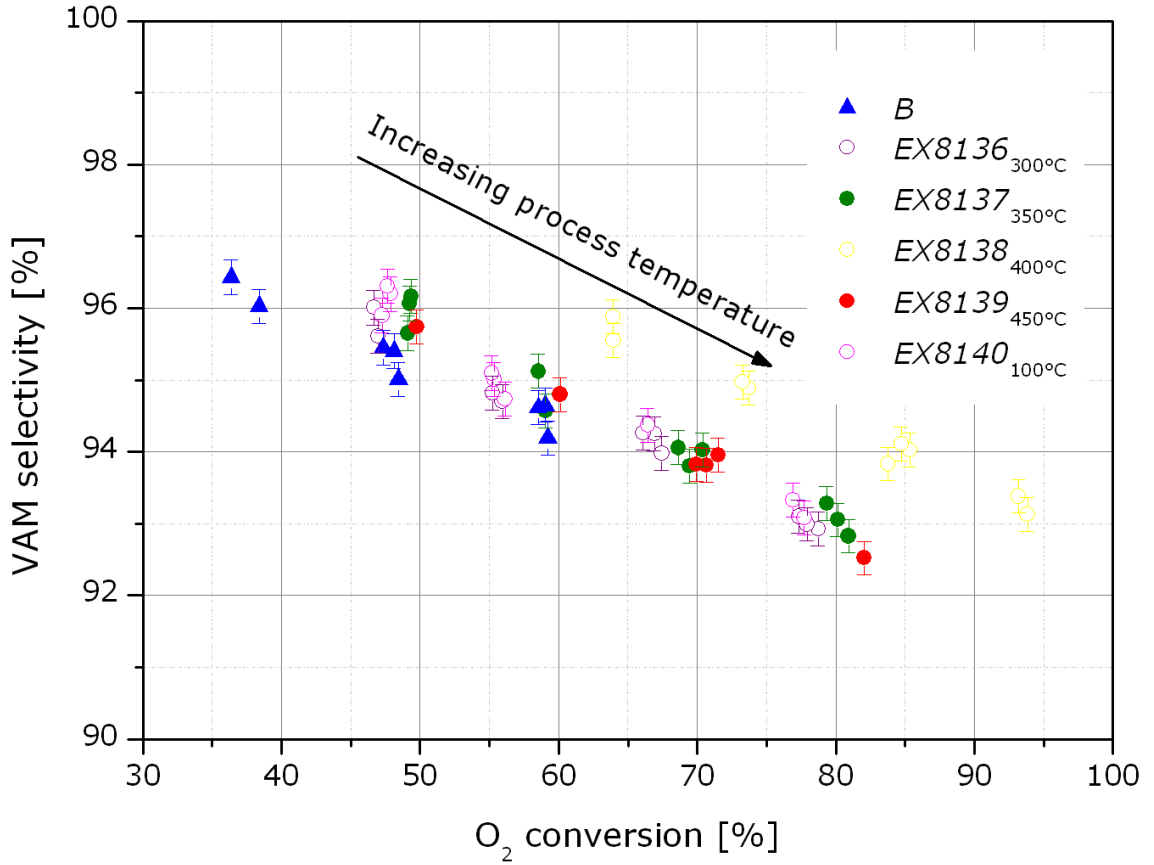


Figure 4.2: Comparison of VAM selectivity for several gas phase reduced catalysts using reduction temperature variation. The selectivity data of the benchmark *B* is also shown.

erated bigger nanoparticles when using higher reduction temperatures. According to the present measurements  $T_{red} = 400^\circ\text{C}$  seems to describe the optimum temperature in regard to selectivity. This sample reaches approximately 95 % O<sub>2</sub> conversion without any indication of total combustion, which would lead to rapid thermal damage of the catalyst [64, 71]. Heat transport is therefore revealed to proceed very efficiently in the test unit presented here. In order to generate selectivity data at lower conversions, catalyst *EX8138* could be operated at lower temperatures such as  $135^\circ\text{C}$ , to simultaneously improve the selectivity.

Further gas phase reduced catalysts were screened in different test libraries. A meaningful performance ranking of the samples is provided by a relative comparison of the selectivity to the benchmark at 50 % O<sub>2</sub> conversion. These values were obtained by

a linear fit for each catalyst data set. The approach is illustrated in figure 4.3 on the example of catalyst *EX6152* and was carried out in the same manner for all tested catalysts, including the benchmark *B*. In the following table 4.1, the calculated results of absolute selectivity are presented for the base mixture series. In addition, the relative selectivities compared to *B* ( $Dev_{rel}(S_{VAM})_{EX6152} = 1 - \frac{95.45}{95.62} = +0.17\%$ ) are given. However, an extrapolation was necessary in a few cases in order to generate a selectivity value at 50 % conversion, *i. a.* for *EX8138*.

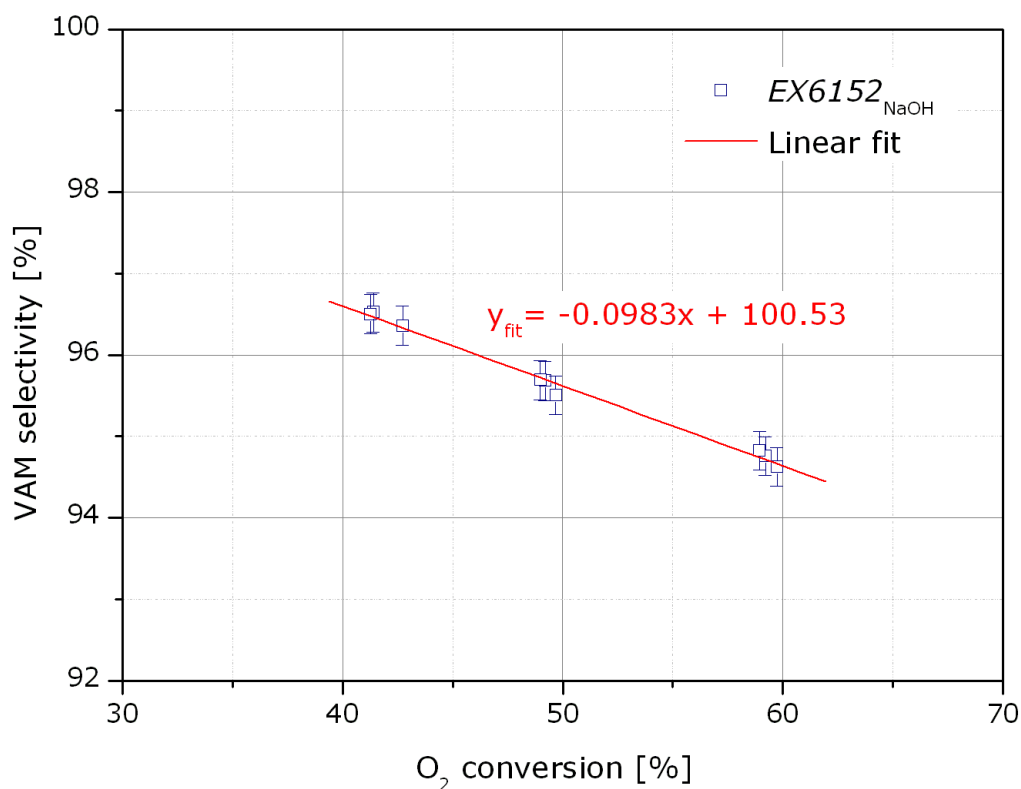


Figure 4.3: Experimental data set of selectivity for catalyst *EX6152*. According to the linear fit a VAM selectivity of 95.62 % is obtained at 50 % O<sub>2</sub> conversion.

Table 4.1: Average results of absolute selectivity calculated at 50 % O<sub>2</sub> conversion for catalysts of the base mixture series and the reference *B* including a relative comparison of these values.

<i>EX No.</i>	<i>6152</i>	<i>6312</i>	<i>6313</i>	<i>6314</i>	<i>6315</i>	<i>B</i>
$S_{VAM}$ [%]	95.62	95.58	95.42	95.38	95.21	95.45
$Dev_{rel}(S_{VAM})$ [%]	+0.17	+0.13	-0.03	-0.07	-0.26	

Selectivity deviations  $Dev_{rel}(S_{VAM})$  with respect to the benchmark  $B$  calculated for this series and for all catalysts presented in this thesis are schematically illustrated in figure 4.4. This summary identifies the prepared VAM catalysts referring to the varied synthesis parameters. The individual series of experiments are represented in different colours. In addition LPR and GPR are distinguished by two different bar designs. As previously mentioned catalyst selectivity was measured in a few cases at higher conversion ranges. These catalyst samples are labelled in the following overview with an asterisk.

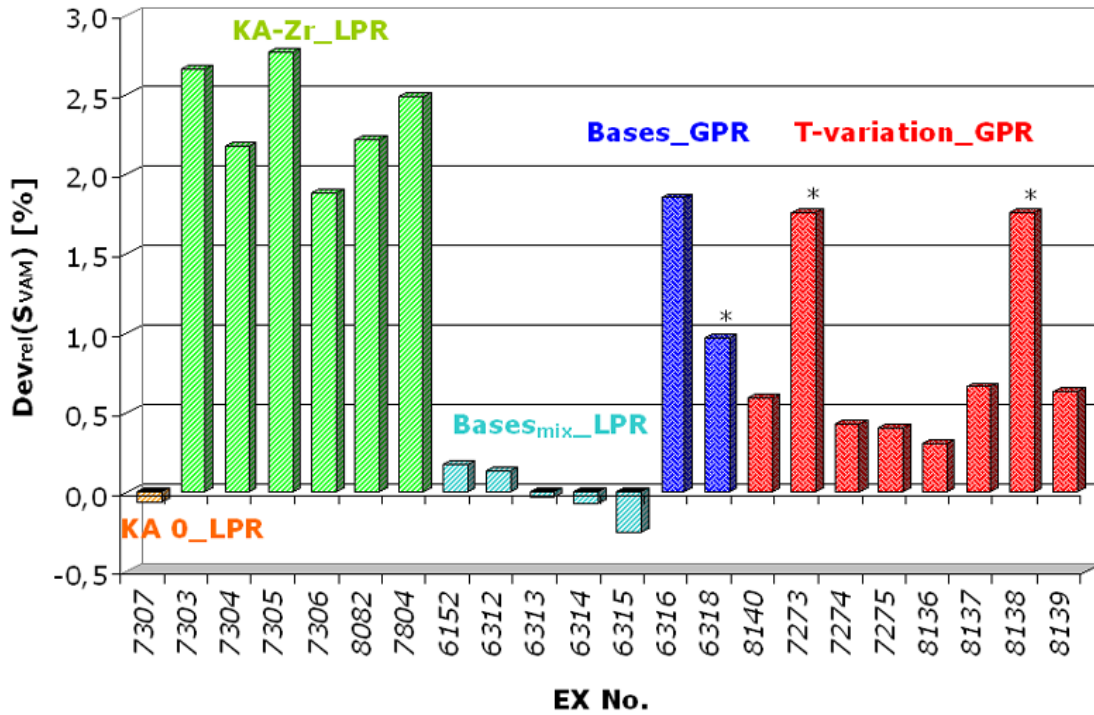


Figure 4.4: Comparison of selectivity at 50 % O<sub>2</sub> conversion for all synthesised catalysts relative to the benchmark  $B$ .

Due to the higher average pore diameter in the catalyst carrier KA 0 compared to KA 160 (*cf.* sec. 3.2.1), higher selectivities were expected for *EX7307* (labelled in orange) based on this support [64]. However, its selectivity is comparable to the benchmark synthesised with a KA 160 carrier. The highest improvements in selectivity were achieved, according to this overview, by the Zr-based carrier catalysts (green), followed by samples of GPR (blue and red). Within the Zr-series catalysts *EX7303*, *EX7305* and *EX7804* are on average about 20 % more selective than the remaining three analogues representing different Zr amounts.

As previously mentioned, NaOH enriched precipitation (*EX6152* and *EX6312*) results in slightly more selective catalysts using LPR (turquoise). However, this trend cannot be confirmed for the reduction in gas phase (blue). Higher selectivity is obtained in this case by using  $\text{Na}_2\text{SiO}_3$  (*EX6316*,  $S_{VAM} = 96.39\%$ ) as precipitating agent compared to NaOH (*EX6318*,  $S_{VAM} = 95.52\%$ ).

Final evaluation of all catalysts reduced in the gas phase at several temperatures reveals *EX7273*<sub>150 °C</sub> ( $S_{VAM} = 95.21\%$ ) and *EX8138*<sub>400 °C</sub> ( $S_{VAM} = 96.88\%$ ) to be about 70% on average more selective than samples reduced at other temperatures. Considering the previously mentioned error range, comparable selectivities are obtained among these remaining samples. However, comparing all observed data to the selectivity of benchmark *B*, it can be concluded that the majority of synthesised catalysts can compete with this highly selective standard applied for the present study.

Since space time yield is characteristic for the efficiency of VAM formation, catalyst comparison with regard to this performance parameter will be subsequently shown in the same manner as previous selectivity analysis. The obtained *STY* data is given below for the same catalyst series (fig. 4.5 and 4.6). Further *STY* master curves of all catalysts mentioned herein are displayed in appendix C. The calculated error of measurement was estimated to  $\pm 5\%$  for the *STY* (*cf.* sec. 3.5).

These results confirm an increase of *STY* with process temperature, since this correlation exists for almost every catalytic system. With regard to catalysts of the base mixture series, displayed in figure 4.5, a similar range of activity values was observed. This result suggests that significant optimisation in *STY* cannot be provided by  $\text{Na}_2\text{SiO}_3$  precipitation. However, these catalysts are about 10% more active than the benchmark, as the overview of all catalysts will subsequently show.

Differences between the reference *B* and the investigated catalysts become more evident using GPR. Figure 4.6 shows that GPR leads to an enormous increase of *STY*, indicating that significantly more VAM was produced using these catalysts compared to the liquid phase reduced benchmark. In addition, comparison of all catalysts tested in this library reveals again that the performance of *EX8138* is considerably higher compared to the experimental analogues. This confirms the consistency of both measured data (*S* and *STY*). Within these remaining samples activity is decreasing in the

following order:  $EX8137 \geq EX8139 > EX8136 > EX8140$ .

In order to provide an overview on the synthesised catalysts, the average  $STY$  at  $145^\circ\text{C}$  process temperature was chosen. Based on these values, the relative deviation from  $B$  as benchmark was calculated. The results are given in the following table 4.2 as an example for the base mixture series reduced with  $\text{NaH}_2\text{PO}_2$ .

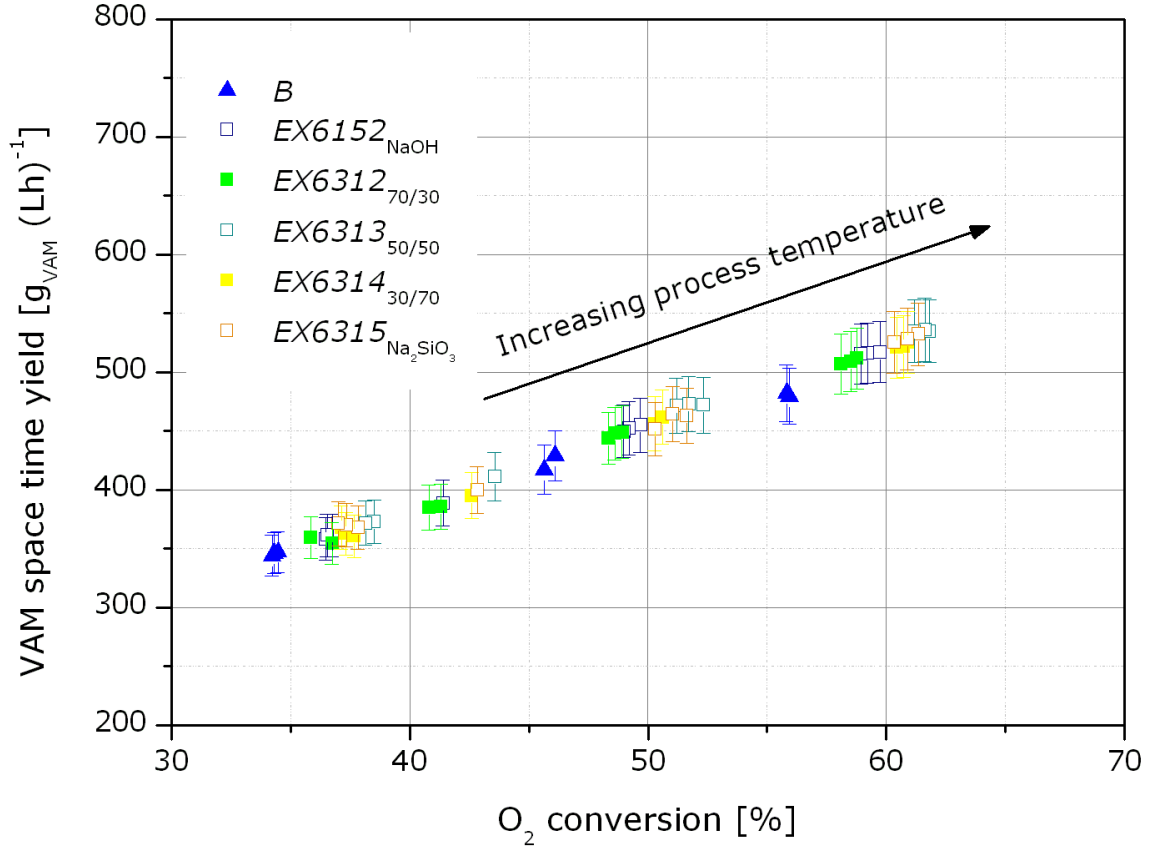


Figure 4.5: Comparison of activity for the liquid phase reduced catalysts with different  $\text{NaOH}/\text{Na}_2\text{SiO}_3$  mixtures as precipitating agent. The  $STY$  data of the benchmark  $B$  used in this test library is also shown.

In figure 4.7 the entire overview of catalysts is depicted relative to the reference  $B$ . Nearly all of the systematic variations applied to VAM catalyst synthesis in this study resulted in significant improvements of activity compared to the benchmark.

Whereas the KA 0 carrier gains about 6 % in activity compared to  $B$ , the Zr-based supports (except  $EX7804$ ) achieve even 16 % on average. Within the Zr-series catalyst  $EX7804$  is found to be as active as the benchmark. The other Zr-based specimens

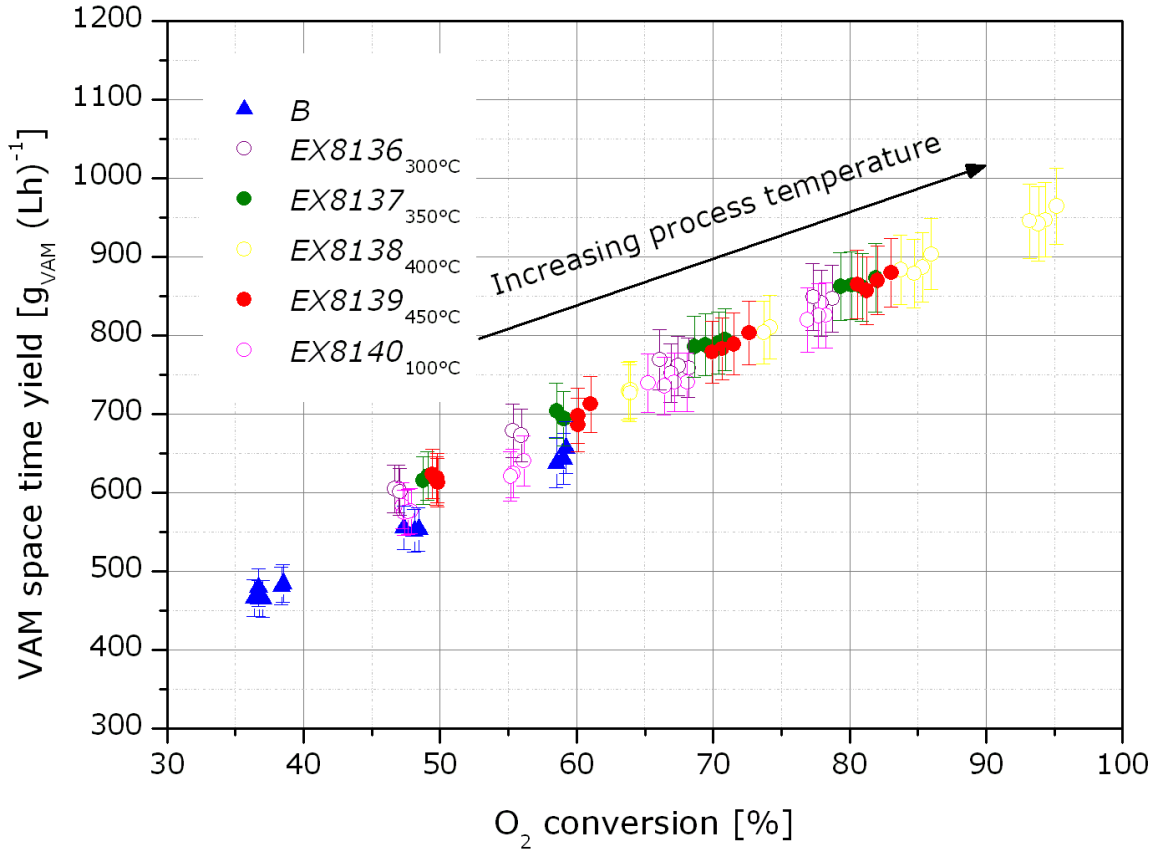


Figure 4.6: Comparison of activity for several gas phase reduced catalysts using reduction temperature variation. The *STY* data of the benchmark *B* is also shown.

Table 4.2: Averaged absolute *STY* results measured at 145 °C process temperature for catalysts of the base mixture series and the applied benchmark *B* including their relative comparison.

<i>EX No.</i>	<i>6152</i>	<i>6312</i>	<i>6313</i>	<i>6314</i>	<i>6315</i>	<i>B</i>
$STY_{VAM}$ [g <sub>VAM</sub> Lh <sup>-1</sup> ]	452	446	472	457	460	410
$Dev_{rel}(STY_{VAM})$ [%]	+9.25	+7.88	+13.03	+10.19	+10.68	

show among themselves a relatively small deviation in activity. Compared to these samples, the VAM catalysts synthesised with different base mixtures using LPR are approximately 30 % less active. However, in this series the Na<sub>2</sub>SiO<sub>3</sub> enriched precipitating agents result in slightly more active catalysts. By contrast, the GPR analogues reveal the opposite trend. The activity of *EX6316* (Na<sub>2</sub>SiO<sub>3</sub> precipitation) is about 8 %

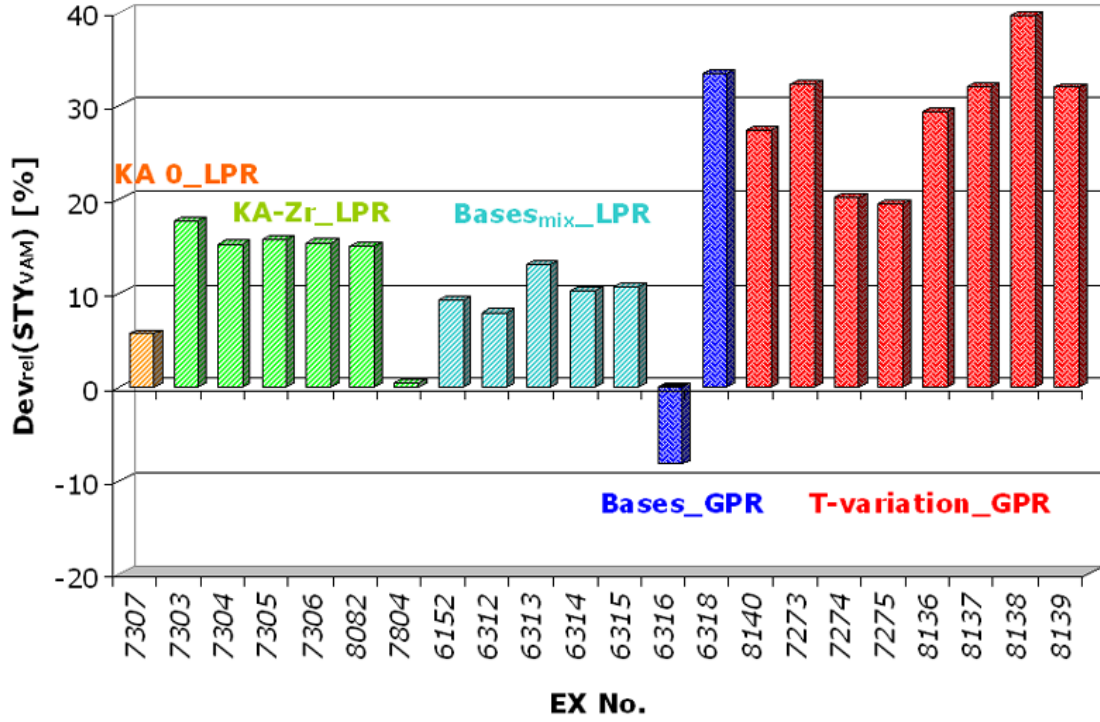


Figure 4.7: *STY* comparison relative to the reference *B* measured at 145 °C process temperature.

lower than *B*, whereas catalyst *EX6318* (NaOH precipitation) results in approximately 33% more *STY* compared to the benchmark. In general, higher activity is apparently arising due to GPR. The highest *STY* of almost 40% is achieved by catalyst *EX8138*, which was reduced via forming gas at 400 °C. Since its improved selectivity reduces the CO<sub>2</sub> formation, less heat is produced and less oxygen is consumed by this unselective reaction which in turn increases the *STY*.

Finally, the combination of all obtained selectivity and activity data enables a classification of the catalysts presented herein. *STY* improvements were revealed to attain about 40%. An increase in selectivity was reached up to approximately 3%. Regarding the carrier variation, Zr-based supports are more promising in performance than KA 0. Although the experimental series applying different bases associated with LPR results in slightly higher activity than the benchmark, it is not competitive with the other catalyst series. In contrast to LPR, precipitation with Na<sub>2</sub>SiO<sub>3</sub> using GPR (*EX6316*) increases the selectivity due to lower shell thickness (*cf.* sec. 4.2.2), but associated with unfavourable loss in activity. Catalysts obtained by temperature variation

during reduction in the gas phase are, due to their outstanding activity and improved selectivity, preferred to the other series. In summary, the three best catalysts reviewed in this study are *EX7273*, *EX8138* and *EX7305*. By means of the characterisation methods presented in the following section, the previously outlined selectivity and activity results of the synthesised catalysts will be correlated with different parameters such as elemental composition and structural configuration.

## 4.2 Characterisation of VAM catalysts

### 4.2.1 Wet chemical analysis (ICP-OES, AAS)

A wet chemical analysis was carried out among other characterisation methods at SCAG on all synthesised VAM catalysts, using ICP-OES and AAS in order to elucidate differences in element concentration and to verify specification limits and metal retention, respectively. Details of the analytical procedure are described in section 3.4. In the following sections the analytical results obtained for VAM catalysts prepared with varying synthesis parameters will be presented. All measured values are represented relative to the amount of each element applied during catalyst synthesis. Since catalyst *B* was selected as reference, its data will additionally be considered for further comparison. For all synthesised catalysts the absolute metal amounts range as follows:

- Pd = 0.8-1.1 wt %
- Au = 0.3-0.6 wt %
- K = 2.8-3.3 wt %
- Cl  $\leq$  250 ppm

In general, a decrease in the concentrations of Pd and Au can be explained by abrasion during unit operations such as for example precipitation and reduction. Apart from that effect, assuming similar precious metal amounts for synthesis of all catalysts presented herein, metal loss is assumed to be seriously affected by the use of different bases and the selection of the reduction medium. However, both metal components Pd and Au are important for VAM formation and should therefore be maintained close

to their specification values. By contrast, the concentration of chloride acting as a catalyst poison is preferred to be as low as possible. Since potassium, added as acetate solution in a final impregnation stage, is indispensable for good performances of VAM catalysts, its value was additionally analysed for control purposes.

Table 4.3 displays the analytical results for VAM catalyst *EX7307* based on the KA 0 carrier (*cf.* sec. 3.2.1.1) compared to the proprietary benchmark *B*. As shown in this table, some element concentrations vary strongly from the reference specification values (*Dev* = deviation). The previously determined marginal difference in activity compared to the reference can be attributed to the presence of less Pd in this catalyst. However, the concentration of Au is significantly higher than that in the benchmark. For both catalysts, the measurements revealed that the chloride concentration was halved in comparison with the specification value. The notably lower potassium concentration of *EX7307* compared to the standard is assumed to additionally affect the performance of the KA 0 based catalyst. It should be noted that the error in measurement for the potassium concentration is assumed to be larger than for the three other components due to the volatilisation of KOAc.

Table 4.3: Analytical results for *EX7307* based on KA 0 carrier compared to the reference *B*.

<i>EX No.</i>	<i>7307</i>	<i>B</i>
$Dev_{Pd}$ [%]	-1.1	+0.4
$Dev_{Au}$ [%]	+1.2	-8.6
$Dev_{K^+}$ [%]	-15.6	-2.8
$Dev_{Cl^-}$ [%]	-41.0	-65.0

In order to compare catalysts synthesised with different KA-Zr carriers as supports (*cf.* sec. 3.2.1.2), the amounts of Pd, Au,  $K^+$  and  $Cl^-$  in these catalysts were also determined via wet chemical analysis. As table 4.4 shows, significant metal loss occurs for catalyst *7804* which may derive from a short impregnation time. Due to the metal loss the determined low activity of this catalyst (*cf.* fig. 4.7) can be explained. In addition, the measured chloride deviation for this catalyst is less preferable compared to the other Zr-based analogues since, as previously mentioned, deviations towards

lower values are advantageous for this parameter. For the remaining catalysts, chloride concentrations average 58.4 % and hence lie far below the specification limit. However, no correlation was found between the noble metal concentrations presented for this series and the amount of Zr in the carrier.

Table 4.4: Analytical results for VAM catalysts with different KA-Zr carriers as support.

<i>EX No.</i>	<i>7303</i>	<i>7304</i>	<i>7305</i>	<i>7306</i>	<i>7804</i>	<i>8082</i>
<i>Dev<sub>Pd</sub></i> [%]	+3.3	+2.8	-0.6	+3.9	-8.9	-4.4
<i>Dev<sub>Au</sub></i> [%]	+1.2	+3.7	+4.9	+1.2	-13.6	-1.2
<i>Dev<sub>K+</sub></i> [%]	-1.6	-10.9	-6.3	-14.1	-12.5	-0.5
<i>Dev<sub>Cl-</sub></i> [%]	-66.8	-58.8	-63.8	-50.0	-3.8	-52.5

The following table 4.5 depicts elemental concentrations determined in the catalysts obtained in a precipitation step with different base mixtures of NaOH and Na<sub>2</sub>SiO<sub>3</sub> (*cf.* sec. 3.2.2). As previously mentioned, metal loss is expected to be lower for samples precipitated with Na<sub>2</sub>SiO<sub>3</sub> enriched agents compared to NaOH, due to lower alkalinity. However, this effect is only observed for Au, as shown by comparison of noble metal concentrations in the catalysts. This may be attributed to the fact that Au<sup>3+</sup> precipitated on the catalyst surface redissolves more easily than Pd during the contact with the fixation solution [72]. However, the analytical results for both noble metals are on average 7 % (Pd) and 15.9 % (Au), respectively, lower than the calculated specification values. This implies high losses during precipitation and reduction for the two species. The obtained chloride concentrations are nearly equal within this series. The average deviation for Cl<sup>-</sup> (60.6 % below the specification limit) is considered as advantageous. Measurements of potassium concentration could not be performed due to low remaining sample amounts. Since all these samples achieved approximately similar performance data, also compared to the reference *B*, no further statement with regard to the influence of element concentrations can be made for this series.

As illustrated in the previous section, differences in performance were revealed between VAM catalysts precipitated with NaOH and Na<sub>2</sub>SiO<sub>3</sub> using GPR (*cf.* sec. 3.2.3). The analytical results in table 4.6 confirm that the metal retention is increased when us-

Table 4.5: Analytical results of VAM catalysts synthesised with base variations.

<i>EX No.</i>	<i>6152</i>	<i>6312</i>	<i>6313</i>	<i>6314</i>	<i>6315</i>
<i>Dev<sub>Pd</sub></i> [%]	-6.2	-6.2	-7.2	-8.2	-7.2
<i>Dev<sub>Au</sub></i> [%]	-18.2	-18.2	-13.6	-15.9	-13.6
<i>Dev<sub>Cl-</sub></i> [%]	-55.0	-62.0	-64.5	-62.0	-59.5

ing  $\text{Na}_2\text{SiO}_3$  rather than  $\text{NaOH}$ . Deviations for Au and Pd are lower due to application of the less alkaline agent. Concentrations of chloride found in these two catalyst species are below the specification limit as for all previously mentioned catalysts. However, it can be stated that catalysts reduced in gas phase do not achieve  $\text{Cl}^-$  concentrations as low as their liquid phase reduced analogues. Although *EX6318* and *EX6316* were washed three hours longer than the corresponding samples of LPR *EX6152* and *EX6315* (*cf.* tables 3.11, 3.9), their chloride concentration is about two to three times higher. A possible reason for this discrepancy between both reduction media has been previously described in section 3.3. Due to additional washing during LPR, chlorides can diffuse into solution. Since dissolution of chlorides is avoided in the case of GPR, more chlorides remain in the catalyst spheres.

Table 4.6: Analytical results of VAM catalysts reduced in gas phase using different bases.

<i>EX No.</i>	<i>6318</i>	<i>6316</i>
<i>Dev<sub>Pd</sub></i> [%]	-3.1	+2.1
<i>Dev<sub>Au</sub></i> [%]	-18.2	-15.9
<i>Dev<sub>Cl-</sub></i> [%]	-15.0	-27.5

Since performance data revealed that GPR in VAM catalyst synthesis is preferable, another parameter than chloride concentration is assumed to be more dominant. With regard to metal retention of Pd and Au, samples of GPR are favoured since they deviate to a lesser extent from the Pd specification limit. Values for Au concentration in both catalyst specimens do not show any trend. It seems that whichever of the presented bases is used for precipitation, replacing LPR by using forming gas can be a reasonable approach. This statement will be object of further discussion.

A comparison of the conducted plant certification trials *B* (LPR) and *D* (GPR) (*cf.* sec. 3.3) confirms the tendencies observed between both reduction media for the laboratory scale catalysts. As table 4.7 summarises, values of Pd throughout these specimens are above the specification value. Besides, it becomes obvious that Pd values are constantly higher for GPR (*EX7273-EX7275* and *EX8136-EX8140*). However, higher deviations from the Au specification limit indicate lower concentrations of Au in catalysts prepared using GPR compared to LPR. Again the liquid phase reduced reference *B* shows a slightly lower concentration of chloride than forming gas reduced catalysts resulting from *D*, although its wash time was about four hours shorter. Among the *D* catalysts the highest discrepancies are determined for  $K^+$  and Pd concentrations. The metal loss of Au varies for these specimens by about 13.5%. In general, it is difficult to establish a correlation between these data and the previously introduced performance of each catalyst.

Table 4.7: Analytical results for VAM catalysts obtained by plant certification trials, varying in reduction medium and temperature.

<i>EX No.</i>	<i>B</i>	<i>8140</i>	<i>7273</i>	<i>7274</i>	<i>7275</i>	<i>8136</i>	<i>8137</i>	<i>8138</i>	<i>8139</i>
<i>Dev<sub>Pd</sub></i> [%]	+0.4	+2.2	+2.2	+2.2	+3.2	+3.2	+3.2	+2.2	+4.3
<i>Dev<sub>Au</sub></i> [%]	-8.6	-18.5	-16.0	-16.0	-16.0	-18.5	-16.0	-18.5	-18.5
<i>Dev<sub>K+</sub></i> [%]	-2.8	-3.1	±0	±0	-3.9	-6.3	-3.1	-6.3	-3.1
<i>Dev<sub>Cl-</sub></i> [%]	-65.0	-37.5	-60.0	-61.5	-59.0	-61.5	-56.5	-56.5	-49.0

### 4.2.2 Optical microscopy

As previously described in section 3.2.2, high selectivities can be preferably obtained by having rather thin and uniform shells in the VAM catalyst carrier particles. However values of shell diameter that are too low would result in inactive catalysts. In order to determine the influence of shell thickness on catalytic performance, 10-20 spheres of each catalyst presented herein were analysed using an optical microscope at SCAG (Leitz, 10:1 magnification). The catalysts were cut into two hemispheres and the shell thickness was measured for each half at four different positions with increments of

90°. An average value was calculated to compare the different catalysts. The error is estimated to be approximately 10  $\mu\text{m}$ .

In the following table 4.8 the shell thicknesses of different KA carriers are summarised. Previous experiments showed that a shell thickness of about 300-400  $\mu\text{m}$  impairs the mass transport. Values lower than 100  $\mu\text{m}$  lead to high metal distribution throughout the sphere resulting in heat transport problems. Since the optimum shell thickness is supposed to be 200  $\mu\text{m}$ , both the values obtained for *EX7307* synthesised with KA 0 as support and for the reference *B* based on KA 160 are too high. It can be concluded from this data that the performance data of *EX7307* could be improved by achieving thinner shells.

Table 4.8: Comparison of shell thicknesses for VAM catalysts based on KA 0 and KA 160 carrier.

<i>EX No.</i>	<i>7307</i>	<i>B</i>
Carrier	KA 0	KA 160
Shell thickness [ $\mu\text{m}$ ]	295.8	330.0

According to section 3.2.1.2, carriers based on different Zr amounts were synthesised to determine the optimum concentration for high performance catalysts [54]. In general, zirconium is known to enhance the selectivity and activity of VAM catalysts either by using it as oxidic support [65, 66] or by impregnating the adequate metal salts [55]. It was suggested that not all Zr carriers allow consistent shell formation. The overview in table 4.9 confirms this assumption especially for higher Zr concentrations around 8-19%. These catalysts labelled in red reveal blurred shells, as illustrated in figure 4.8 by comparison between *B* and *EX8082*. Repetition of syntheses for *EX7306* and *EX8082* confirmed this result. The optimum Zr concentration to obtain consistent shells consequently ranges between 2 and 7%. In addition, the lower shell thicknesses observed for catalysts *EX7303*, *EX7305* and *EX7804* result in higher selectivities due to improved mass transport as previously presented in figure 4.4. Furthermore, this performance parameter is supported for catalysts *EX7305* and *EX7804* by low BET surface areas, resulting in bigger pores (*cf.* tab. 3.5) compared to the other Zr-based samples.

Table 4.9: Shell thicknesses for VAM catalysts synthesised with different KA-Zr supports. Samples with blurred shells are displayed in red colour.

<i>EX No.</i>	<i>7303</i>	<i>7304</i>	<i>7305</i>	<i>7306</i>	<i>7804</i>	<i>8082</i>
Zr [%]	5-7	4-6	3-5	17-19	2-4	8-12
Shell thickness [ $\mu\text{m}$ ]	212.3	285.7	232.0	312.2	246.5	280.8

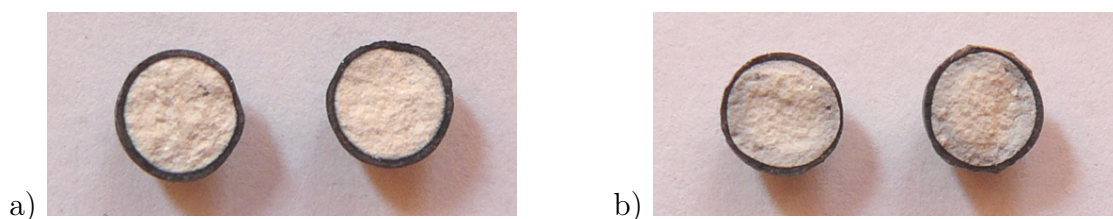


Figure 4.8: Images of catalyst hemispheres for a) *B* and b) *EX8082* showing that too high concentrations of Zr in the carrier impair shell formation.

Table 4.10 depicts the different shell thicknesses of the catalysts precipitated using base mixture variation and LPR. It is evident that an increase of  $\text{Na}_2\text{SiO}_3$  compared to NaOH during precipitation results in a decrease of the shell thicknesses.

Table 4.10: Shell thicknesses for VAM catalysts using different NaOH/ $\text{Na}_2\text{SiO}_3$  mixtures and LPR.

<i>EX No.</i>	<i>6152</i>	<i>6312</i>	<i>6313</i>	<i>6314</i>	<i>6315</i>
NaOH/ $\text{Na}_2\text{SiO}_3$	100/0	70/30	50/50	30/70	0/100
Shell thickness [ $\mu\text{m}$ ]	229.8	284.8	209.8	199.8	179.3

The obtained correlation may originate from higher molecular size of the less alkaline base compared to NaOH. As a result, diffusion into the spheres occurs slower and the back diffusing noble metal chlorides precipitate preferably in the outer regions of the spheres, as schematically presented below (fig. 4.9). However, the thinner shells observed for catalysts precipitated with  $\text{Na}_2\text{SiO}_3$  enriched agents do not lead to higher selectivity as expected. It can be therefore supposed that another parameter dominates the difference in selectivity. So far, the comparison of these bases was not subject

in literature for VAM catalyst synthesis. But it is known that VAM catalysts are synthesised with  $\text{Na}_2\text{SiO}_3$  as precipitating agent resulting in good performing catalysts [9, 42, 48].

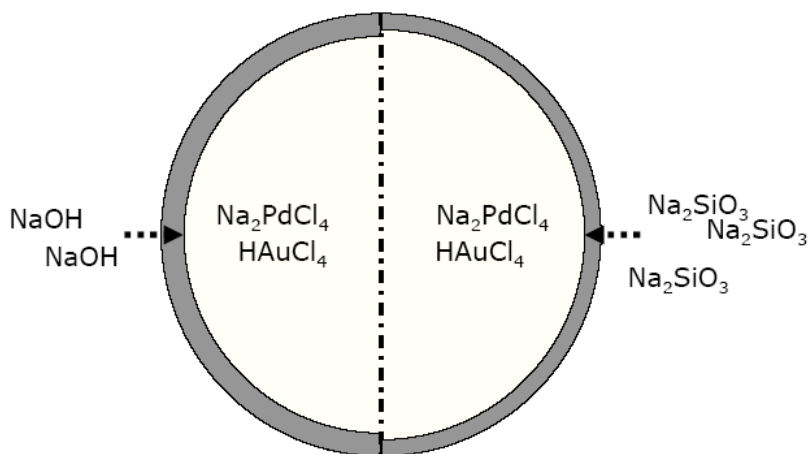


Figure 4.9: Influence of structural dimensions of the base on shell thickness illustrated for  $\text{NaOH}$  and  $\text{Na}_2\text{SiO}_3$ .

In order to elucidate the differences described in performance for catalysts precipitated by both bases and reduced via forming gas, shell thicknesses were measured (tab. 4.11). According to these data, the combination of  $\text{Na}_2\text{SiO}_3$  precipitation and GPR leads to very thin shells of only  $135\ \mu\text{m}$ . Since this value is significantly lower than for  $\text{NaOH}$ , the previously mentioned difference between both bases can also be confirmed for GPR. However, contrarily to LPR, low shell thickness of GPR catalysts results in high selectivity, as predicted, represented by catalyst *EX6316* ( $S_{VAM} = 96.39\%$ ). On the other hand, this leads to relatively low activity values which may derive from a high Pd deposition throughout the shell. By contrast, the mean shell thickness of *EX6318* is close to the optimum value of approximately  $200\ \mu\text{m}$ . Due to a thicker shell compared to *EX6316*, its selectivity is lower (*EX6318*,  $S_{VAM} = 95.52\%$ ). However, the higher Pd amount (*cf.* tab. 4.6) concentrated in a thinner shell is responsible for the low activity of this catalyst. The significant improvement in *STY* obtained for all other GPR catalysts (fig. 4.7) confirms the disadvantage of an only  $135\ \mu\text{m}$  thick shell.

In addition, the results show that GPR leads to thinner shell formation differing

Table 4.11: Shell thicknesses for VAM catalysts synthesised via GPR and diverse bases.

<i>EX No.</i>	<i>6318</i>	<i>6316</i>
Precipitation agent	NaOH	Na <sub>2</sub> SiO <sub>3</sub>
Shell thickness [ $\mu\text{m}$ ]	191.9	135.0

by about 40  $\mu\text{m}$  for both bases. However, similar shell thicknesses would be expected for both reduction media since this parameter is meant to be configured during the precipitation. As an assumption, thicker shells for the LPR were possibly caused by the flow pressure of NaH<sub>2</sub>PO<sub>2</sub> during reduction which can take free chlorides into the center of spheres leading to shell growth.

The laboratory experimental trend showing VAM catalysts reduced via LPR revealing thicker shells than GPR analogues was also observable for specimens resulting from production scales of plant certification trials *B* and *D* (4.12). Better performance data for the temperature varied catalysts of *D* can therefore be partly attributed to their thickness which is about 80  $\mu\text{m}$  lower than for the reference *B*.

Table 4.12: Shell thicknesses for VAM catalysts obtained by plant certification trials, varying in reduction medium.

<i>EX No.</i>	<i>B</i>	<i>D</i>
Reduction	LPR	GPR
Shell thickness [ $\mu\text{m}$ ]	330.0	246.0

### 4.2.3 CO chemisorption

The extent of Pd dispersion was analysed at SCAG for catalysts synthesised with different base mixtures and by variation in reduction media. For this method samples were reduced at 200 °C for one hour. Then specimens were exposed to a carbon monoxide excess pulse at RT. After elimination of non-chemisorbed CO, utilising a H<sub>2</sub> current, heating at 400 °C resulted in methanation. The dispersion of palladium ( $D_{Pd}$ ) was finally obtained by the molar ratio of chemisorbed CO to Pd which gives the

Pd concentration of the sample, assuming that 1 mol CO adsorbs on 1 mol Pd. Furthermore, mean particle sizes  $d$  were calculated from  $D_{Pd}$  using the following equation ( $v_m$  = volume occupied by an atom  $m$  in the bulk of metal,  $a_m$  = surface area occupied by an atom  $m$  on a polycrystalline surface) [73]. The obtained results for  $D_{Pd}$  and  $d$  are summarised in table 4.12.

$$d = 6 \cdot \frac{v_m}{a_m} \cdot \frac{1}{D_{Pd}} \quad (4.1)$$

Table 4.13: Measured Pd dispersion  $D_{Pd}$  and resulting mean particle size  $d$  for different base mixtures and variation in reduction medium.

<i>EX No.</i>	<i>6152</i>	<i>6312</i>	<i>6313</i>	<i>6314</i>	<i>6315</i>	<i>6318</i>	<i>6316</i>
NaOH/Na <sub>2</sub> SiO <sub>3</sub>	100/0	70/30	50/50	30/70	0/100	100/0	0/100
Reduction	LPR	LPR	LPR	LPR	LPR	GPR	GPR
$D_{Pd}$ [%]	8	7	6	5	12	27	25
$d$ [nm]	13.9	15.9	18.5	22.2	9.3	4.1	4.4

A trend can be observed which suggests that the Pd dispersion decreases with use of increasing amount of Na<sub>2</sub>SiO<sub>3</sub> compared to NaOH. However, catalyst *EX6315* is an exception to this general result. Furthermore, it is quite obvious that both specimens reduced via forming gas (*EX6318* and *EX6316*) achieved three to four times higher Pd dispersion than their liquid phase reduced analogues. This result indicates that GPR leads to smaller particles than LPR which can be confirmed by the calculated mean particle sizes. However, it was determined that water stored in the KA carrier was interfering with the measurements. With regard to this observation, changes in Pd dispersion due to variations in the reduction medium is scientifically more reliable than the marginal influence of bases. Pulse chemisorption would be an appropriate method of choice for optimisation to determine Pd dispersion. However, this instrument was not available at the time of this study. Therefore, subsequent characterisation techniques will reveal if this result can be confirmed.

#### 4.2.4 BET measurements

Specific surface areas of the benchmark  $B$  were determined at 77 K using the standard BET method [74] at SCAG. Nitrogen physisorption isotherms were obtained with a Micromeritics Tristar instrument after baking out the samples at 150 °C in vacuum. Table 4.14 displays BET surface areas before and after impregnation with potassium acetate. In addition, the analysed value for the spent catalyst after test screening procedure is given below.

Table 4.14: BET surface areas for the carrier of benchmark  $B$  synthesised by LPR, differing between the fresh and spent sample; all BET values are represented in  $[\text{m}^2\text{g}^{-1}]$ .

<i>EX No.</i>	<i>B</i>
Without KOAc	159
Fresh sample	66
Spent sample	89

As expected this catalyst reveals a decrease in surface area after potassium acetate impregnation. Pore filling with this solution seems to affect significantly the sample studied. In addition, a meaningful alteration in BET surface area is also occurring between the fresh and spent catalyst. The carrier surface area increase of  $23\text{m}^2\text{g}^{-1}$  after testing can be attributed to the volatilisation of KOAc.

#### 4.2.5 X-ray powder diffraction (XRD)

X-ray powder diffraction (XRD) represents a common characterisation technique to analyse phases present in heterogeneous catalysts. The diffraction pattern formed by reflection at distinctive scattering angles identifies a particular crystalline phase. In addition, the measured intensities correspond to the amount of the crystalline phase in the specimen. Identification of phases is possible by comparison of the measured XRD profile with a database of standard profiles.

XRD data were obtained at SCAG using a Bruker D4 Endeavor X-ray diffractometer with Cu  $K\alpha$  radiation ( $\lambda = 154.06\text{ pm}$ ). All samples presented subsequently were

analysed at room temperature for a scanning angle range of 5 to 90° in 0.3° steps with a 0.5 s hold time per step. For optimisation of precious metal intensities compared to the carrier SiO<sub>2</sub>, shell surfaces of about 100 catalyst spheres were scraped off for preparation of powder specimens. Due to the low analytical amounts a Bruker silicon monocrystal (fig. 4.10) was used to hold the specimen during the measurements. Without any holder X-rays would pass through the thin catalyst sample and generate unfavourable background signals. Furthermore, results can be improved since the silicon monocrystal does not generate any reflections itself. The crystalline phases were identified by reference to the International Centre for Diffraction Data (ICDD).

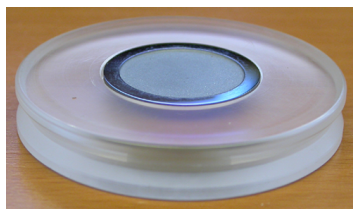


Figure 4.10: Silicon monocrystal purchased by Bruker for holding the sample without self-generated reflections during analysis.

XRD patterns of catalysts *B* and *EX7273* were investigated, in order to reveal differences caused by variation in the reduction phase. Figure 4.11 displays both XRD profiles for the fresh (*f*) catalysts *B<sub>f</sub>* and *EX7273<sub>f</sub>*. As shown in this figure, both catalyst samples have similar patterns with small variations in reflection intensities. For both XRD profiles an amorphous signal centered at about  $2\theta = 23^\circ$  and a sharp reflection of relatively high intensity at approximately  $2\theta = 27^\circ$  can be seen. Furthermore, several sharp reflections of lower intensity at  $2\theta = 21, 50, 60$  and  $68^\circ$  are visible. Broad reflection components in the range of  $2\theta = 38-41^\circ$  and  $2\theta = 45-46^\circ$  can also be observed.

While the broad feature at  $2\theta = 17-31^\circ$  is characteristic for amorphous silica [75, 76], all of the sharp reflections obtained, including the component of high intensity at  $2\theta = 27^\circ$ , correspond to a crystalline form of quartz in the support material, as illustrated in the following figures 4.12 and 4.13.

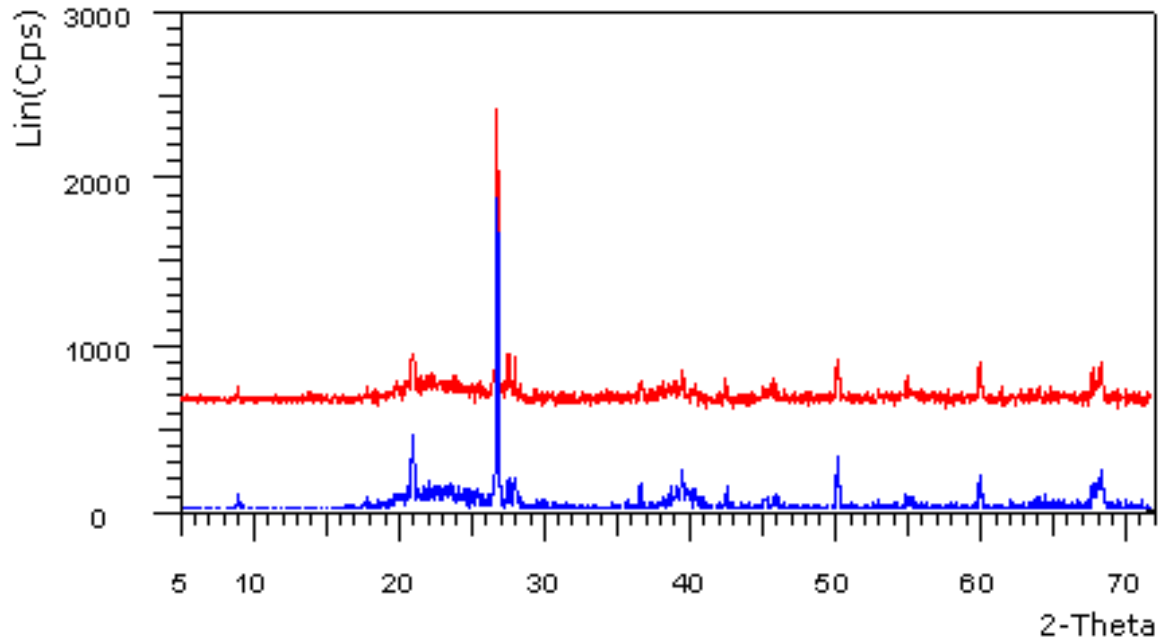


Figure 4.11: XRD data obtained from fresh catalysts  $B_f$  (blue) and  $EX7273_f$  (red) for  $2\theta$  range of 5-70°.

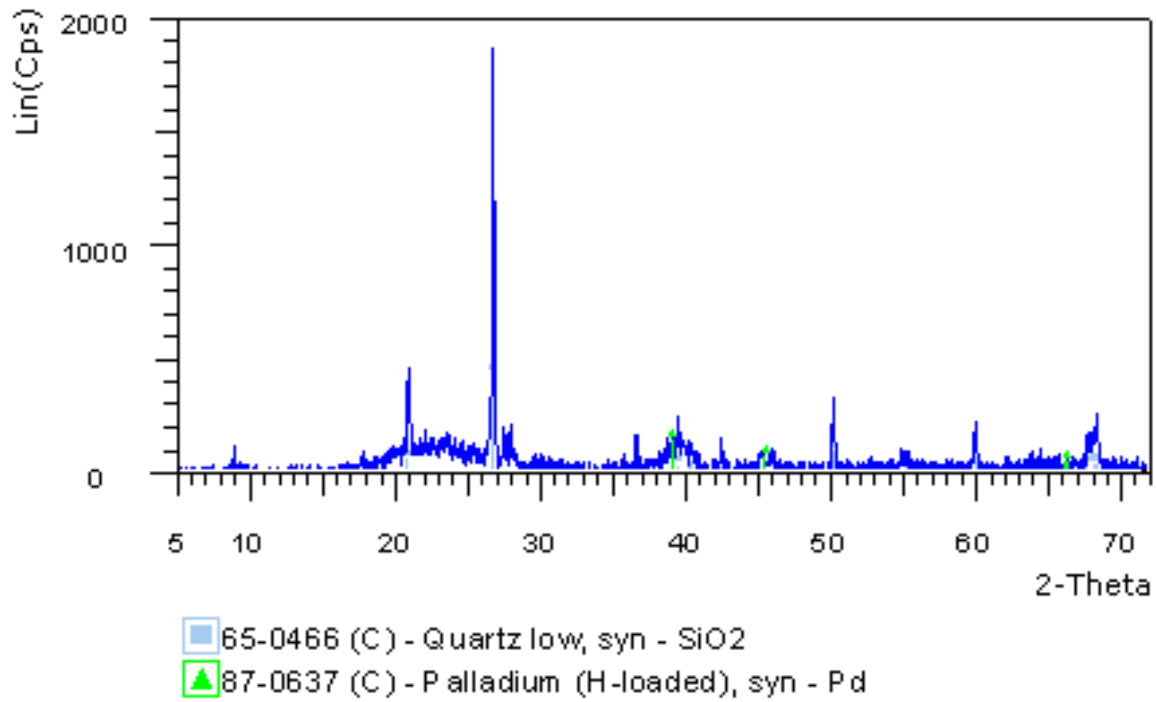


Figure 4.12: Identification of reflections for XRD pattern of fresh catalyst  $B_f$ .

Due to the high intensity of the main quartz reflection compared to other reflections throughout the XRD profile, a significant quantity of this modification is supposed to

exist in the carrier. Further reflections at  $2\theta = 38-41^\circ$  and  $2\theta = 45-46^\circ$  were identified as the Pd metal phase with interstitial hydrogen atoms. The presence of these hydrogen atoms is assumed to derive, in both cases, from the reduction stage of VAM catalyst synthesis. According to the pattern files available from the ICDD data base, the observed Pd reflections can be attributed to Pd(111) ( $2\theta = 39.060^\circ$ ) and Pd(200) ( $2\theta = 45.414^\circ$ ). Pd particle sizes in both catalysts are assumed to be rather small (several nm) due to the broad character of the reflection, correlated with its low intensity. However, it is assumed that most of the observed reflections derive from the catalyst support, KA 160 (lot 7073). Figure 4.14 reveals the XRD pattern of this carrier which was subsequently used. The pattern has been subtracted from the fresh VAM catalyst profiles, in order to disclose the phases not affected by the support.

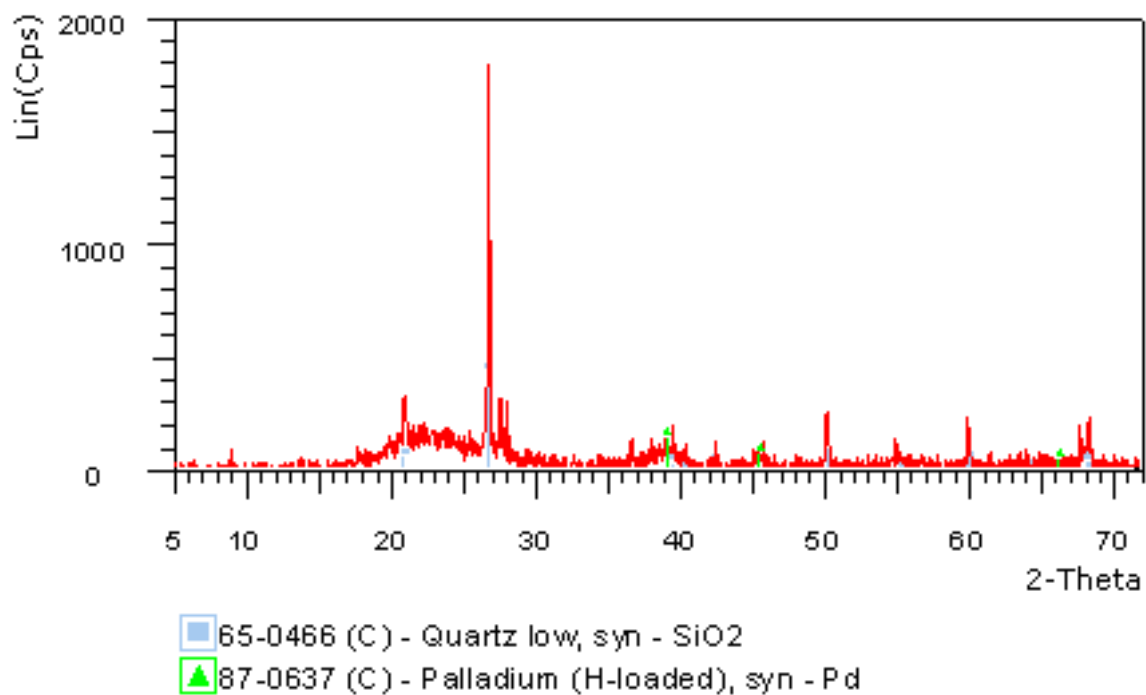


Figure 4.13: Identification of reflections for XRD pattern of fresh catalyst  $EX7273_f$ .

The remaining reflections are displayed for both specimens  $B_f$  and  $EX7273_f$  in figures 4.15 and 4.16. As expected the broad background signal representing the amorphous part of KA 160 is not visible. However, some reflections of the quartz phase are still present, although in lower intensities, which can be assigned to the calculation method. It can be now confirmed that both residual broad peaks derive from  $Pd^0$ . In

addition, this view verifies that the expected reflections corresponding to other catalyst components, such as Au or PdO, could not be observed.

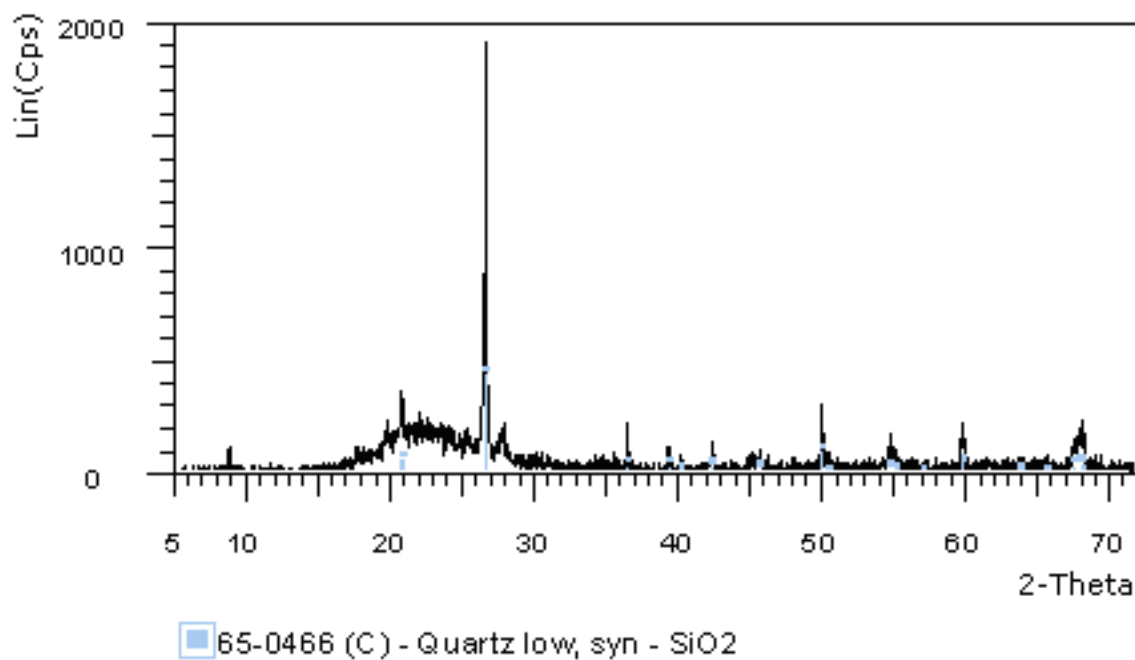


Figure 4.14: XRD pattern resulting from VAM catalyst carrier KA 160 lot 7073.

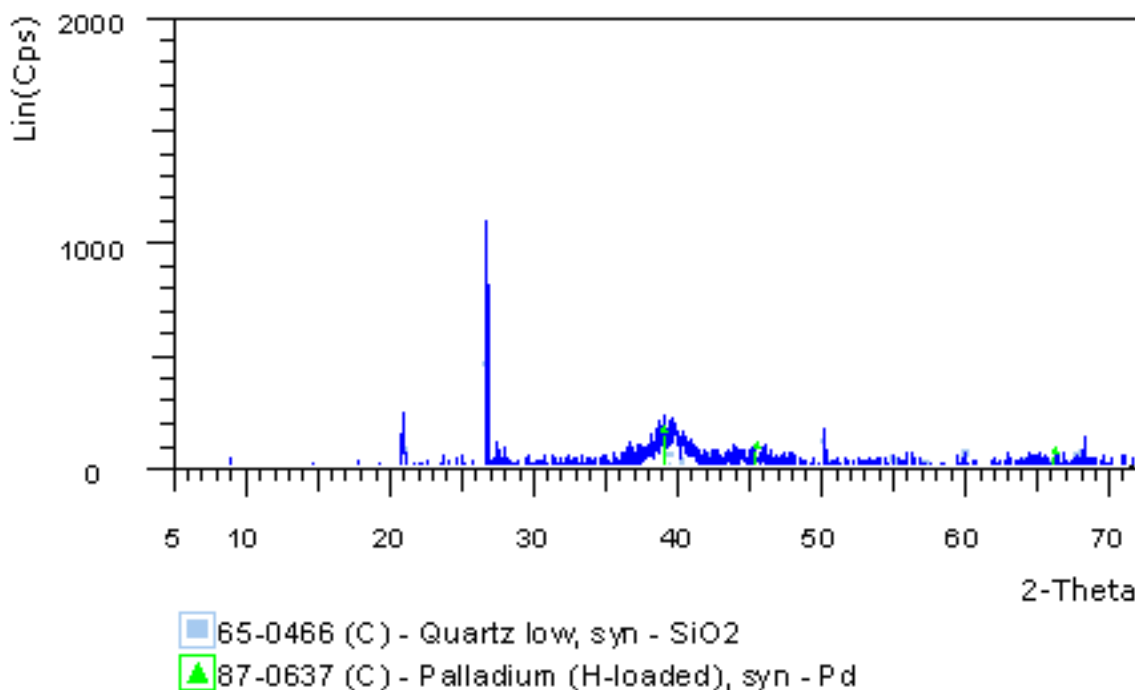


Figure 4.15: Identification of reflections for XRD pattern of catalyst  $B_f$  after subtraction of carrier profile.

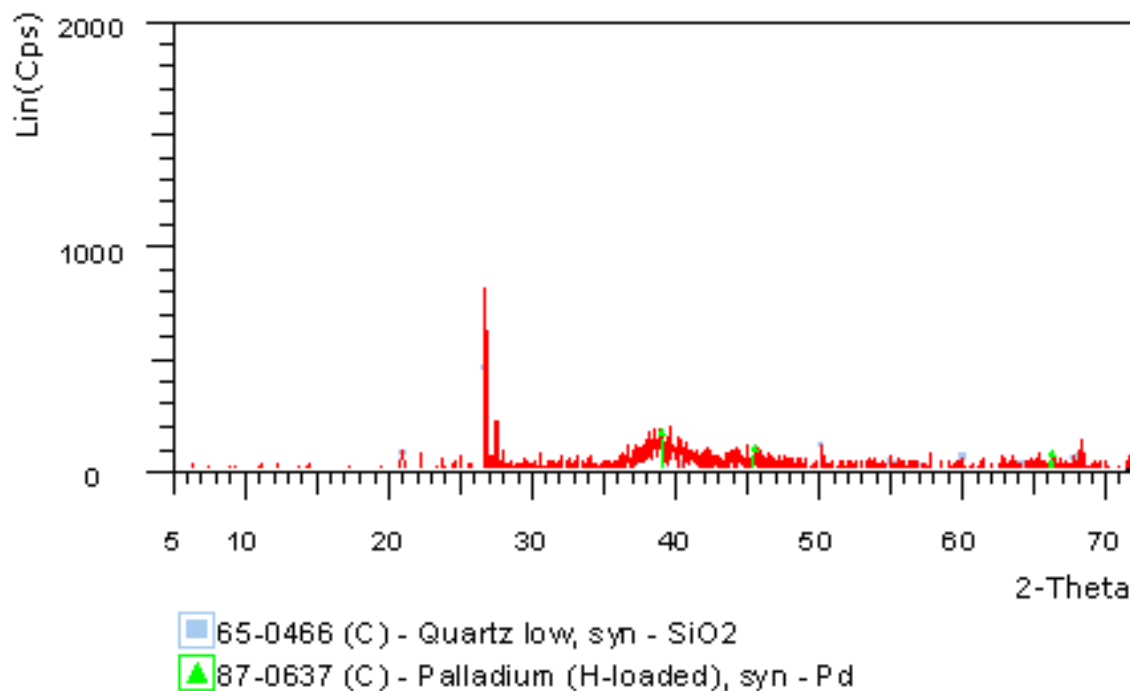
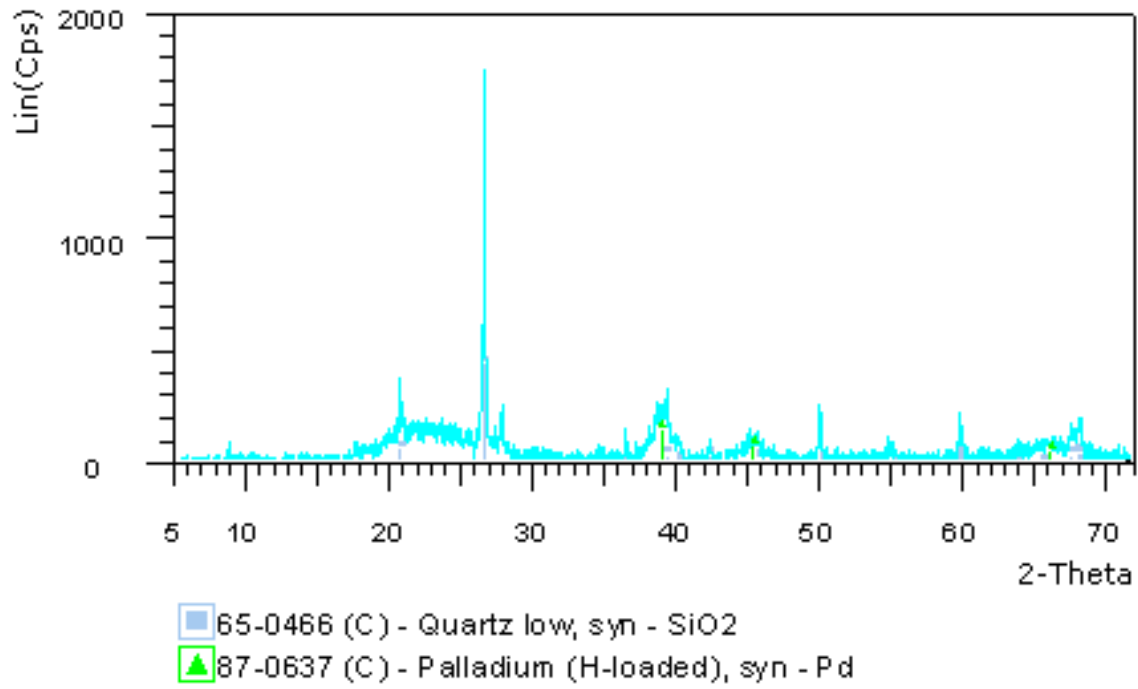
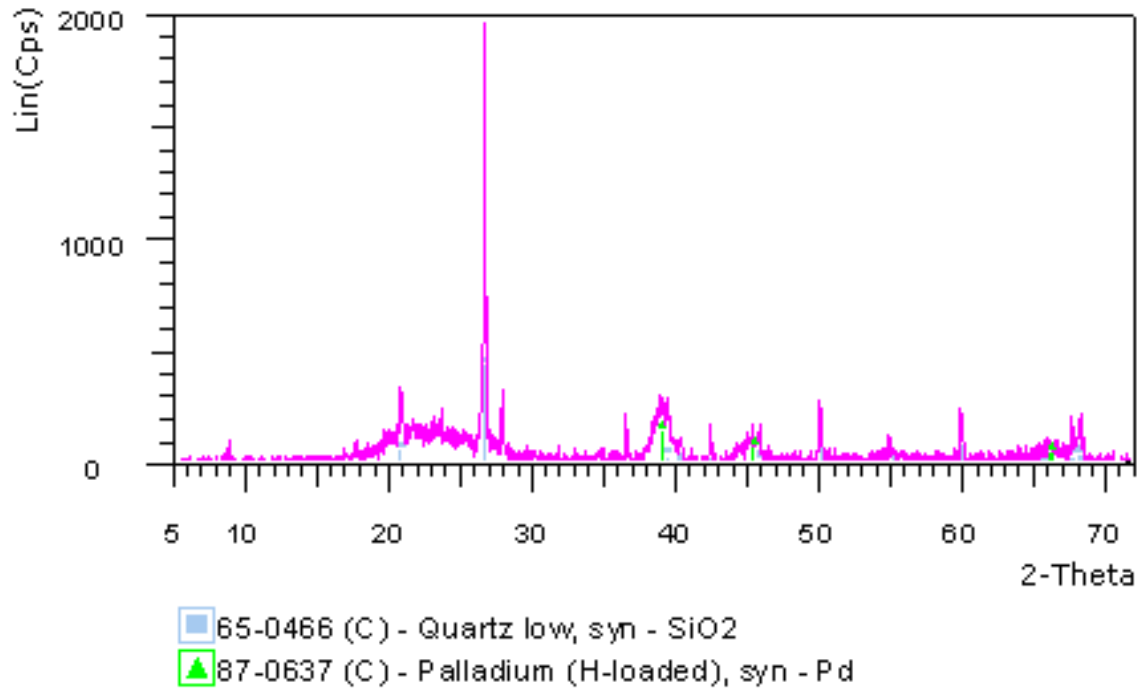


Figure 4.16: Identification of reflections for XRD pattern of catalyst  $EX7273_f$  after subtraction of carrier profile.

In addition to characterisation of fresh VAM catalyst samples, XRD measurements were carried out for the same catalyst species after being tested via the test screening procedure, as outlined in section 3.5. XRD results from these two spent catalysts, referred to as  $B_s$  and  $EX7273_s$ , are summarised in the following figures to determine the presence of consistent reflection phases. As figures 4.17 and 4.18 illustrate, both spent samples show reflections at the same scattering angles as their corresponding fresh analogues. This implicates that no phase transformation occurred during testing of the catalysts.

Figure 4.19 displays all four XRD profiles of fresh and spent catalysts in order to give a final comparison. Regarding the fresh and spent samples of each catalyst species, it can be observed that the shape of the Pd reflections changes marginally after the test procedure. Compared to the fresh specimens, showing broad Pd reflections, the analogous features for both spent catalysts are rather sharp. This would suggest that the samples of spent catalysts contain larger Pd particles than those in the fresh species.

Since the obtained Pd reflections are in all cases very broad and relatively low in

Figure 4.17: Identification of reflections for XRD pattern of spent catalyst  $B_s$ .Figure 4.18: Identification of reflections for XRD pattern of spent catalyst  $EX7273_s$ .

intensity, using the full width at half maximum (FWHM)  $\Delta$  of these reflections to calculate the mean particle diameter  $d$  via Scherrer equation may be subject to a

meaningful error. In the following equation  $k$  represents the Scherrer constant,  $\lambda$  the X-ray wavelength and  $\theta$  the Bragg angle of the peak maximum:

$$d = k\lambda/\Delta\cos\theta \quad (4.2)$$

Based, for example, in the case of the fresh catalyst  $B_f$ , taking  $\Delta = 1.85$  at  $39.52^\circ$  as the reflection maximum, an average Pd particle diameter of 4.6 nm was calculated. However, taking the conditions described above into consideration, the calculated results can only indicate a tendency to values of particle diameter. It can be estimated that the mean particle sizes determined for  $B$  catalysts are bigger than for  $EX7273$ . While values of fresh catalysts are around 5 nm for the liquid phase reduced sample  $B_f$ , Pd particle size for  $EX7273_f$  reduced in gas phase is approximately 3 nm. The trend of particles being smaller for  $EX7273$  than for  $B$  was confirmed for the spent samples. Furthermore, calculations revealed that mean particle sizes for each catalyst species increased by 1 nm after testing.

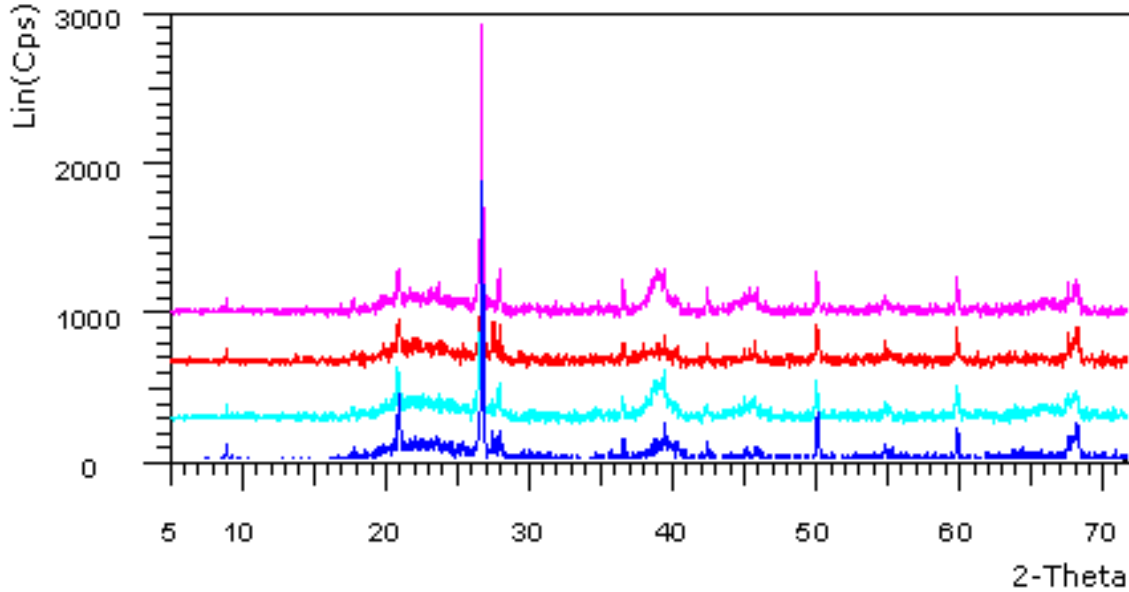


Figure 4.19: XRD patterns of fresh and spent catalysts for species  $B$  and  $EX7273$ :  $EX7273_s$  (magenta),  $EX7273_f$  (red),  $B_s$  (turquoise) and  $B_f$  (blue).

Finally, it can be summarised that, apart from reflections caused by the carrier support, only Pd was detected in its metallic state. Expected reflections indicating phases like PdO and Au could not be measured. Although Pd was observed via XRD,

the amount of this metal and especially of Au is generally too low to obtain an optimum pattern for better differentiation of the various catalysts. Therefore it has to be stated that XRD is a helpful technique to reveal components high in crystallinity and amount, but it can only give rough indications about catalytic components of low concentration, represented herein by Pd and Au. This limitation makes it difficult to distinguish features of VAM catalysts via the XRD characterisation technique.

#### 4.2.6 Energy dispersive X-ray spectroscopy (EDX)

Energy dispersive X-ray spectroscopy (EDX) is a commonly used characterisation technique for qualitative and quantitative analysis of elements present in the studied samples. Such investigations were carried out at Technische Universität Darmstadt (TUD) on a FEI CM12 microscope operating at 120 kV by using a LaB<sub>6</sub> cathode and equipped with an EDAX Genesis 2000 (Ametek GmbH) EDX system. The concentration ratio of Pd and Au in VAM catalysts had been determined previously by wet chemical analysis (*cf.* sec. 4.2.1). The intention of EDX characterisation was to reveal the local composition and distribution of Pd and Au. Are both noble metal atoms present separately in the catalyst, forming Pd and Au particles, or do the two species mix to form clusters? Another structural configuration could result in substitution of atoms, forming alloys. And if mixed crystals arise which composition would be preferred or would different ratios be found?

For EDX analysis an electron beam was directed at different sample positions on catalyst *B*. The spectra of the emitted X-rays were detected, as illustrated representatively in figure 4.20, indicating the elements present in the sample.

As the EDX data show, considerable variations in Pd and Au composition were revealed. Whereas the first location of sample *B* contains both precious metals in significant intensities, compared to the Si and O originating from the carrier, rather low amounts of Pd and Au could be observed for a neighbouring area enriched in silica. In addition, the third spectrum indicates lower Pd/Au ratios than the first. Comparison of the signal intensity ratios for Pd L and Au M signal results in values of about 2.5 for the third location and 4 for the first.

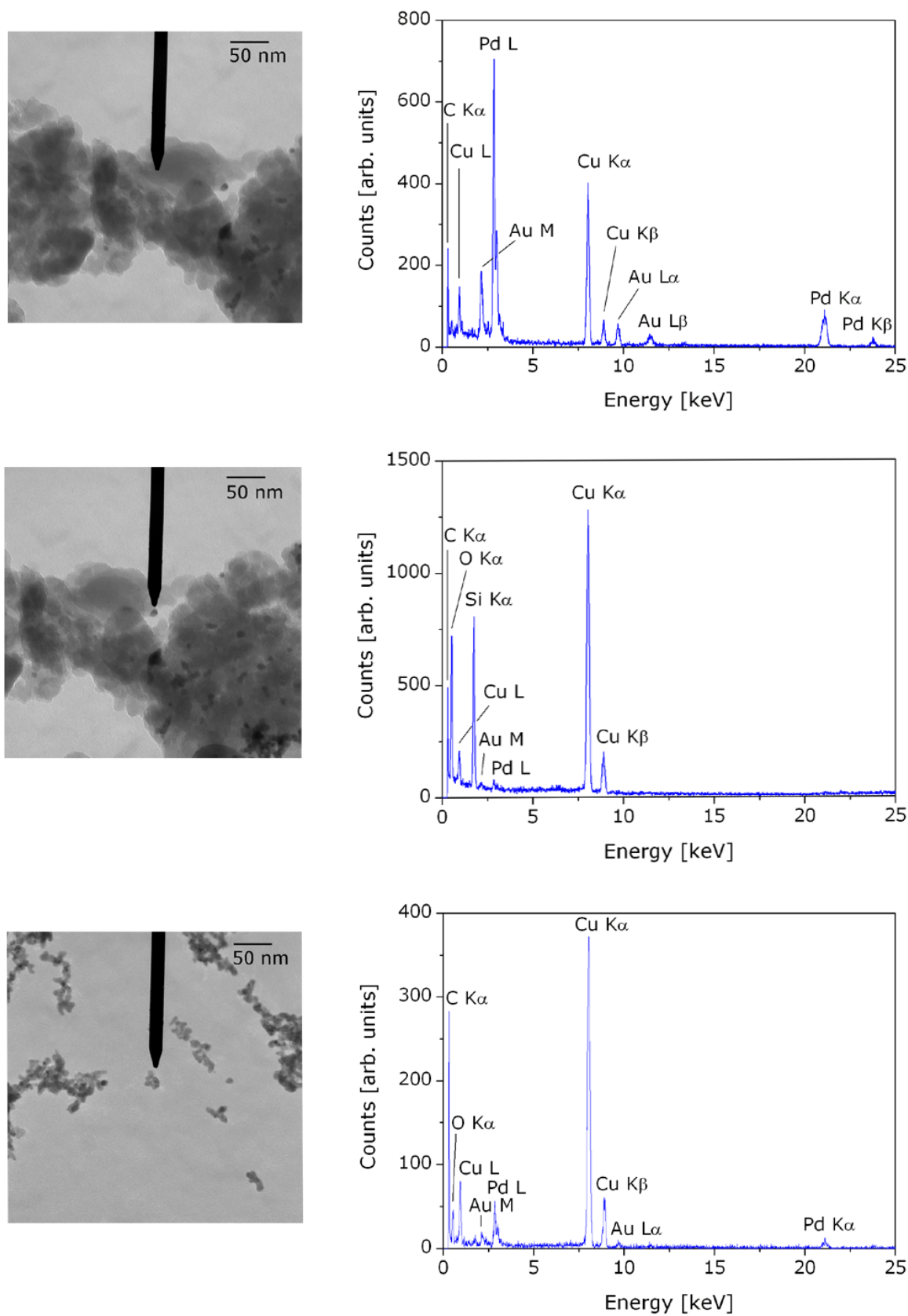


Figure 4.20: EDX analysis for different locations on catalyst *B* (left) and their corresponding spectra (right).

Generally speaking the analyses showed that the amount of carrier compared to both noble metals is too high to obtain high intensity peaks suited for analysis of the catalyst species. Similar difficulties were encountered in the XRD studies presented previously.

As a further result it was revealed that isolated particles are not present in this studied sample. The metal particles in *B* seem to have a large tendency to agglomerate. In the following section a study via transmission electron microscopy (TEM) of catalyst *B* will give attention to this observation, providing statistics about the size and local distribution of the particles.

Additionally, EDX analysis indicated that particles in this catalytic system were too small for a separate evaluation with the equipment used. Since the maximum resolution is 20 nm, particles revealing smaller sizes could not be analysed separately. Further investigations using high resolution electron microscopy (HREM) would be a promising alternative to improve EDX results for catalyst particles in the range of several nanometers.

#### 4.2.7 Scanning electron microscopy (SEM)-EDX mapping

As shown by further experiments on VAM catalysts synthesised with an advanced coating technology (*cf.* chp. 6), the performance correlates with the homogeneity of metal distribution throughout the shell. In contrast to coating, it is difficult to influence the distribution by use of the incipient wetness method. The effect of different process parameters in the IW approach on the shell structure was analysed at SCAG by applying scanning electron microscopy (SEM) in combination with EDX mapping, using a Leo 1530 (Zeiss) microscope coupled with an XFlash 4010 detector from Bruker. For every catalyst, two different hemispheres were analysed in order to optimise statistics. The elemental distribution on the cross section of the hemispheres will be represented by different colours.

To receive a first impression about the Pd and Au distribution in VAM catalysts based on different KA-Zr carriers, a sample with low Zr concentration (*EX7804*) was compared to one of the higher Zr containing catalysts (*EX8082*). Figure 4.21 displays both an overall distribution of the elements in one image as well as separate views

showing each analysed element for *EX7804*.

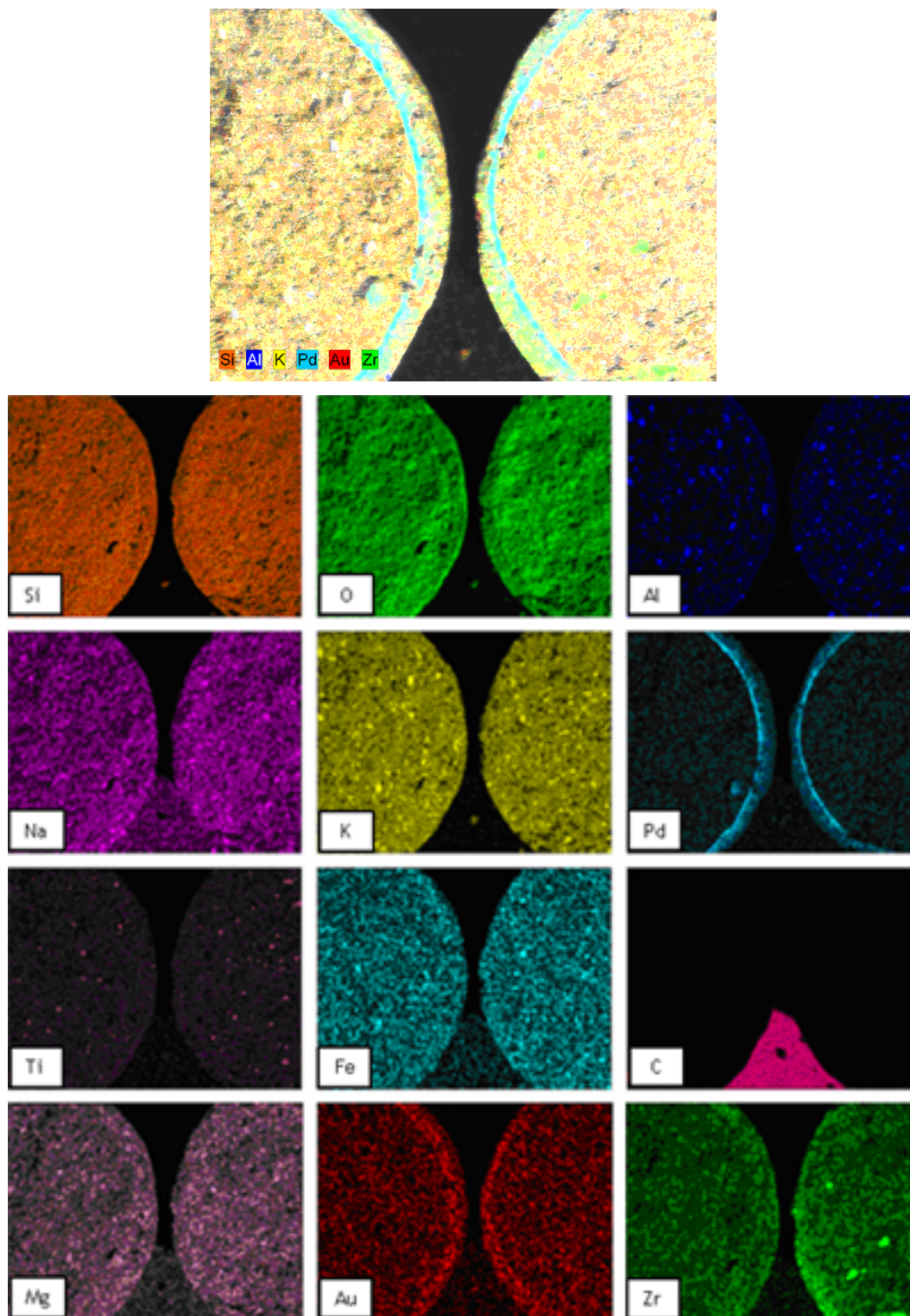


Figure 4.21: SEM-EDX mapping indicating the distribution of elements throughout the catalyst shell for *EX7804*.

Since no differences in the elemental distribution of Si, O, Al, Na, Ti, Fe, C and Mg were observable for all presented catalysts, attention will be given in the following to the dispersion of K, Pd and Au. Homogeneous distributions are favoured for both metals, Au and Pd, inside the shell. On the contrary, K should preferably be evenly spread throughout the complete sphere, since it diffuses to the surface to fill any local absences. Comparing these distributions for both Zr-based catalysts (fig. 4.22), it can be determined that the Au and K impregnation is preferable in the low Zr sample *EX7804*. In case of catalyst *EX8082* K is mostly present near the shell region and not in the complete cross-section as for *EX7804*. It is assumed that for the Zr-enriched catalyst the pores were filled with Zr or Au, both inhibiting diffusion of potassium towards the inside of the particle. The distribution of Pd is for both catalysts similar, indicating accumulation along the boundary area between shell and interior of the sphere. Finally, it should be mentioned that the Au results for this pair of samples have to be interpreted carefully, since X-ray energies of this element ( $M\alpha$ ,  $M\beta$ ) are overlapping with the energies for Zr ( $L\alpha$ ,  $L\beta$ ).

Un the next comparison both extremes of the base mixture series reduced in liquid phase will be regarded: *EX6152* (NaOH) and *EX6315* ( $\text{Na}_2\text{SiO}_3$ ). As the analysis of shell thickness revealed, precipitation with NaOH resulted in approximately 20 % thicker shells than in case of  $\text{Na}_2\text{SiO}_3$  application. This significant observation could be confirmed by SEM-EDX mapping (fig. 4.23). Furthermore, this characterisation method showed that the Pd and Au distribution is more homogeneous throughout the shell of *EX6315* than for *EX6152*. This can be explained by the following effect of chromatography: In general, the metal gradient increases from outwards to the center of the sphere. The thicker the catalyst shell, the broader the gradient in metal concentration. Since the concentration of Pd used in VAM catalyst synthesis is significantly higher than for Au, this effect is visible only marginally for the latter metal. Thus, the differences in synthesis parameters, correlating with the shell thickness, are assumed to influence the distribution of elements inside this region. In case of catalyst *EX6152*, Pd is therefore more concentrated at the boundary area between the shell and the catalyst interior. However, the dispersion of K is similar for both catalysts (fig. 4.23).

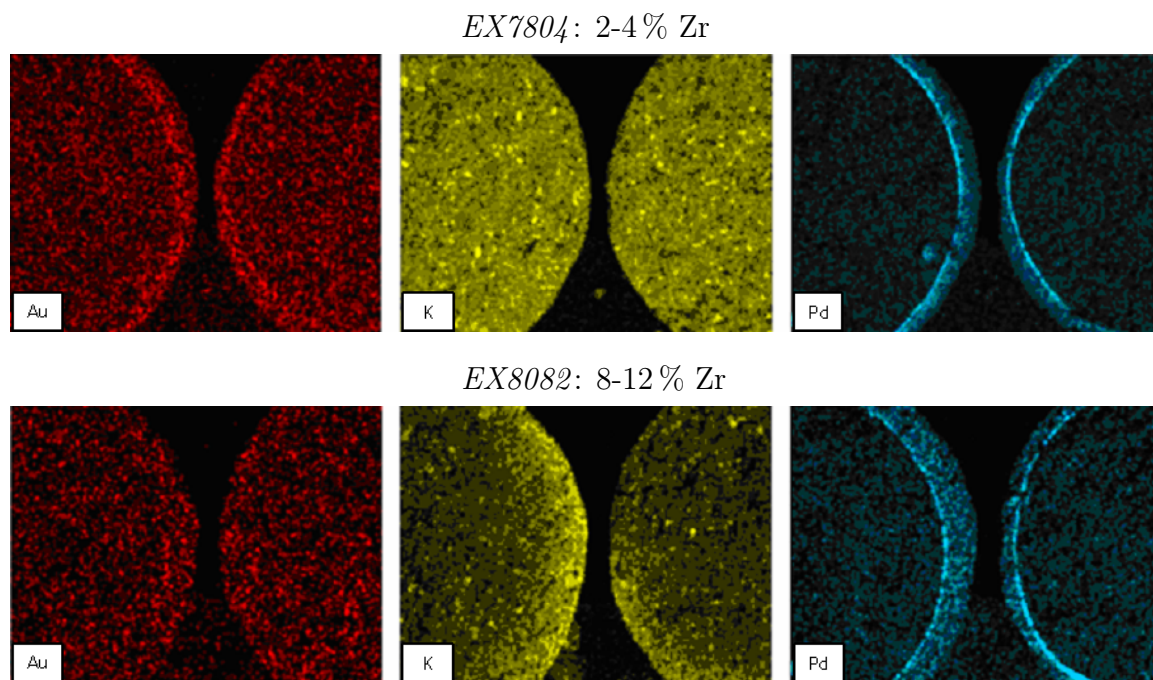


Figure 4.22: Influence of Zr concentration in the carrier on distributions of Pd, K and Au.

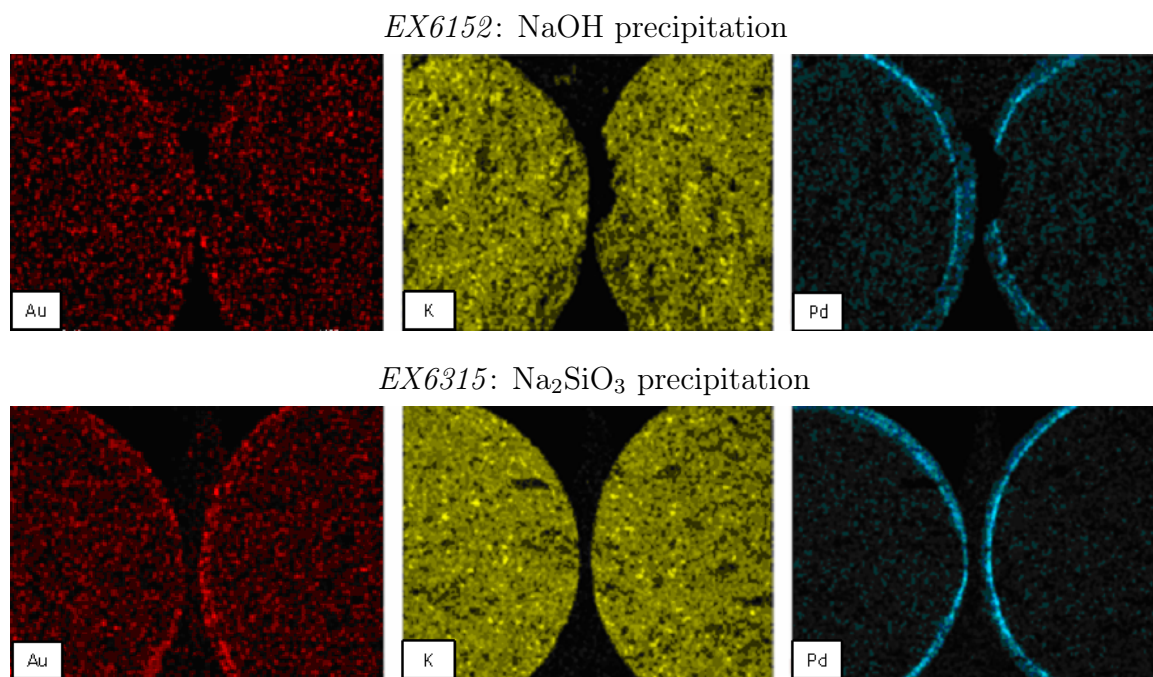


Figure 4.23: Influence of the precipitating agent on Pd, K and Au dispersion.

Finally, elemental mappings were obtained for catalysts *B* (LPR), *EX7273* (GPR at 150 °C) and *EX7275* (GPR at 250 °C) (fig. 4.24). Although they differ in reduction medium and temperature, no significant deviations were found concerning the

distribution of elements. Consequently, this comparison reveals that other parameters than metal distribution throughout the sphere are the determining factors for the pronounced difference in performance between LPR and GPR.

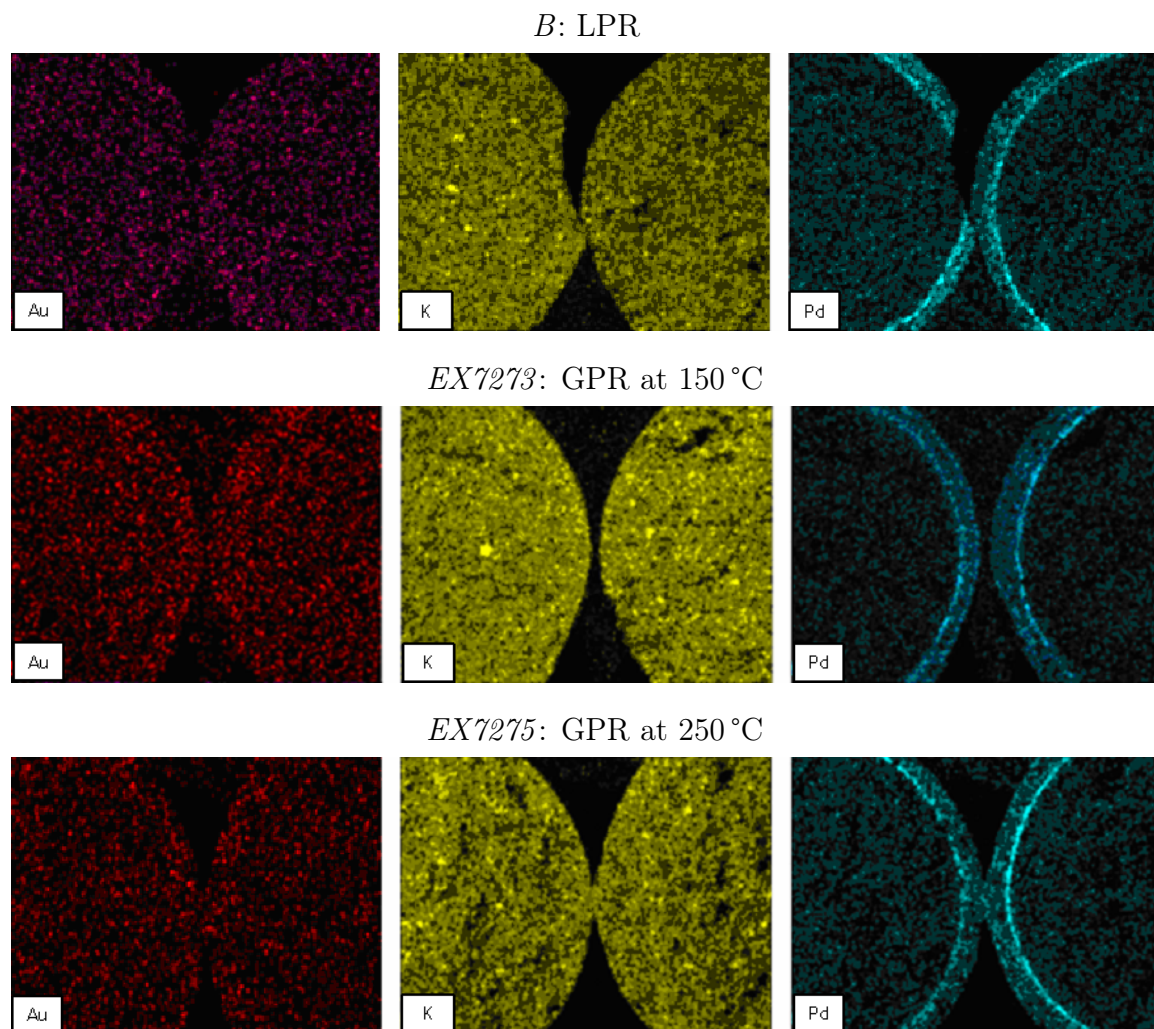


Figure 4.24: Distribution of Pd, K and Au for catalysts reduced in liquid and gas phases.

### 4.2.8 Transmission electron microscopy (TEM)

As a further characterisation method transmission electron microscopy (TEM) was carried out to analyse the morphology and size distribution of the catalyst particles. Since the major difference in activity was determined between the two reduction media (*cf.* fig. 4.7), fresh and spent samples of catalysts *B* (LPR), *EX7273* (GPR at 150 °C) and *EX7275* (GPR at 250 °C) were investigated by this technique for subsequent comparison. TEM micrographs were obtained at TUD with a Jeol JEM-3010 transmission electron microscope equipped with a LaB<sub>6</sub> cathode operating at 300 kV. Samples were prepared by addition of ethanol and subsequent dispersion in an ultrasonic bath before deposition of the catalyst powder onto copper grids (mesh 150) covered with a lacey carbon support.

Figure 4.25 displays representative examples for the distribution of metal particles in catalyst *B<sub>f</sub>*. From the micrographs it can be seen that the particles have a high tendency to form agglomerates resulting in chain-like framework structures.

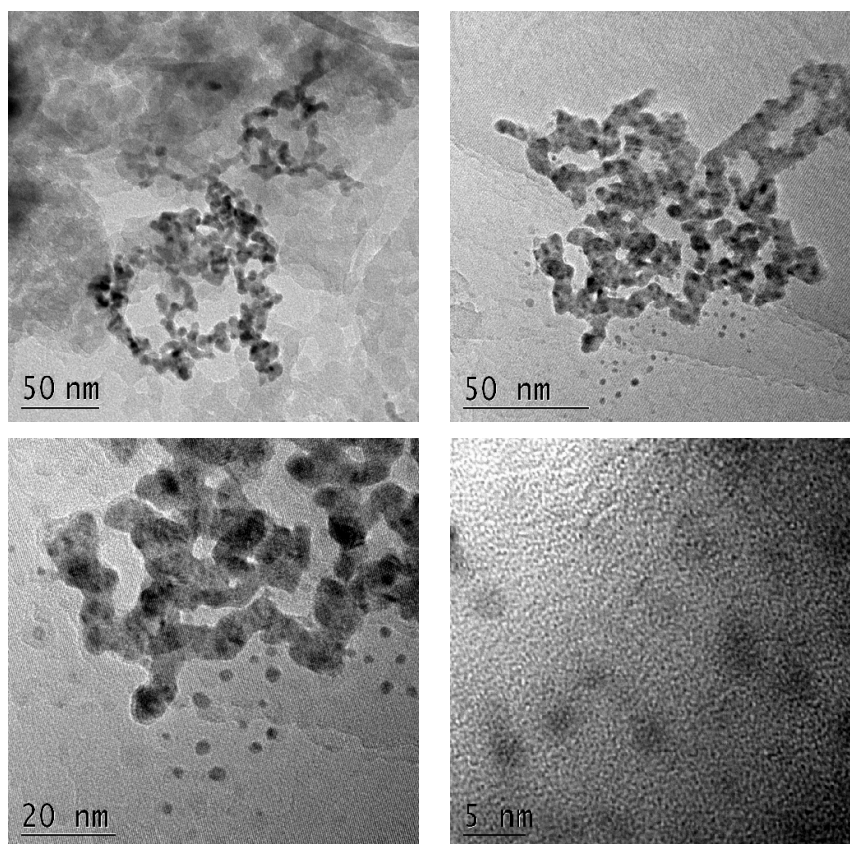


Figure 4.25: TEM images for fresh catalyst *B<sub>f</sub>* reduced in liquid phase.

Due to the high complexity of this framework, only isolated particles, as visible in the two bottom images, were taken into account to determine the trend in particle size distribution. A statistical evaluation of the particle diameter carried out by means of the software Lince 2.4.2 is depicted in the histogram below (fig. 4.26). It becomes obvious that these particles have a rather uniform size distribution averaging at  $(2.2 \pm 0.8)$  nm.

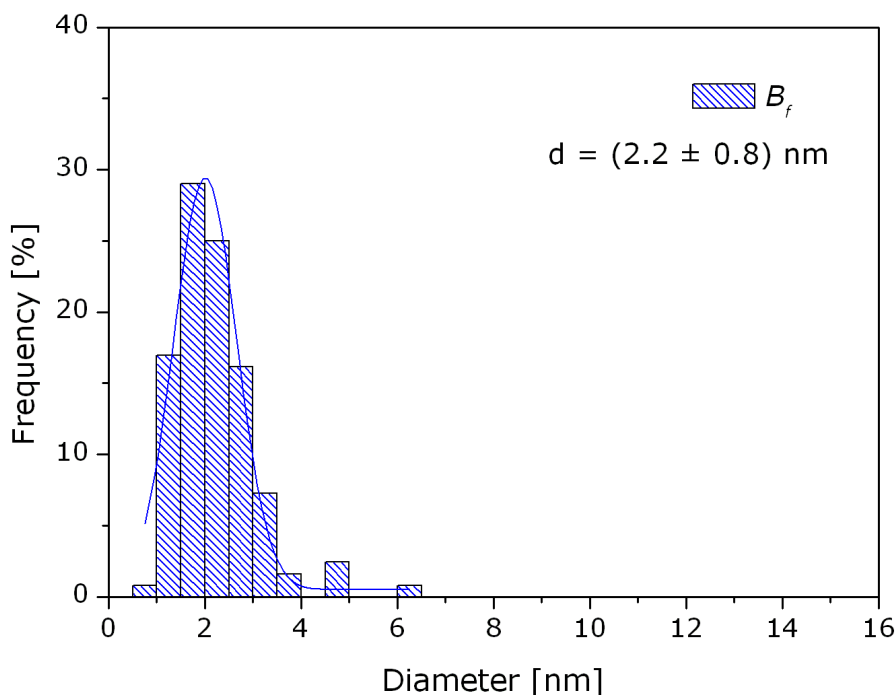


Figure 4.26: Particle size distribution of catalyst  $B_f$ .

In contrast to catalyst  $B_f$ , a different particle morphology was obtained for the fresh catalysts  $EX7273_f$  and  $EX7275_f$  reduced in gas phase at 150 and 250 °C respectively (fig. 4.27, 4.28). According to the micrographs presented at different magnification, both catalysts reveal similar local distributions of metal particles, homogeneously dispersed on the carrier. In addition, isolated inclusions of separate particles can be observed at boundary regions. However, no significant difference exists in the local distribution or the average particle size between these two catalyst specimens. This can be confirmed by the following comparison of histograms (fig. 4.29).

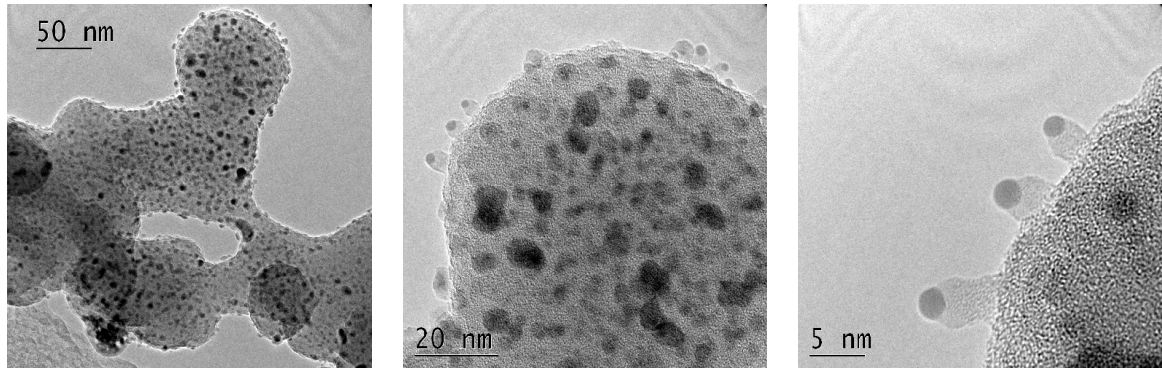


Figure 4.27: TEM images for fresh catalyst  $EX7273_f$  reduced at 150 °C in gas phase.

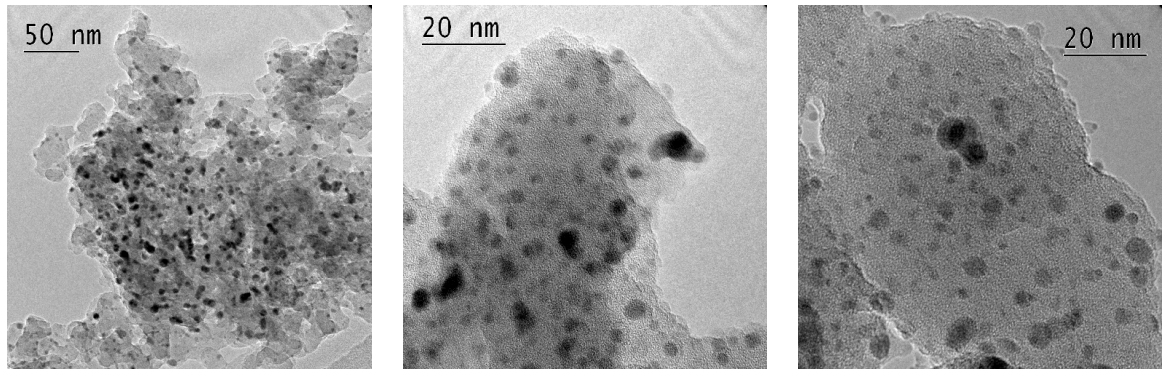


Figure 4.28: TEM images for fresh catalyst  $EX7275_f$  reduced at 250 °C in gas phase.

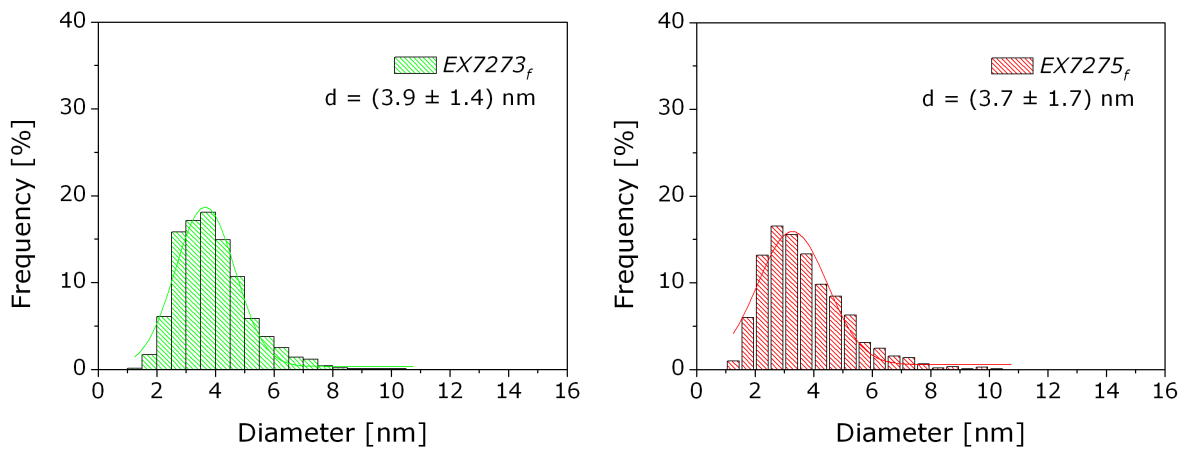


Figure 4.29: Particle size distributions of gas phase reduced catalysts  $EX7273_f$  and  $EX7275_f$ .

As can be seen from these figures, particle sizes range approximately from 1.5-10.5 nm. Average diameters are  $(3.9 \pm 1.4)$  nm for catalyst  $EX7273_f$  and  $(3.7 \pm 1.7)$  nm for  $EX7275_f$ , indicating that an 100 °C increase of temperature for GPR has only a marginal effect on particle sizes.

In addition to TEM analysis, catalysts  $B_f$  and  $EX7273_f$  were investigated by scanning transmission electron microscopy (STEM) Z-contrast imaging [77] at Siemens AG (Corporate Technology Analytics) in a FEI CM200 FEG instrument with a thermal field emitter cathode, scanning unit and high angle annular dark field (HAADF) detector. A representative image for each catalyst is shown in figure 4.30. The particles are easily discernible by this method since they consist of significantly heavier elements (higher  $Z$  = brighter contrast) than the carrier. The previously determined difference in morphology for the two catalysts ( $B_f$  = agglomeration vs.  $EX7273_f$  = small, isolated particles) can be confirmed by these images. Contrast variation within the carrier regions are due to local alteration of the sample thickness.

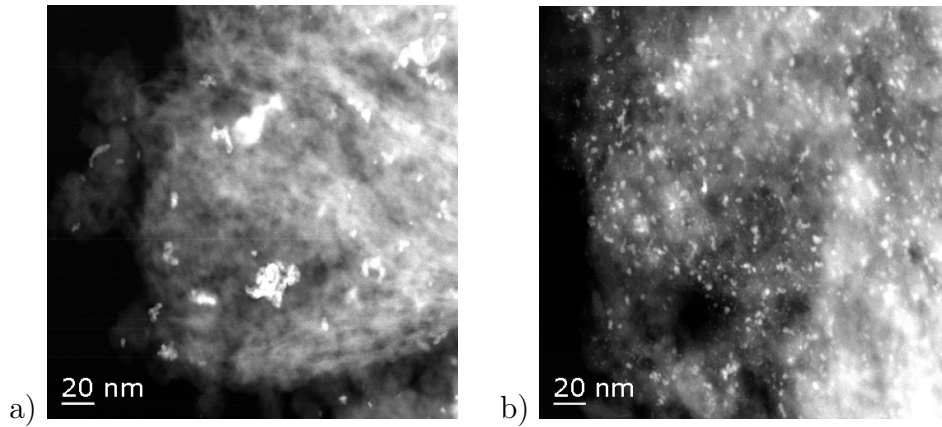


Figure 4.30: Particle morphologies for catalysts a)  $B_f$  and b)  $EX7273_f$  reduced in different media.

In order to investigate the ageing effect during testing of the VAM catalysts presented here, spent samples were also analysed with TEM. The corresponding micrographs for catalyst  $B_s$  in figure 4.31 suggest that the frameworks existing in the fresh analogue  $B_f$  agglomerate into larger particles in the samples measured after testing.

Agglomeration also occurs for a low number of small isolated particles. This is graphically shown by the histogram in figure 4.32. Particle sizes in the spent catalyst  $B_s$

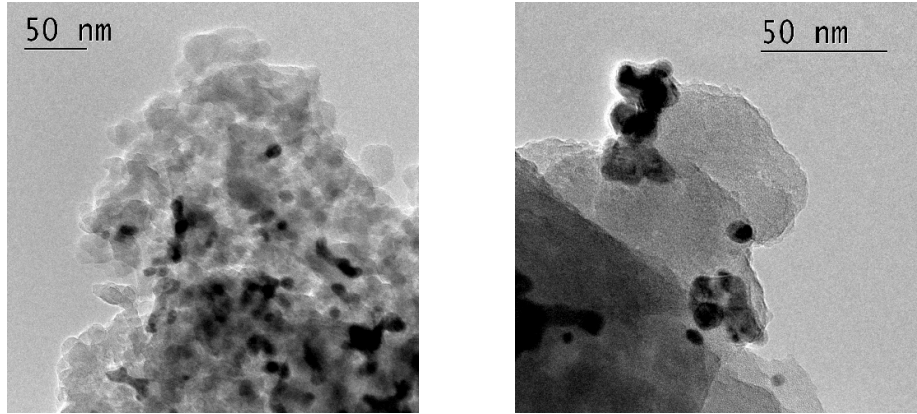


Figure 4.31: Representative micrographs for the spent catalyst  $B_s$ .

range between 3 and 12 nm. Compared to the isolated particles of  $B_f$ , this figure reveals an expanded distribution range with an average diameter of  $(6.9 \pm 1.8)$  nm. Thus, these statistics confirm the agglomeration of particles, which was already indicated by previous images. Furthermore, the results are in good agreement with BET analysis, where a meaningful increase in carrier surface area between the fresh and spent catalyst  $B$  was assumed to arise from agglomeration of particles (*cf.* sec. 4.2.4).

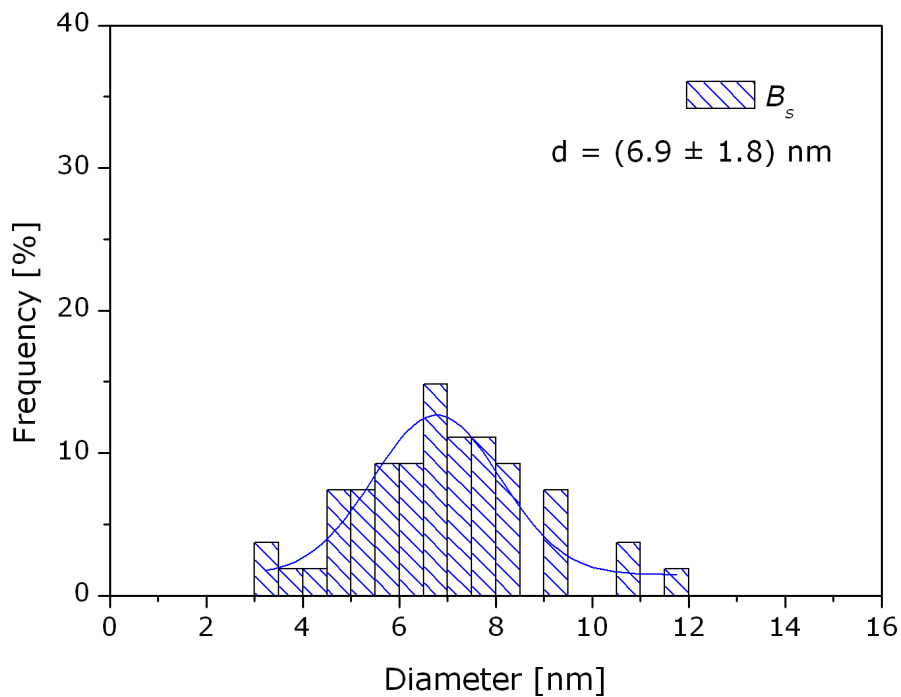


Figure 4.32: Particle size distribution of the spent catalyst  $B_s$ .

Clustering of particles is also visible for the catalysts reduced in the gas phase, as the images below in figure 4.33 illustrate using  $EX7273_s$  as an example. Measurements of particle size distribution for this specimen led to similar conclusions. The average diameter increased by about 2 nm after testing to  $(6.2 \pm 2.0)$  nm for  $EX7273_s$ . Analogous to catalyst  $B_s$ , the particle distribution after testing became broader, including a shift towards higher diameters 4.34.

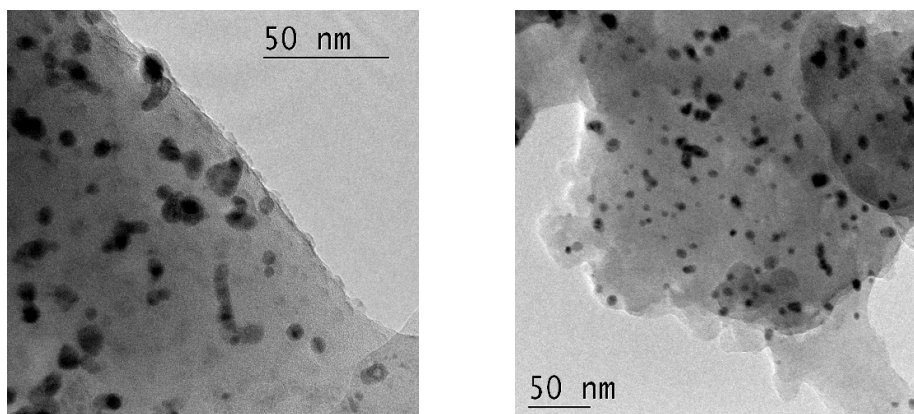


Figure 4.33: Representative micrographs for the spent catalyst  $EX7273_s$ .

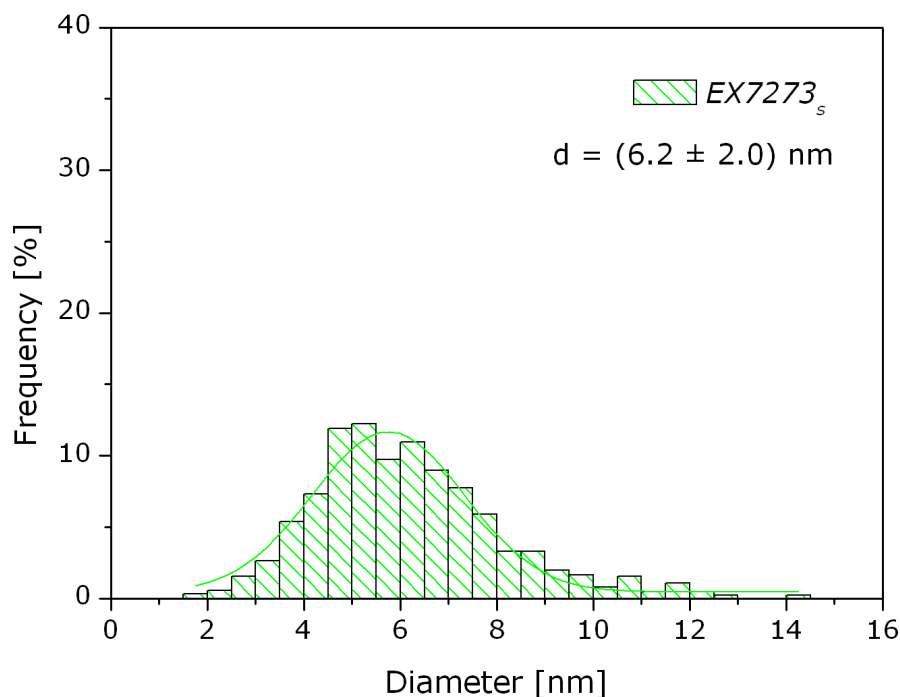


Figure 4.34: Particle size distribution of the spent catalyst  $EX7273_s$ .

Finally, it can be summarised that GPR results in smaller isolated particles than

LPR, where agglomeration is dominant. This considerable difference in particle size confirms the previously presented values based on Pd dispersion measurements (*cf.* sec. 4.2.3). The mean diameter of 4.1 nm calculated for catalyst *EX6318* (GPR<sub>200°C</sub>, NaOH) (tab. 4.13) is in very good agreement with the presented results based on TEM characterisation for *EX7273<sub>f</sub>* (GPR<sub>150°C</sub>) and *EX7275<sub>f</sub>* (GPR<sub>250°C</sub>) (fig. 4.29). Assuming a bimetallic system, Pd atoms are therefore supposed to dominate the particle surface. If the contrary was the case, the Pd dispersion would be significantly lower since CO does not chemisorb to Au. In addition, the effect of agglomeration observed with TEM analysis for catalyst *B<sub>f</sub>* (LPR, NaOH), verifies the bigger mean particle size of catalyst *EX6152* ( $d = 13.9$  nm) produced with comparable synthesis parameters. However, due to the chain-like framework structure, it is difficult to evaluate if the diameter observed by both characterisation methods is the same in case of LPR. The agglomeration is assumed to be attributed to the hypophosphite solution used for LPR and the excess of chlorides which allows the particles to stay mobile and enables them to grow together. For catalysts synthesised via GPR higher activities are achieved, as highlighted in section 4.1, due to the separation between particles and their small size.

Although not presented in this document, similar tendencies were discovered when comparing both reduction media for further catalysts presented in this thesis, independent of the precipitating agent (NaOH, Na<sub>2</sub>SiO<sub>3</sub>) used in VAM catalyst synthesis.

### 4.2.9 Extended X-ray absorption fine structure spectroscopy (EXAFS)

Since characterisation via EDX did not allow us to resolve single nanoparticles within the VAM catalysts in order to reveal their average composition, extended X-ray absorption fine structure (EXAFS) spectroscopy was used to obtain a more detailed insight into the average Pd and Au atom distribution within the catalyst particles. Two possible structural modifications of the bimetallic PdAu system are schematically shown in figure 4.35.

EXAFS studies were performed at the Deutsches Elektronen-Synchrotron (DESY) of the Hamburger Synchrotronstrahlungslabor (HASYLAB). Beamline X1 (energy range

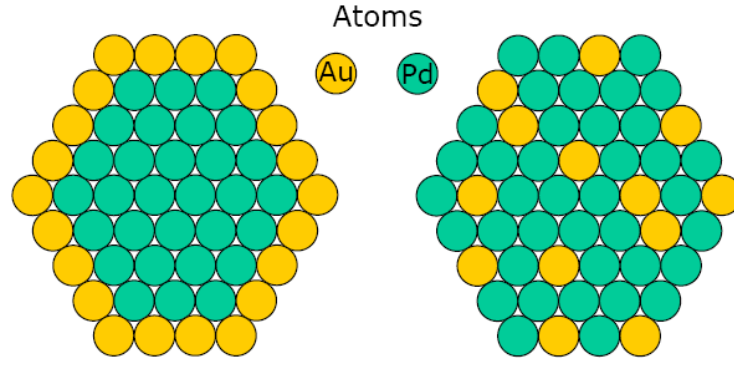


Figure 4.35: Different structures for bimetallic PdAu nanoparticles: Core-shell (left) and 3:1 alloy (right).

of X-ray = 6-80 keV) on the historically first DESY storage ring DORIS III (originally: Double Ring Store, energy = 4.45 GeV, current = 120 mA) was used for this characterisation method. The measurements were conducted in transmission mode (fig. 4.36) at the Pd  $K$  edge (24.350 keV) applying a Si(311) monochromator and at the Au  $L_3$  edge (11.919 keV) using Si(111). In both cases, a corresponding elemental foil was placed after the second ion chamber to provide an internal standard for the energy. The intensity,  $I_t$ , of an X-ray beam passing through a sample of thickness  $x$  can be obtained by the following Lambert-Beer equation with  $I_0$  as incident X-ray intensity and  $\mu$  representing the absorption coefficient:

$$I_t = I_0 e^{-\mu x} \quad (4.3)$$

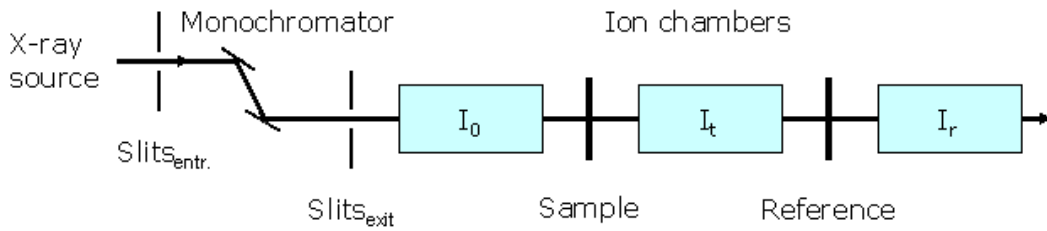


Figure 4.36: Experimental setup for EXAFS measurements in transmission mode using a Pd or Au foil as reference.

As previously described powder samples were obtained by scraping off the surfaces of about 100 of the catalyst spheres and this powder was used to prepare pellets for each catalyst specimen. For characterisation with EXAFS spectroscopy, catalysts  $B$ ,

*EX7273* and *EX7275* were chosen again in order to reveal possible structural differences due to variation of the reduction medium (LPR vs. GPR) and reduction temperature (150 vs. 250 °C) respectively.

The obtained EXAFS data were analysed with the Ifeffit software Athena 0.8.058 [78, 79]. After several adjustments, such as for the background of the absorption spectra, normalisation was accomplished according to procedures described in [80]. The resulting graphs are shown in figures 4.37 and 4.38 for both energy edges.

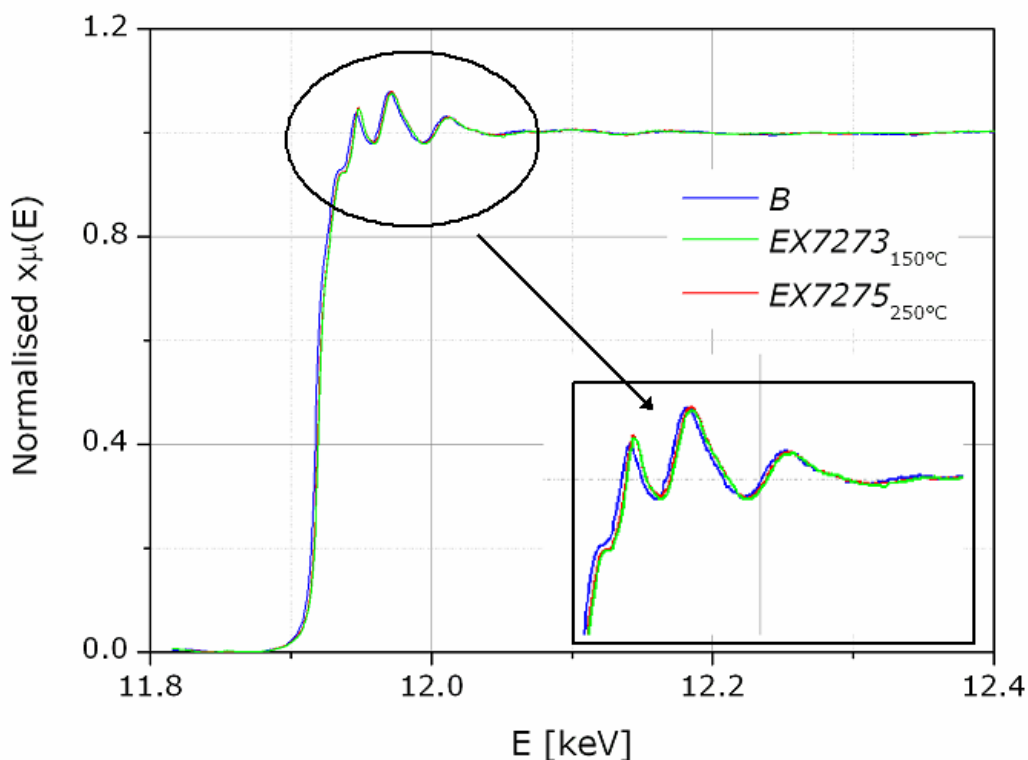


Figure 4.37: Normalised absorption spectra of catalysts *B* (blue), *EX7273* (green) and *EX7275* (red) for the Au  $L_3$  edge at 11.919 keV.

According to figure 4.37, consistent superposition is obtained at the Au  $L_3$  edge for all spectra. Therefore, it can be supposed that the corresponding structures are similar. By contrast, measurements at the Pd  $K$  edge revealed, at first view, differences between the liquid phase reduced catalyst *B* and the specimens from GPR. The first oscillation near the absorption edge (white line) reveals an evident decrease in energy for *B* compared to *EX7273* and *EX7275*. However, the second oscillation of *B* is higher than for the other two catalysts. This observation indicates that particles of *B*

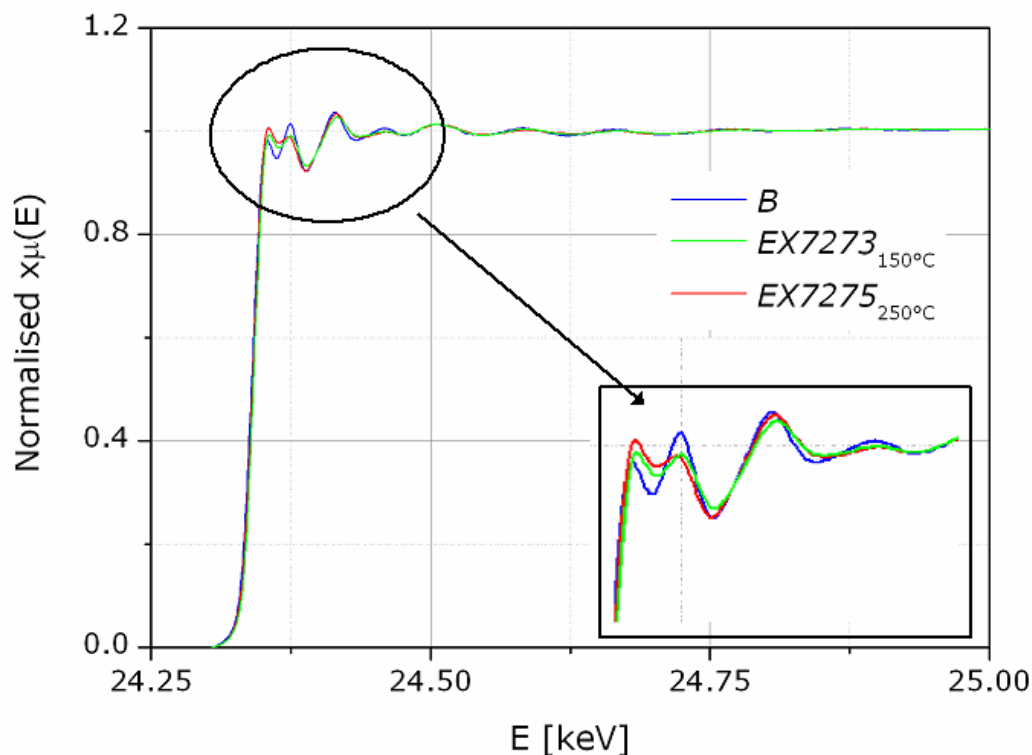


Figure 4.38: Normalised absorption spectra of catalysts *B* (blue), *EX7273* (green) and *EX7275* (red) for the Pd *K* edge at 24.350 keV.

exist as  $\text{Pd}^0$  rather than in an oxidic state. By contrast, for *EX7273* and *EX7275* a higher amount of oxidic Pd is suggested to be present. Probably the oxidic component derives from catalyst exposure to air. This effect will have to be verified in the following experiments.

Modulation of the absorption coefficients  $\mu(E)$  leads to the EXAFS function  $k\chi(k)$ . Figure 4.39 shows the Pd *K* edge spectra in *k* space. As this figure displays, the EXAFS of Pd foil is extended over a larger range of wavenumber *k* than Pd in the catalysts ( $15 \text{ \AA}^{-1}$  compared to  $12 \text{ \AA}^{-1}$ ). This can be attributed to higher crystallinity and coordination ( $N = 12$ ) of Pd in the foil compared to that in the nanoparticles. Furthermore, heavy elements show less declining scattering power [80]. In consequence, it is assumed that the catalysts analysed contain light element additives such as for example O. Additionally, this figure emphasises the difference in composition of *B*, obviously containing higher amounts of metal compared to the other two catalytic systems.

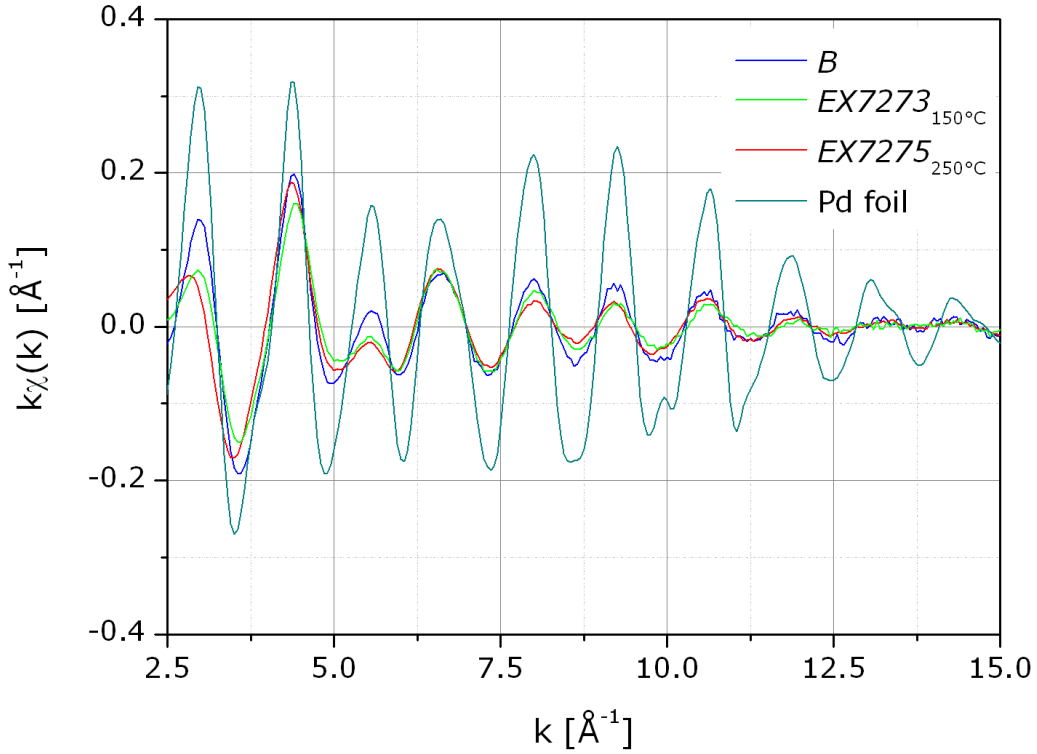


Figure 4.39: Transmission EXAFS spectra  $k\chi(k)$  of studied catalysts  $B$  (blue),  $EX7273$  (green) and  $EX7275$  and the Pd reference foil.

Since the raw EXAFS spectra decrease with  $k$ , weighting the higher- $k$  portion of the spectra by multiplying  $\chi(k)$  by  $k^3$  is a common method used in this analysis step [81]. Subsequently, a Fourier transformation (FT) from  $k$  to  $R$  space results in the radial distribution function [82]. The Fourier transforms  $|\chi(R)|$  of the catalysts studied are shown in figure 4.40 for the Au edge. Usually, only the amplitude of the complex function is shown.

All catalyst samples reveal a feature having three amplitudes with symmetric shapes between 1.9 and 3.2 Å. The amplitudes for catalyst  $B$  are marginally higher compared to those for  $EX7273$  and  $EX7275$ . Since the y-axis gives an indication for the number of neighbouring atoms  $N$ , this characteristic is expected to be lower for the catalysts than for the foil ( $N_{Au-Au} = 12$ ). An additional amplitude is observed for the PdAu catalysts. This implies a further backscattering atom which is assumed to be Pd.

The Fourier transforms  $|\chi(R)|$  with regard to Pd are displayed in figure 4.41 for all samples. The main feature, centered at about 2.4-2.5 Å, has a similar shape for all

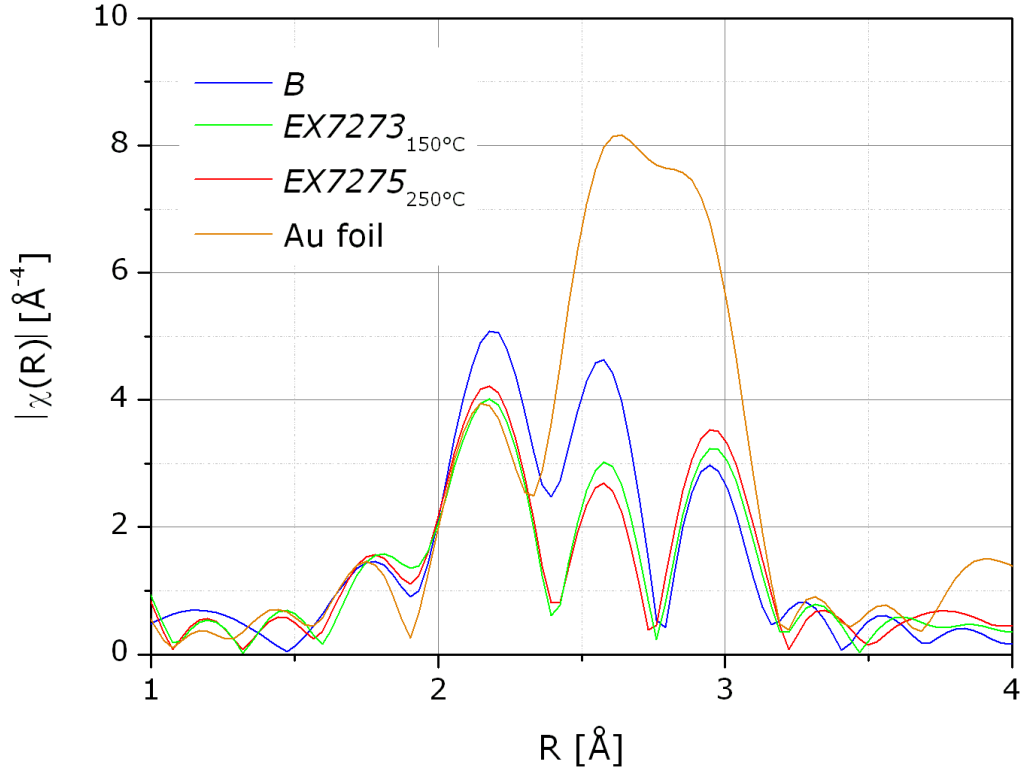


Figure 4.40: Fourier transforms  $|\chi(R)|$  of  $k^3\chi(k)$  for catalysts *B* (blue), *EX7273* (green) and *EX7275* (red) with regard to the Au edge.

three catalysts. Close to this amplitude, a shoulder can be determined in the range of 1.9-2.2 Å. This characteristic is supposed to describe the oxidic amount, whereas the feature at higher distances derives from Pd backscattering [80, 83]. In this context it is essential to consider that the distances,  $R$ , obtained by Fourier transformation only represent tendencies. For example, the Pd-O distance in PdO is 2.02 Å [84]. The deviation of the first peak, at approximately 2.08 Å, results from the phase-shift. Furthermore, the distance of Pd-Pd is about 0.3 Å lower than the theoretical value for the first coordination shell in the Pd crystal structure ( $R_{Pd-Pd} = 2.74$  Å). However, a shift of about  $\pm 0.5$  Å is typical for this analysis. The figure reveals additionally that the average coordination of Pd in the catalyst nanoparticles is much lower than 12 (Pd foil). Since an increase in coordination number  $N$  correlates with larger nanoparticles [85, 86], *B* is assumed to consist of a larger Pd<sup>0</sup> component than *EX7273* and *EX7275*.

In order to obtain quantitative information about the coordination number  $N$  and

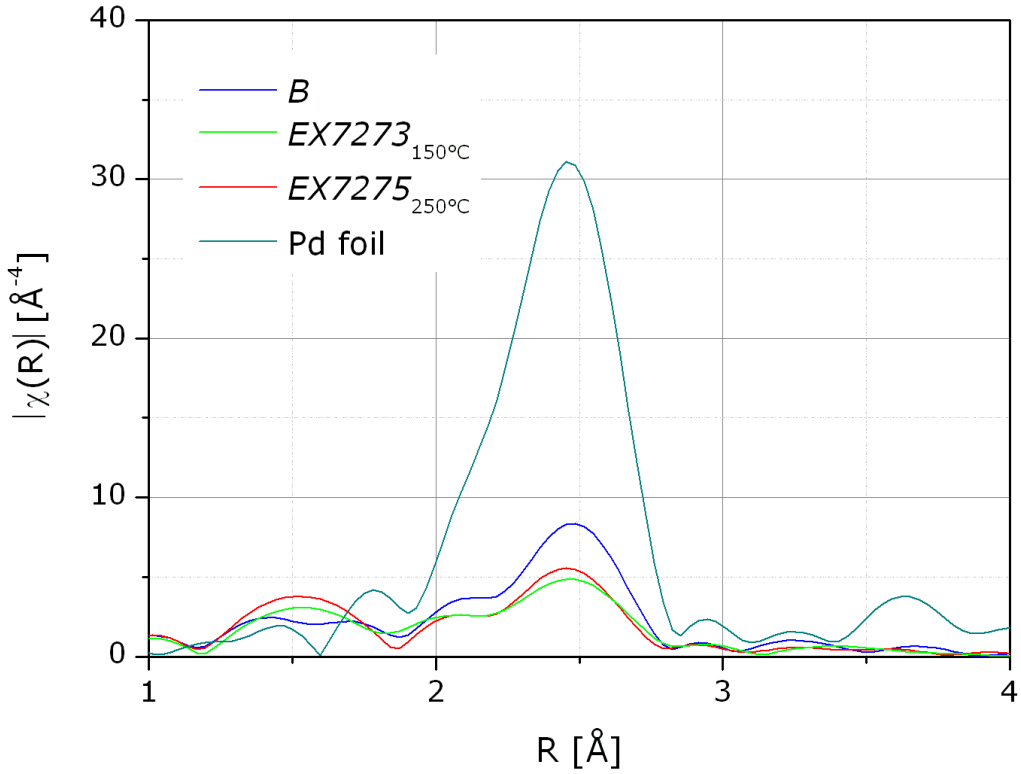


Figure 4.41: Fourier transforms  $|\chi(R)|$  of  $k^3\chi(k)$  for catalysts *B* (blue), *EX7273* (green) and *EX7275* (red) with regard to the Pd edge.

the distance  $R$ , simulations using XDAP software [87] were performed. For modelling of the EXAFS fits, calculations of the scattering amplitude and the phase-shift were performed with Feff 7.0 [88] based on structural input for Pd, Au and tetragonal PdO. These functions were applied to refine values for  $N$  and  $R$  until the model EXAFS function matched the experimental data.

Figure 4.42 gives an example of the model function compared to the experimental information, calculated for the Au edge of catalyst *EX7275*. The quality of the experimental data is comparatively high, so that up to values of approximately  $14 \text{ \AA}^{-1}$  a reasonable fit was obtained.

Parameters resulting from this fit and from simulations for the other model systems are summarised in table 4.15. Values of coordination number  $N$  and distance  $R$  are displayed for catalysts *B*, *EX7273* and *EX7275* with regard to both measured energy edges. The calculation errors were estimated to be for  $N \pm 10\%$  and for  $R \pm 0.02\%$ .

In general, iteration was performed until a goodness of fit (GOF) lower than 20 was

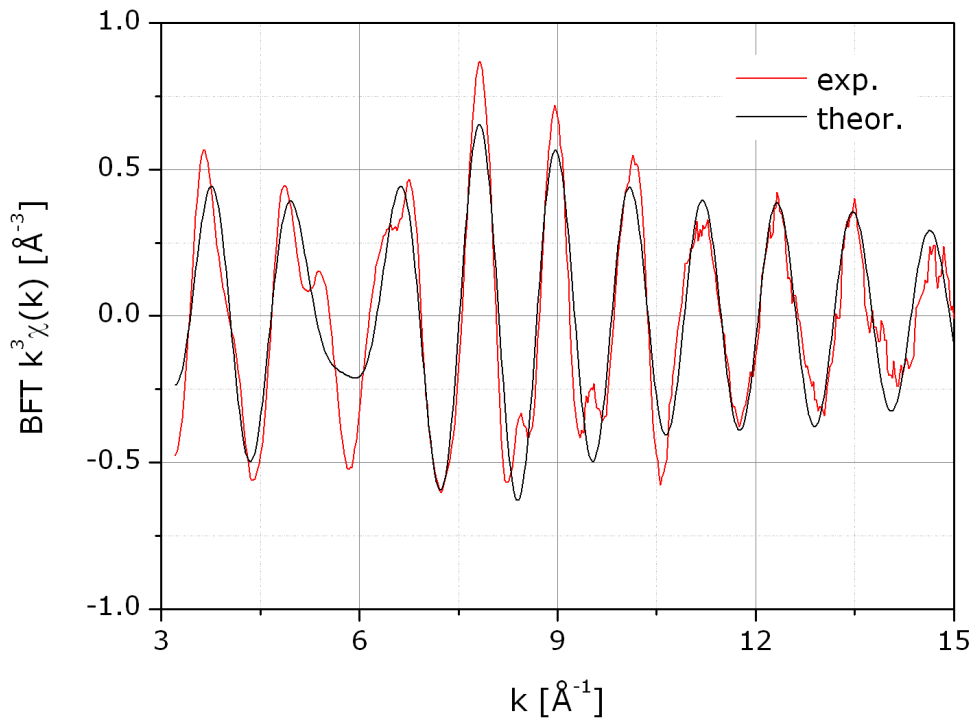


Figure 4.42: Refined EXAFS function (red) and calculated model (black) for catalyst *EX7275* achieved by modulation in  $k$  space with regard to the Au edge.

achieved with the XDAP software was achieved. Since  $N$  correlates strongly with the Debye-Waller factor  $\Delta\sigma^2$  [89], this value was kept constant for each data fit. The corresponding values are given in table 4.16.

Comparing the obtained values for  $N$  with regard to the Au  $L_3$  edge, it can be observed that they are similar for all catalysts. Based on Au as absorber atom, backscattering occurs from other Au atoms and Pd, respectively. Fitting a path for Au-O was not possible for the measured data. However, the coordination number determined for Au-Au ( $N_{Au-Au} = 7.1$ ) is significantly higher than for Pd-Au ( $N_{Au-Pd} = 0.8$ ), revealing Au-Au interactions as the main characteristic. Hence, the average coordination for Au atoms resulting from both metal backscatterers is about 8. Furthermore, information about the Au metal particle diameter is available from  $N_{Au-Au}$ . Based on previous experiments in literature [85, 86] for the metals Ni, Pt, Rh and Ir, the diameter resulting from the Au-Au coordination number obtained by EXAFS can be estimated to about 2.9 nm for all three catalyst samples.

Table 4.15: Simulation parameters using a constant Debye-Waller factor  $\Delta\sigma^2$  for the obtained EXAFS data of catalysts *B*, *EX7273* and *EX7275*.

<i>EX No.</i>	<i>B</i>	<i>7273</i>	<i>7275</i>	
Au <i>L</i> <sub>3</sub>				
Backscatterer	Au	Au	Au	
<i>N</i>	7.1	7.1	7.2	
<i>R</i> [Å ]	2.87	2.87	2.87	
-----				
Backscatterer	Pd	Pd	Pd	
<i>N</i>	0.8	0.7	0.8	
<i>R</i> [Å ]	2.93	2.92	2.93	
-----				
Pd <i>K</i>				
Backscatterer	Pd	Pd	Pd	
<i>N</i>	3.2	1.9	2.1	
<i>R</i> [Å ]	2.75	2.74	2.74	
-----				
Backscatterer	O	O	O	
<i>N</i>	1.8	1.9	2.6	
<i>R</i> [Å ]	2.06	2.03	2.00	

Table 4.16: Debye-Waller factors  $\Delta\sigma^2$  for different pairs of calculated model systems; the error is estimated to be  $\pm 5\%$ .

Pair	$\Delta\sigma^2$ [Å <sup>2</sup> ]
Au-Au	0.0062
Au-Pd	0.0060
Pd-Pd	0.0057
Pd-O	0.0060

In contrast to the Au  $L_3$  edge,  $N$  values calculated for the Pd  $K$  edge vary between the catalyst specimens. The coordination numbers for Pd-Pd decrease in the following order: *B* ( $N_{Pd-Pd} = 3.2$ ) > *EX7275* ( $N_{Pd-Pd} = 2.1$ ) > *EX7273* ( $N_{Pd-Pd} = 1.9$ ). This indicates higher amounts of Pd-Pd interaction in catalyst *B*. Despite the inconsistency

in coordination number, a calculation [85, 86] showed only marginal differences in Pd particle sizes. In the case of catalyst *B*, the particle diameter was estimated to 0.9 nm and for both GPR catalysts to 0.8 nm.

According to the calculated model systems, Pd-O represents a further phase. For this interaction the  $N$  of *EX7275* ( $N_{Pd-O} = 2.6$ ) is larger than that of *EX7273* ( $N_{Pd-O} = 1.9$ ) and *B* ( $N_{Pd-O} = 1.8$ ). Considering the ratio  $N_{Pd-Pd}/N_{Pd-O}$  for these three samples, it becomes apparent that the liquid phase reduced catalyst *B* contains more Pd<sup>0</sup> compared to the analogues prepared using GPR. Between both calculated ratios for *EX7273* ( $N_{Pd-Pd}/N_{Pd-O} = 1$ ) and *EX7275* ( $N_{Pd-Pd}/N_{Pd-O} = 0.8$ ) a marginal difference, indicating more oxidic Pd in *EX7275* can be determined. However, for all catalysts the resulting average Pd atom coordination number is significantly lower than for Au, indicating either a Pd shell or smaller Pd clusters attached to the Au nanoparticle.

Since an Au-Pd interaction was observed for all catalysts, a contribution of the pair Pd-Au was expected to be found as well. However, EXAFS model system calculations including this interaction did not result in satisfactory agreement with the data for *EX7273* and *EX7275*. Only in case of catalyst *B* both modelling routes, *i. e.* with and without Pd-Au, led to reasonable results. The corresponding parameters for *B* for the EXAFS model containing Pd-Au as additional interaction are shown in table 4.17. The Debye-Waller factors  $\Delta\sigma^2$  remained the same as before (tab. 4.16). Therefore only  $\Delta\sigma^2$  for the additional interaction Pd-Au is given in this table.

According to this overview, the alternative model system reveals similar parameters for the Pd-Pd and Pd-O contributions compared to the previous calculation results (tab. 4.15). The coordination number of Au as backscatterer is rather small compared to  $N$  of the other components. Even though this additional feature results in a better GOF than the model without Pd-Au, its calculation is marginally approaching the resolution.

Regarding the distances  $R$  achieved by modelling, it can be concluded that, within the accuracy of analysis, the obtained values agree in most cases very well with the analogues described in literature [84, 90–92]. However, the distance of the Au-Pd interaction represents an exception. Table 4.18 depicts the comparison of both values for each pair. Since the determined distances are almost similar for all of the analysed

Table 4.17: Alternative parameters resulting from simulations with Pd-Au as additional scattering path for the obtained EXAFS data of catalysts *B*.

<i>EX No.</i>	<i>B</i>
Pd <i>K</i>	
Backscatterer	Pd
<i>N</i>	3.1
<i>R</i> [Å]	2.75
-----	
Backscatterer	O
<i>N</i>	1.9
<i>R</i> [Å]	2.04
-----	
Backscatterer	Au
<i>N</i>	0.6
<i>R</i> [Å]	3.06
$\Delta\sigma^2$ [Å <sup>2</sup> ]	0.0059

catalysts, an average value will be used subsequently as representative.

Table 4.18: Representative comparison between distances *R* obtained by EXAFS model fitting and values of literature; all results are represented in Å [84, 90–92].

Pair	EXAFS model	Literature
Au-Au	2.87	2.88
Au-Pd	2.93	2.81
Pd-Pd	2.74	2.74
Pd-O	2.03	2.02

In accordance with distances *R* obtained for the Au-Pd interaction, the simulated value for Pd-Au of *B* ( $R_{Pd-Au} = 3.06$  Å) is also higher than suggested in the literature ( $R_{Au-Pd} = 2.81$  Å) [90]. Since the distance between these two atoms given by literature describes a homogeneous alloy, this structure is assumed not to exist in the catalysts analysed here. For *B*, *EX7273* and *EX7275* higher distances between Pd and Au were observed compared to the literature. This can be explained by a higher average number

of Au neighbours. Taking all this information into account, structures of the three different catalyst samples were proposed, as schematically illustrated in figure 4.43.

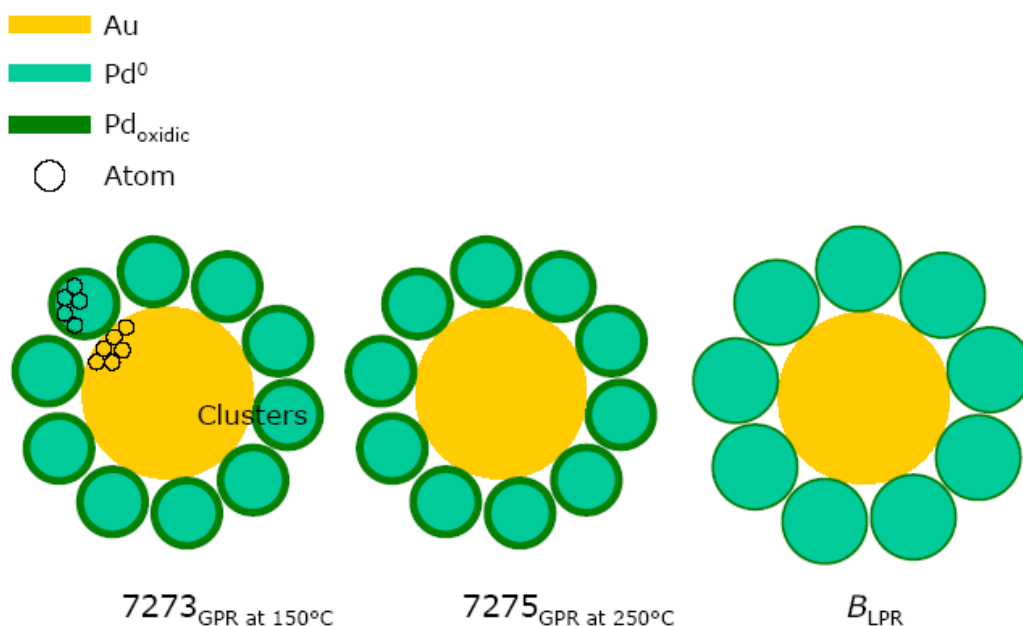


Figure 4.43: Structural difference between the three catalysts determined by EXAFS analysis.

Based on these results, locally independent clustering of Au and Pd atoms is assumed to occur for all catalysts. Considering the similar environments for Au, a significant difference in the presented core-shell distribution originates from  $\text{Pd}^0$  and oxidic Pd. Catalyst *B* reduced via LPR is expected to contain a higher amount of  $\text{Pd}^0$  compared to oxidic Pd. By contrast, catalysts reduced via forming gas are composed of significantly more oxidic Pd than the LPR synthesised products. This can be explained by the presence of small metal particles resulting from GPR (tab. 4.13, fig. 4.29). These particles show a high reactivity and react instantaneously subsequent to GPR with oxygen from the atmosphere.

Based on the different particle diameters obtained by Pd dispersion measurements (tab. 4.13) and TEM (*cf.* sec. 4.2.8) for LPR ( $\geq 10$  nm) and GPR ( $\approx 4$  nm), larger Pd particle sizes were expected for catalyst *B* compared to *EX7273* and *EX7275*. But since EXAFS only provides average diameters, smaller Pd particles are assumed to be present in catalyst *B* among larger ones, which finally results in a particle size of 1 nm. In addition, the fact that the Pd-Au interaction is only observable for *B* can be finally attributed to this difference in Pd particle sizes.

The results achieved via EXAFS spectroscopy confirm that this characterisation technique is very promising for analyses of different VAM catalysts. The present study provided information about the atomic Pd and Au distribution within the catalyst particles. From both structures presented above (fig. 4.35), the core-shell design could be verified for all investigated VAM catalysts.

### 4.3 Summary of results

As a conclusion to this chapter, the main results comparing both reduction media (LPR vs. GPR) will be given in the following table.

**Table 4.19:** Main differences in performance and further characteristics of catalysts produced via LPR and GPR.

Characteristic	Characterisation method	LPR		GPR
$S_{VAM}$ [%]	Catalyst screening	$\approx 94$	<	$\approx 96$
$STY_{VAM}$ [g <sub>VAM</sub> Lh <sup>-1</sup> ]	Catalyst screening	$\approx 500$	<	$\approx 700$
Shell thickness [ $\mu$ m]	Optical microscopy	330	>	246
Palladium dispersion [%]	CO chemisorption	8	<	25
Mean particle size [nm]	CO chemisorption	14	>	4
Mean particle size [nm]	TEM	$\geq 10$	>	$\approx 4$
Particle morphology	TEM	agglomerated		isolated
Pd state on particle surface	EXAFS	more Pd <sup>0</sup>		oxidic Pd

# Chapter 5

## Final discussion

In the previous sections, syntheses of high performance VAM catalysts prepared by employing systematic variations of different parameters were presented. Due to the applied Temkin reactor concept allowing efficient heat and mass transport, it was possible to distinguish the prepared catalysts clearly with regard to their selectivity and particularly space time yield within a wide range of values. As the screening results showed, the highest selectivities were achieved by samples synthesised with SCAG proprietary KA-Zr carriers using the LPR route. Outstanding improvement of about 2.4 % on average for this experimental series derives from lower BET surface areas compared to the KA 160 support. As a result, bigger pores in these materials lead to a more efficient mass transport than for catalyst *B*. Furthermore the BET surface area reduces the dispersion of nanoparticles, while simultaneously increasing their sizes which finally improves the selectivity by eliminating the unselective Pd atoms and clusters. However, this results in decreasing activity. But since zirconium dioxide is known to enhance the activity of VAM catalysts [65], this component counteracts the effect of nanoparticle size. As expected, samples based on the KA-Zr carriers turned out to be more active than the benchmark. Considering that GPR achieves significantly higher *STY* than LPR, great potential can be assigned to Zr-catalysts if synthesised with a gas mixture of 5 % H<sub>2</sub> ( $F_{H_2} = 250 \text{ NmLmin}^{-1}$ ) and 95 % N<sub>2</sub> ( $F_{N_2} = 4750 \text{ NmLmin}^{-1}$ ) as reduction medium.

The use of KA 0 as carrier and Na<sub>2</sub>SiO<sub>3</sub> as precipitating agent resulted also in high performance VAM catalysts. However, as previously described in section 4.1, improve-

ments were marginal in comparison to the other catalyst series (*cf.* fig. 4.4 and 4.7). To advance VAM catalyst synthesis based on the KA 0 support, further input will be necessary to attain, for example, an optimum Pd/Au ratio. Catalysts synthesised chronologically later (higher *EX No.*) showed an elevated gain in performance. Aside from the already mentioned Zr-series, GPR led to remarkable performance values especially in *STY*. Due to the 40 % higher *STY* compared to the benchmark, a compromise to lower process temperatures can be afforded for these VAM catalysts in order to further improve the selectivity. High potential is therefore expected for GPR.

Furthermore, the variation in reduction medium (LPR vs. GPR) and precipitating agent (NaOH vs. Na<sub>2</sub>SiO<sub>3</sub>) revealed that the shell thickness is a very important parameter in the catalyst performance. Lower shell thicknesses of 197.3  $\mu\text{m}$  (LPR) and 135.0  $\mu\text{m}$  (GPR) were observed using Na<sub>2</sub>SiO<sub>3</sub> as less alkaline base compared to NaOH (229.8  $\mu\text{m}$  (LPR), 191.9  $\mu\text{m}$  (GPR)). This difference is attributed to slower diffusion of Na<sub>2</sub>SiO<sub>3</sub> due to the higher molecular size. In addition, GPR resulted independent from the base chosen also in catalysts with thinner shells compared to LPR. However, the variation in shell thickness showed that less improvement in *S* (base mixture series) and *STY* (*EX6316*) can occur if the shell is too thin.

In view of the fact that the most significant differentiation was observed between catalysts prepared using LPR and GPR, samples from each reduction medium were chosen for a detailed characterisation using Pd dispersion measurements, XRD, TEM and EXAFS. In order to optimise the precious metal intensity compared to the bentonite carrier, the shell surfaces of about 100 catalyst spheres were scraped off for preparation of powder specimens.

For both reduction media (LPR and GPR) XRD analysis of fresh and spent (after time-on-stream over several days) VAM catalysts revealed reflections caused by Pd crystals containing interstitial hydrogen atoms. Further features could be assigned to the KA 160 support. Both broad and sharp characteristic peaks in the carrier diffraction pattern can be confirmed by literature describing other commercial VAM catalysts. In this context Macleod *et al.* examined the comparison between a fresh catalyst and a sample aged 14 months under industrial conditions [32]. Due to the longer ageing compared to the test period in this study, differences in average particle sizes

between those fresh (5 nm) and aged (12 nm) samples were more significant. According to the calculations via the Scherrer equation presented herein, VAM catalyst particles reduced in the liquid and gas phases increased in diameter by only about 1 nm after testing. However, this deviation is in the margin of error and since the Pd reflections observed in this thesis are, in all cases, rather broad and relatively low in intensity, using the FWHM of these reflections to calculate the mean particle diameter may be subject to a notable error, as later approved by TEM analysis showing an increase of about 2-4 nm. In a current study, Pohl *et al.* pointed out that determining crystallite sizes and alloy compositions from the width and position of XRD reflections is not a meaningful approach for inhomogeneous systems like VAM catalysts [93]. A combination of XRD characterisation with TEM-EDX is therefore recommended by this research group. Limited sintering of particles in Pd(1 wt %) and Pd(5 wt %) catalysts supported on a high surface area silica ( $600\text{ m}^2\text{g}^{-1}$ ) was also observed via XRD during the VAM reaction by Han *et al.* [33]. In addition, XRD results from the Pd(5 wt %) catalyst [36] showed that the data quality can be easily improved by using significantly higher amounts of Pd metal compared to the low concentration found in commercial VAM catalysts used herein. Due to the low metal amounts it was rather complicated to reveal the differences between the LPR and GPR routes presented herein, used for the industrial VAM production, by applying XRD analysis. Thus, catalyst preparation using higher Pd concentrations in combination with both reduction media may be a promising alternative for XRD optimisation. However, it has to be pointed out that in this case, the realistic VAM catalyst would not be the system under investigation.

As for XRD, measurements using EDX were also limited because of the low Pd and Au concentration in VAM catalysts. Since the amount of carrier exceeded considerably the concentration of the noble metals, it was difficult to obtain high intensity peaks suited for analysis. Furthermore, EDX revealed that the particle diameters were too small for a separate evaluation. With the equipment employed in this investigation only particles larger than 20 nm could be analysed. The study of catalyst *B* indicated an agglomeration of particles which was confirmed by further characterisation methods such as TEM and Pd dispersion.

The characterisation of samples varying in the reduction medium turned out to be

more efficient using TEM analysis. Results showed that the samples prepared by LPR consisted almost exclusively of agglomerated nanoparticles, whereas GPR led to a higher dispersion of smaller and isolated particles. This is in good agreement with the calculated particle sizes from the experimentally determined Pd dispersions ( $d_{LPR} = 13.9\text{ nm}$ ,  $d_{GPR} = 4.4\text{ nm}$ ). Furthermore, the observed agglomeration by applying LPR is consistent with results published in literature. Zhang claimed in US patents 5,721,189 [94] and 5,962,366 [95] that addition of chloride induced a significant growth of carbon supported Pd catalyst particles. This process decreased the activity of the treated hydrodechlorination catalysts, thereby increasing their resistance against catalyst poisons to improve the lifetime. With regard to the VAM catalyst system, formation of chloride films can also increase the mobility of nanoparticles. These films would lower the adhesion of particles to the bentonite carrier. Consequently, particles were expected to grow together until reaching a size big enough to cause immobility. The ability to form chain-like framework structures may be supported by quartz defects existing in the KA carrier. Compared to GPR, where it can be supposed that many nuclei are formed concurrently, reduction in liquid phase would be initialised only by a few nuclei growing together.

A kinetic examination by Han *et al.* [33] revealed that the catalyst performance was improved by small particles compared to large sizes. In accordance with this result, higher selectivities and activities were herein obtained by smaller particle diameters arising from GPR compared to LPR catalysts (*cf.* sec. 4.1). VAM formation is therefore assumed to be particle size-sensitive.

Since only a minority of all VAM catalysts discussed in the literature is close to the commercial products, comparison with the specimens synthesised herein is generally questionable. In addition, the small part of industrial VAM catalysts correlated with scientific information was reduced with hydrazine. Due to the toxicity of this agent, it was replaced by sodium hypophosphite in this work. However, assuming equivalent processes in the liquid phase for both reducing agents, similar structural distribution of particles can be observed compared to this dissertation. Macleod *et al.* determined a clear tendency for metal particles in the fresh sample to form clusters, varying in shape [32]. Moreover, this research group revealed with HREM-EDX that some PdAu

particles are surrounded by lower contrast networks identified as highly dispersed Pd metal components.

Comparison of particle sizes observed with TEM analysis between fresh and spent catalysts showed that sintering occurred for samples from both LPR and GPR. Due to the rather small test period compared to samples aged for several months [32] or even years, no changes in particle diameter were expected. However, an increase of 2-4 nm in particle size was visible. By contrast, sintering of Pd catalysts studied by Han *et al.*[33] was less significant than in the present study. But since the reaction period was shorter, a smaller increase in diameter seems reasonable.

In this thesis, EXAFS measurements were performed in order to determine the geometric structure defined by the average coordination and interatomic distances around each Pd and Au atom. As the EXAFS study showed, the atoms of Pd and Au are distributed in a core-shell design for all investigated VAM catalysts. Moreover, the results of particle sizes obtained by Pd dispersion and TEM analysis should be verified. However, Pd particle sizes were estimated to vary only marginally between LPR (0.9 nm) and GPR (0.8 nm). Particle sizes for Au were as well determined to be similar within the three investigated VAM catalysts (2.9 nm). In accordance with the particle sizes studied with previous characterisation methods, both small and large cluster sizes of Pd<sup>0</sup> are supposed to be present for the exemplary sample reduced in the liquid phase. Thus, an average diameter of about 1 nm is explainable. This can be explained by the fact that approach of Pd atoms to the Au core was enabled during LPR and favoured by the reduction solution.

The observed difference in performance between samples of LPR and GPR could be therefore primarily explained by this variation in particle diameter. However, distinguishing the two catalysts reduced at different temperatures (150 °C and 250 °C) was rather difficult with EXAFS. Although these catalysts varied significantly in performance, considerable deviations on the microscopic scale were difficult to reveal.

Subsequently, a model for the evolution starting from both precipitated metal hydroxides until the final metal distribution after a longer period of catalyst testing will be presented. It will be shown that this process is in accordance with the structure determined in the EXAFS model. The following sequences are supposed to occur for

LPR and GPR, respectively. After precipitation highly dispersed Pd and Au hydroxides are expected to be present. Since the ionisation potential of Au atoms is known to be higher than for Pd (9.226 eV vs. 8.337 eV) [69], the more precious metal transforms into its metallic state at first. It is supposed that these atoms agglomerate, in order to increase stability, forming small Au particles. In the meantime Pd hydroxides are reduced as well leading to a Pd agglomeration in an analogous manner to decrease the surface energy. Thus, these agglomerates tend to cover the core of metallic Au particles.

According to the EXAFS results, some oxidic Pd was found to be present for both catalysts that were reduced in gas phase. By contrast, significantly more Pd<sup>0</sup> compared to oxidic Pd was revealed for LPR. This difference can be attributed to the passivation step during GPR. Due to the contact with oxygen-depleted air, a thin protective oxide film forms on the Pd particles in this case. However, a certain part of the determined Pd-O interaction could also derive from Pd interaction with the carrier. Since the KA support consists of many oxides, especially SiO<sub>2</sub>, it can be assumed that Pd also interacts with these oxygen atoms. It is important to keep in mind that EXAFS provides average results. Therefore it is also possible that a certain amount of Pd particles (oxidic or Pd<sup>0</sup>) exists isolated in the catalyst system. This arrangement is schematically illustrated in figure 5.1 for LPR.

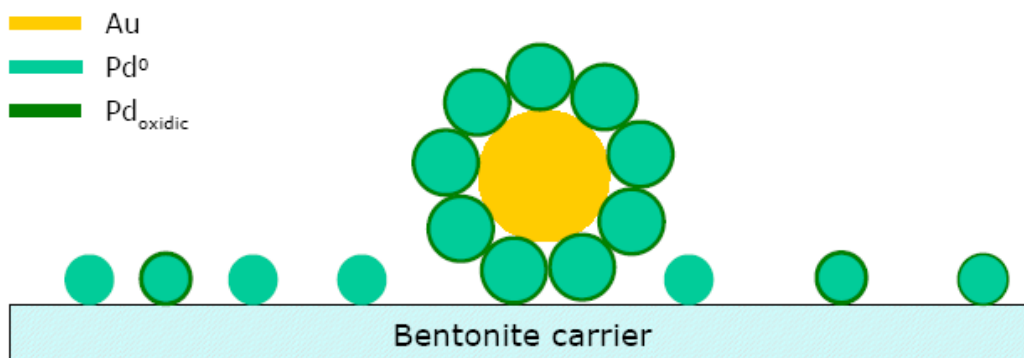


Figure 5.1: Model of structural arrangement in the case of the benchmark synthesised by LPR.

An indication for this structural arrangement derives from the average Pd and Au particle diameters, calculated from the coordination numbers  $N_{Pd-Pd}$  and  $N_{Au-Au}$ . According to the experimental EXAFS results, these diameters are similar for both LPR

and GPR ( $d_{Pd} \approx 1$  nm,  $d_{Au} \approx 3$  nm). Based on the core-shell structure, the diameter of a bimetallic particle would be about 5 nm. Considering a GPR catalyst, this size would confirm the results from both Pd dispersion and TEM (tab. 4.19). On the other hand, studies with these characterisation methods showed significantly larger particles of more than 10 nm for the LPR. Therefore a Pd particle diameter of about 3 nm would be expected from  $N_{Pd-Pd}$  to support the previous measurements. The existence of isolated Pd particles on the surface, as shown in the figure above, enables finally to explain the small average diameter found by EXAFS.

Bimetallic clusters consisting of a gold enriched core covered by Pd are moreover found in the literature by EXAFS analysis of bimetallic PdAu catalysts which can also be used in other chemical reactions. Reifsnnyder and Lamb [96] observed this structural distribution for Pd-Au/SiO<sub>2</sub> (1.3:1, pH 7) catalysts. However, another sample synthesised with similar conditions (1:1, pH 10) revealed homogeneous PdAu alloy clusters. It was supposed that reduction in this case occurred simultaneously rather than sequentially during catalyst preparation. Due to this observation, the sequential reduction of gold and palladium assumed in this study can be confirmed. In addition, Harada *et al.* use an experimental series to support the dependence of particle structure on reduction order during synthesis of these clusters [97, 98]. They studied three preparation methods by reducing first Pd and then Au as well as in the opposite order and also simultaneously for two different Pd/Au ratios (4:1 and 1:1). Different structures in the resulting bimetallic clusters were obtained by these variations according to EXAFS measurements. In accord with the model established in this thesis, the simultaneous reduction of a catalyst with Pd/Au ratio 4:1 also led to a gold core based structure. A model composed of a palladium decorated core of gold atoms, was furthermore stated by Davis and Boudart [99] for a PdAu catalyst system (mole ratio<sub>Pd:Au</sub> = 60:40) supported on silica. In a current paper, Marx and Baiker investigated the interaction of Au and Pd in bimetallic catalysts used in the selective oxidation of benzyl alcohol [100]. This study also suggests the presence of a gold rich core and a palladium rich shell.

Structures consisting of a rather noble core covered by less noble atoms can be found as well in other catalyst systems. For instance, equal effects are observable for PtPd [84] and PtRu catalysts [101]. However, the formation of different bimetallic structures

is assumed to be dependant on many criteria during synthesis.

Finally, when exposing the catalysts to the educts during the VAM reaction, oxidic Pd is easily reduced by ethylene to Pd<sup>0</sup>. Depending on temperature and time, the Au core-Pd shell structure might still be intact. On the other hand, partial alloying could already start to occur. Since Au has a lower surface energy than Pd (1.63 Jm<sup>-2</sup> [102] vs. 2.05 Jm<sup>-2</sup> [103]), it is assumed that the more precious metal preferentially segregates at the surface. Therefore alloy formation exhibiting a gold enriched surface is expected to result, as confirmed by several studies [104, 105]. Furthermore, this segregation process can be influenced on the surface by carbon deposition on Pd particles described in [17, 18, 39]. In addition, the chemical potential is expected to change when the nanostructure is exposed to the hydrocarbon educts due to the different atmospheres during reduction and VAM reaction. This might also affect the alloy forming process. However, reaching this atomic distribution is expected to be rather time consuming. Having achieved an equilibrium condition of alloy formation, considerable sintering of particles to about 15-20 nm is expected to occur over a period of 2-3 years. Due to the experienced catalyst deactivation, VAM catalyst are replaced in industry after this lifetime. Since the equilibrium condition differs significantly from the situation after reduction studied herein, EXAFS measurements of VAM catalysts in different reaction states would be of high interest. However, realisation of this experiment is rather complex.

In general, characterisation of the synthesised VAM catalysts was the biggest challenge in this thesis. It can be assumed that the high complexity of this system is one reason why only little information can be found in literature. However, summarising all results, it can be postulated that a Au core-Pd shell structure is predominant in fresh VAM catalysts. Based on this bimetallic neighbouring system high catalyst performances were realised during VAM reaction for both LPR and GPR. Furthermore, it was shown that a significant difference in activity between both reduction media is supposed to be associated with the Pd dispersion.

# Chapter 6

## Outlook

The present study showed that systematic variation of different synthesis parameters improved the performance of VAM catalysts. Comparison with the state-of-the-art benchmark *B* revealed an outstanding increase in selectivity of 2.4 % for samples synthesised with the KA-Zr carriers. Based on the obtained performance data, an optimum Zr amount embedded in the support is determined to be 3-7 wt % for highest selectivities. Zr concentrations of 8-19 wt % showed also an enhancement in selectivity compared to the reference, but less significantly. However, the activity (*STY*) within this experimental series was rather similar for all catalysts, not indicating, as expected, any correlation to the Zr amount. Since it was observed that higher Zr concentrations resulted in unfavourable blurred catalyst shells, not preferential for the performance, increased amounts in the support are not reasonable. Therefore the future objective should be to gain activity using GPR. High potential is estimated to result from combination of a KA-Zr carrier and GPR.

Considering the fact that GPR leads to an enormous increase of almost 40 % in activity compared to the benchmark, LPR should not be further pursued for synthesis of VAM catalysts. Since the realisation of 20 % higher activity represents already a tremendous gain for VAM formation, a compromise to lower process temperatures such as 135 °C can be afforded with loss of *STY* in order to improve the selectivity. A welcome side effect when applying GPR is also the avoidance of additional waste waters resulting from LPR. Hence, GPR is also preferential with regard to noble metal

recovery. In order to further enhance the selectivity, KA carriers with slightly lower BET surface area such as for example  $150\text{ m}^2\text{g}^{-1}$  would be an additional promising alternative.

Since only marginal impacts on the performance were determined for catalysts prepared with  $\text{Na}_2\text{SiO}_3$  enriched fixation solutions, this base should not be subject to further investigations. In addition, using KA 0 as carrier also turned out to be less beneficial compared to other parameter alterations. Higher Pd loading would be necessary in order to achieve a better performance than the benchmark, though not being profitable.

Apart from parameter changes in the wet-chemical synthesis via incipient wetness, a novel and promising method to produce VAM catalysts consists of the application of advanced coating technology. This new path for metal precursor impregnation is already claimed in patent literature [57] (*cf.* chp. 1). High importance will be attributed to further experiments and development efforts in this field. One of the biggest advantages using this preparation method is the ability to control shell thickness. In addition, SEM-EDX mappings revealed a more homogeneous distribution of Pd throughout the catalyst shell, as shown in figure 6.1. The specimen illustrated in this mapping was produced by SCAG.

As the comparison in figure 6.2 illustrates, catalysts synthesised by incipient wetness method reveal accumulation of precious metals along the boundary area between the shell and interior of the sphere, shown in figure 6.2 a) (*cf.* sec. 4.2.7). Figure 6.2 b) proves the enormous advancement in homogeneity of metal distribution obtained by this new synthesis technology, allowing the development of high performance catalysts.

With regard to characterisation methods, further investigations using high resolution transmission electron microscopy (HRTEM) in combination with EDX (similar lattice spacings for Pd and Au) would be a promising alternative to study single catalyst particles [106]. This analysis could indicate the distribution of Pd and Au in one particular nanoparticle. In addition, statistics of the measured Pd/Au ratios existing in different locations could give information about the metal homogeneity. However, a wide range of Pd/Au distributions can be expected for this bimetallic system since both metals are completely miscible [107].

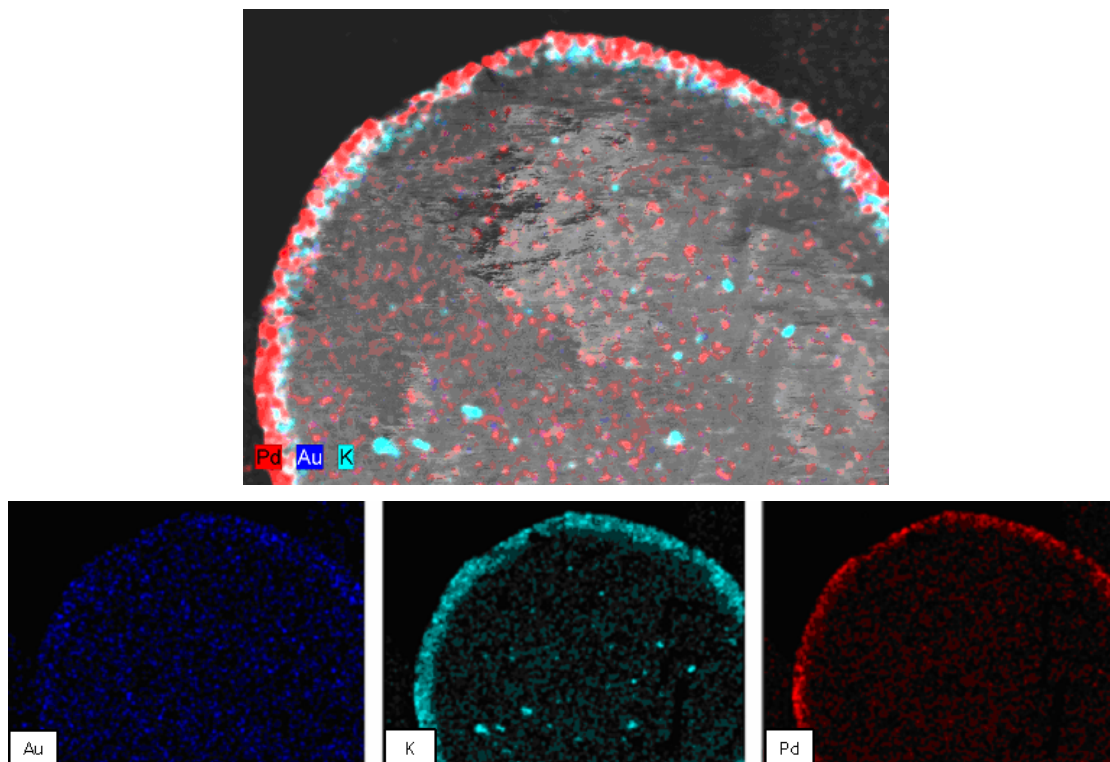


Figure 6.1: SEM-EDX mapping indicating the distribution of elements in the catalyst shell for a sample synthesised by coating.

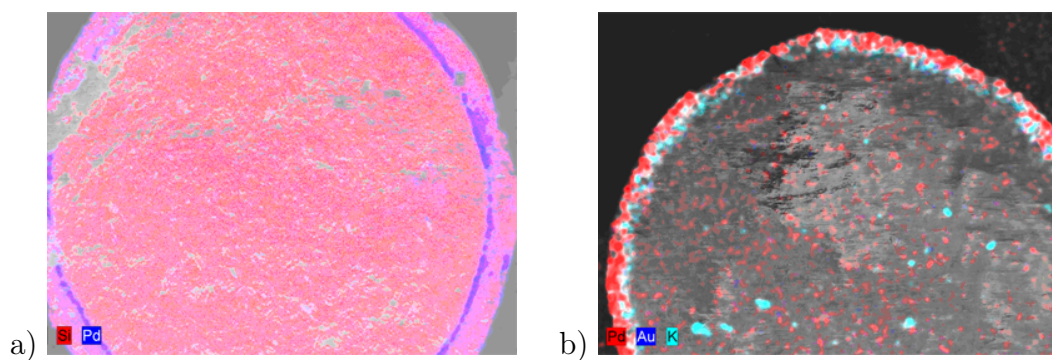


Figure 6.2: SEM-EDX mappings for catalysts synthesised via a) IW method and b) coating technology, indicating different Pd distributions in the shell.

It would also be of interest to analyse spent catalysts after the initial induction period of hyperactivity, as well as after several months time-on-stream in order to reveal whether the cluster arrangement has transformed into alloyed particles. In situ experiments would be of further significance for a deeper understanding of commercial VAM catalysts.

Finally, a reduction of the complexity of the VAM catalyst system, for example by replacing the bentonite carrier with pure silica or by increasing the metal concentrations remarkably, could simplify the characterisation. But what would these results be worth considering that the investigated system does not represent the real VAM catalyst? In the priority program 1091 of the DFG (German research foundation), the bridge between model and real catalysts was subject of studies [108]. With regard to silver catalysts used in acrolein hydrogenation two types of systems were examined in order to answer the question of transferability: Single crystals which are well defined and easy to characterise, but also high pressure and highly disperse systems with increased complexity which render the characterisation difficult. Since the industrial VAM catalyst was investigated in this study, disadvantages in characterisation due to its complexity were accepted while being rewarded by results of a real catalyst system.

# Chapter 7

## References

- [1] *Chemical Week* **25.06.2003**, 31.
- [2] E. Burrige, *ICIS Chemical Business* **2008**, 273, 50–51.
- [3] J. Smidt, W. Hafner, R. Jira, J. Sedlmeier, R. Sieber, R. Rüttinger, H. Kojer, *Angew. Chem.* **1959**, 71, 176–182.
- [4] I. I. Moiseev, M. N. Vargaftik, Y. K. Syrkin, *Dokl. Akad. Nauk. SSSR* **1960**, 133, 377–380.
- [5] H. Krekeler, H. Schmitz, *Chem.-Ing.-Tech.* **1968**, 40, 785–788.
- [6] Farbwerke Hoechst Aktiengesellschaft, *Chem. Ind.* **1968**, 1559.
- [7] Farbenfabriken Bayer Aktiengesellschaft, *World Pet. Cong. Proc.* **1968**, 5, 41.
- [8] H. Fernholz, L. Hornig, T. Quadflieg, H. J. Schmidt, F. Wunder (Farbwerke Hoechst Aktiengesellschaft, vormalis Meister Lucius & Bruning), US 3,658,888, **1972**.
- [9] T. C. Bissot (E. I. Du Pont de Nemours and Company), US 4,048,096, **1977**.
- [10] S. Nakamura, T. Yasui, *J. Catal.* **1971**, 23, 315–320.
- [11] S. M. Augustine, J. P. Blitz, *J. Catal.* **1993**, 142, 312–324.
- [12] R. S. Shetty, D. H. Kashyap, S. B. Chandalia, *Indian J. Technol.* **1972**, 11, 170–173.

- [13] W. J. Bartley, G. G. Harkreader, S. Jobson, M. Kitson, M. Lemanski (BP Chemicals Limited), US 5,274,181, **1993**.
- [14] H. Erpenbach, H. Glaser, K. Sennewald, W. Vogt (Knapsack Aktiengesellschaft), US 3,631,079, **1971**.
- [15] Y. F. Han, J. H. Wang, D. Kumar, Z. Yan, D. W. Goodman, *J. Catal.* **2005**, *232*, 467–475.
- [16] M. Neurock, *J. Catal.* **2003**, *216*, 73–88.
- [17] M. S. Chen, K. Luo, T. Wei, Z. Yan, D. Kumar, C. W. Yi, D. W. Goodman, *Catal. Today* **2006**, *117*, 37–45.
- [18] D. Kumar, M. S. Chen, D. W. Goodman, *Catal. Today* **2007**, *123*, 77–85.
- [19] M. S. Chen, D. Kumar, C. W. Yi, D. W. Goodman, *Science* **2005**, *310*, 291–293.
- [20] H. J. Gotsis, I. Rivalta, E. Sicilia, N. Russo, *Chem. Phys. Lett.* **2009**, *468*, 162–165.
- [21] W. D. Provine, P. L. Mills, J. J. Lerou, *Stud. Surf. Sci. Catal.* **1996**, *101*, 191–200.
- [22] E. A. Crathorne, D. MacGowan, S. R. Morris, *J. Catal.* **1994**, *149*, 254–267.
- [23] S. Nakamura, T. Yasui, *J. Catal.* **1970**, *17*, 366–374.
- [24] I. I. Moiseev, T. A. Stromnova, M. N. Vargaftig, G. J. Mazo, *Chem. Comm.* **1978**, *956*, 27.
- [25] B. Samanos, P. Boutry, R. Montarnal, *J. Catal.* **1971**, *23*, 19–30.
- [26] S. A. H. Zaidi, *Appl. Catal.* **1988**, *38*, 353–358.
- [27] R. van Helden, C. F. Kohll, D. Medema, G. Verberg, T. Jonkhoff, *Recl. Trav. Chim. Pay. B.* **1968**, *87*, 961–991.
- [28] S. Winstein, J. McCaskie, H.-B. Lee, P. M. Henry, *J. Am. Chem. Soc.* **1976**, *98*, 6913–6918.
- [29] M. Neurock, W. D. Provine, D. A. Dixon, G. W. Coulston, J. J. Lerou, R. A. van Santen, *Chem. Eng. Sci.* **1996**, *51*, 1691–1699.

- [30] D. Stacchiola, F. Calaza, L. Burkholder, A. W. Schwabacher, M. Neurock, W. T. Tysoe, *Angew. Chem. Int. Edit.* **2005**, *44*, 4572–7574.
- [31] R. Abel, G. Prauser, H. Tiltscher, *Chem. Eng. Technol.* **1994**, *17*, 112–118.
- [32] N. Macleod, J. M. Keel, R. M. Lambert, *Appl. Catal. A-Gen.* **2004**, *261*, 37–46.
- [33] Y. F. Han, D. Kumar, D. W. Goodman, *J. Catal.* **2005**, *230*, 353–358.
- [34] D. Kumar, Y. F. Han, M. S. Chen, D. W. Goodman, *Catal. Lett.* **2006**, *106*, 1–5.
- [35] Q. Smejkal, D. Linke, U. Bentrup, M. M. Pohl, H. Berndt, M. Baerns, A. Brueckner, *Appl. Catal. A-Gen.* **2004**, *268*, 67–76.
- [36] Y. F. Han, D. Kumar, C. Sivadinarayana, D. W. Goodman, *J. Catal.* **2004**, *224*, 60–68.
- [37] D. Stacchiola, F. Calaza, L. Burkholder, W. T. Tysoe, *J. Am. Chem. Soc.* **2004**, *126*, 15384–15385.
- [38] X. C. Guo, R. J. Madix, *J. Am. Chem. Soc.* **1995**, *117*, 5523–5530.
- [39] D. Kumar, Y. F. Han, D. W. Goodman, *Top. Catal.* **2007**, *46*, 169–174.
- [40] M. O. Coppens, G. F. Froment, *Chem. Eng. Sci.* **1994**, *49*, 4897–4907.
- [41] W. J. Bartley (Union Carbide Chemicals & Plastics Technology Corporation), US 5,179,056, **1993**.
- [42] W. J. Bartley (Union Carbide Chemicals & Plastics Technology Corporation), US 5,179,057, **1993**.
- [43] A. Hagemeyer, A. Kyriopoulos, S. Obermaier (Inventor status recognised after publication; Süd-Chemie AG), DE 102007025324 A1, **2008**.
- [44] A. Hagemeyer, A. Kyriopoulos, S. Obermaier (Inventor status recognised after publication; Süd-Chemie AG), WO 08151731 A1, **2008**.
- [45] T. Tacke, U. Ohlrogge, H. Mueller, H. G. J. Lansink-Rotgerink, H. Krause, F. P. Daly (Degussa-Hüls Aktiengesellschaft), EP 1106247 B1, **2003**.
- [46] A. K. Khanmamedova (Saudi Basic Industries Corporation), US 6,420,308 B1, **2002**.

- [47] A. K. Khanmamedova (Saudi Basic Industries Corporation), US 6,825,149 B2, **2004**.
- [48] A. K. Khanmamedova, B. Li, R. J. Bates, Y. K. Yin (Saudi Basic Industries Corporation), US 6,794,332 B2, **2004**.
- [49] S. C. Chen, Y. L. Jong, F. S. Lin, P. F. Jang (Dairen Chemical Corporation), EP 1205246 B1, **2002**.
- [50] W. J. Bartley (Union Carbide Chemicals & Plastics Technology Corporation), US 5,189,004, **1993**.
- [51] A. Hagemeyer, A. Kyriopoulos, G. Mestl, P. Scheck (Süd-Chemie AG), DE 102007025444 A1, **2008**.
- [52] A. Hagemeyer, A. Kyriopoulos, G. Mestl, P. Scheck (Süd-Chemie AG), WO 08145389 A2, **2008**.
- [53] A. Hagemeyer, A. Kyriopoulos, G. Mestl, P. Scheck (Süd-Chemie AG), German patent application pending.
- [54] E. Haberkorn, K. H. Hable, A. Hagemeyer, R. Kerscher, A. Kyriopoulos, P. Scheck (Süd-Chemie AG), German patent application pending.
- [55] F. P. Daly, H. Krause, H. G. J. Lansink-Rotgerink, H. Mueller, U. Ohlrogge, T. Tacke (Degussa-Hüls Aktiengesellschaft), US 5,808,136, **1998**.
- [56] H. Debellefontaine, Besombes-Vailhé, *J. Chim. Phys.* **1978**, *75*, 801–809.
- [57] A. Hagemeyer, A. Kyriopoulos, G. Mestl, S. Neumann, P. Scheck (Süd-Chemie AG), German patent application pending.
- [58] M. I. Temkin, N. V. Kul'kova, *Kin. i Kat.* **1969**, *10*, 461–463.
- [59] N. Arvindan, H. S. Bergh, V. Sokolovskii, V. Wong (Symyx Technologies Inc), WO 06083437 A2, **2006**.
- [60] T. Schulz, A. Kyriopoulos, M. Lucas, P. Claus in *42. Jahrestreffen Deutscher Katalytiker*, Weimar, Germany, **2009**, 101–102.
- [61] T. Schulz, A. Kyriopoulos, M. Lucas, A. Hagemeyer, G. Mestl, P. Claus in *Jahrestreffen Reaktionstechnik 2009*, Würzburg, Germany, **2009**, 32–33.

- [62] T. Schulz, A. Kyriopoulos, M. Lucas, A. Hagemeyer, G. Mestl, P. Claus in *EuropaCat IX*, Salamanca, Spain, **2009**, 258.
- [63] P. Claus, R. Gunkel, M. Lucas, T. Schulz, G. Arasteh, A. Hagemeyer, G. Mestl (TU Darmstadt, Süd-Chemie AG), Utility model, **2009**.
- [64] J. F. LePage, *Handbook of Heterogeneous Catalysis, Vol. 1* (Eds.: G. Ertl, H. Knözinger, J. Weitkamp), Wiley-VCH Verlag GmbH & Co. KGaA, **1997**, 49–53.
- [65] A. Hagemeyer, J. Han, D. M. Lowe, V. Sokolovskii, L. E. Wade, T. Wang, V. Wong (Celanese International Corporation), WO 05061107 A1, **2005**.
- [66] J. Han, B. Kimmich, Y. Liu, I. Nicolau, L. E. Wade, T. Wang (Celanese International Corporation), WO 05065820 A1, **2005**.
- [67] B. Herzog, A. Schäfer, K.-H. Renkel, T. Wang (Celanese Chemicals Europe), WO 00066261 A1, **2000**.
- [68] E. P. Barrett, L. G. Joyner, P. P. Halenda, *J. Am. Chem. Soc.* **1951**, *73*, 373–380.
- [69] *CRC Handbook of Chemistry and Physics* (Ed.: D. R. Lide), CRC Press/Taylor and Francis, 89th ed., **2008**, 10–204.
- [70] G. Arasteh, M. D. Thesis, Universität Karlsruhe, **2009**.
- [71] C. H. Bartholomew, *Appl. Catal. A-Gen.* **2001**, *212*, 17–60.
- [72] F. Moreau, C. B. Geoffrey, *Catal. Today* **2007**, *122*, 260–265.
- [73] G. Bergeret, P. Gallezot, *Handbook of Heterogeneous Catalysis, Vol. 2* (Eds.: G. Ertl, H. Knözinger, J. Weitkamp), Wiley-VCH Verlag GmbH & Co. KGaA, **1997**, 738–765.
- [74] S. Brunauer, P. H. Emmett, E. Teller, *J. Am. Chem. Soc.* **1938**, *60*, 309–319.
- [75] V. Narayana Kalevaru, A. Benhmid, J. Radnik, M.-M. Pohl, U. Bentrup, A. Martin, *J. Catal.* **2007**, *246*, 399–412.
- [76] A. Palermo, J. P. H. Vazquez, A. F. Lee, M. S. Tikhov, R. M. Lambert, *J. Catal.* **1998**, *177*, 259–266.

- [77] A. K. Datye, *Handbook of Heterogeneous Catalysis, Vol. 2* (Eds.: G. Ertl, H. Knözinger, J. Weitkamp), Wiley-VCH Verlag GmbH & Co. KGaA, **1997**, 493–512.
- [78] M. Newville, *J. Synchrotron Rad.* **2001**, *8*, 96–100.
- [79] M. Newville, *J. Synchrotron Rad.* **2001**, *8*, 322–324.
- [80] M. Vaarkamp, D. C. Koningsberger, *Handbook of Heterogeneous Catalysis, Vol. 2* (Eds.: G. Ertl, H. Knözinger, J. Weitkamp), Wiley-VCH Verlag GmbH & Co. KGaA, **1997**, 475–493.
- [81] D. E. Sayers, B. A. Bunker, *X-ray Absorption: Principles, Applications, Techniques of EXAFS, SEXAFS and XANES* (Eds.: D. Koningsberger, R. Prins), Wiley-VCH Verlag GmbH & Co. KGaA, **1988**, 211–253.
- [82] D. E. Sayers, E. A. Stern, F. W. Lytle, *Phys. Rev. Lett.* **1971**, *27*, 1204–1207.
- [83] K. Okumura, M. Niwa, *Catal. Surv. Jpn.* **2002**, *5*, 121–126.
- [84] A. Morlang, PhD thesis, Technische Universität Darmstadt, **2004**.
- [85] B. J. Kip, F. B. M. Duivenvoorden, D. C. Koningsberger, R. Prins, *J. Catal.* **1987**, *105*, 26–38.
- [86] J. W. Niemantsverdriet, *Spectroscopy in Catalysis: An Introduction*, Wiley-VCH Verlag GmbH & Co. KGaA, **2007**, 147–177.
- [87] M. Vaarkamp, J. C. Linders, D. C. Koningsberger, *Physica B* **1995**, *208/209*, 159–160.
- [88] S. I. Zabinsky, J. J. Rehr, A. L. Ankudinov, R. C. Albers, M. J. Eller, *Phys. Rev. B* **1995**, *52*, 2995–3009.
- [89] C. Roth, N. Benker, M. Mazurek, F. Scheiba, H. Fuess, *Appl. Catal. A-Gen.* **2007**, *319*, 81–90.
- [90] H. Nitani, T. Nakagawa, M. Yuya, T. Ono, S. Emura, S. Seino, K. Okitsu, Y. Mizukoshi, T. A. Yamamoto, *Materials Science* **2004**, 165.
- [91] *Inorganic Crystal Structure Database* **2009**, 64914.
- [92] *Inorganic Crystal Structure Database* **2009**, 52249.

- [93] M. M. Pohl, J. Radnik, M. Schneider, U. Bentrup, D. Linke, A. Brueckner, E. Ferguson, *J. Catal.* **2009**, *262*, 314–323.
- [94] Z. Zhang (Akzo Nobel N.V.), US 5,721,189, **1998**.
- [95] Z. Zhang (Akzo Nobel N.V.), US 5,962,366, **1999**.
- [96] S. N. Reifsnyder, H. H. Lamb, *J. Phys. Chem. B* **1999**, *103*, 321–329.
- [97] N. Toshima, M. Harada, Y. Yamazaki, K. Asakura, *J. Phys. Chem.* **1992**, *96*, 9927–9933.
- [98] M. Harada, K. Asakura, N. Toshima, *J. Phys. Chem.* **1993**, *97*, 5103–5114.
- [99] R. J. Davis, M. Boudart, *J. Phys. Chem.* **1994**, *98*, 5471–5477.
- [100] S. Marx, A. Baiker, *J. Phys. Chem. C* **2009**, *113*, 6191–6201.
- [101] V. Croze, F. Ettingshausen, J. Melke, M. Soehn, D. Suermer, C. Roth, *J. Appl. Electrochem.* **2009**, *39*, accepted (DOI: 10.1007/s10800-009-9919-x).
- [102] W. R. Tyson, W. A. Miller, *Surf. Sci.* **1977**, *62*, 267–276.
- [103] L. Z. Mezey, J. Giber, *Jpn. J. Appl. Phys.* **1982**, *11*, 1569–1571.
- [104] C. W. Yi, K. Luo, T. Wei, D. W. Goodman, *J. Phys. Chem. B* **2005**, *109*, 18535–18540.
- [105] Z. Li, O. Furlong, F. Calaza, L. Burkholder, H. C. Poon, D. Saldin, W. T. Tysoe, *Surf. Sci.* **2008**, *602*, 1084–1091.
- [106] P. A. Crozier, P. Claus, *Microscopy and Microanalysis* (Eds.: G. W. Bailey, J. M. Corbett, R. V. W. Dimlich, J. R. Michael, N. J. Zaluzec), San Francisco Press, **1996**, 224–225.
- [107] J. Banhart, *Phys. Rev. B* **1996**, *53*, 7128–7133.
- [108] M. Bron, E. Kondratenko, A. Trunschke, P. Claus, *Z. Phys. Chem.* **2004**, *218*, 405–423.

# Appendix A

## Sample of chromatogram and calculation for conversion, selectivity and space time yield

Figure A.1 shows a representative gas chromatogram (GC 7890b, Agilent) after VAM formation. Detailed information of this GC method is given elsewhere [70].

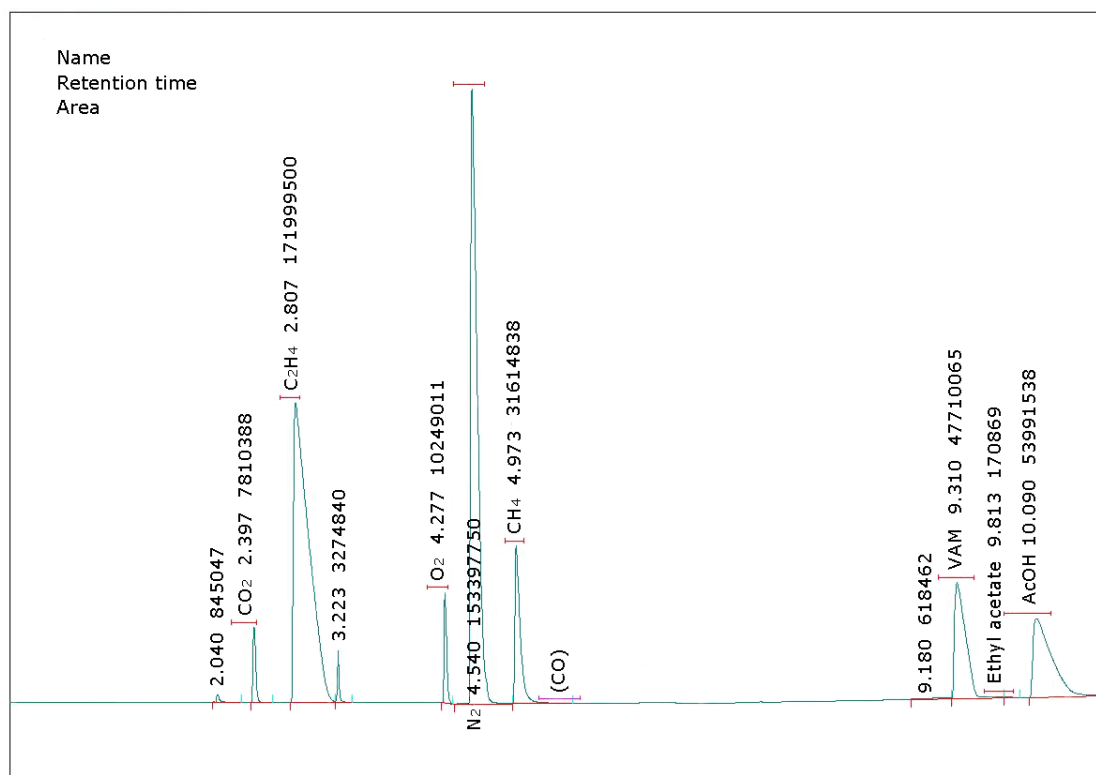


Figure A.1: Exemplary chromatogram of the detected components for the VAM reaction.

The chromatogram displays the separation of the following components detected during this reaction: CO<sub>2</sub>, C<sub>2</sub>H<sub>4</sub>, O<sub>2</sub>, N<sub>2</sub>, CH<sub>4</sub>, CO, VAM, ethyl acetate and acetic acid. Based on the resulting peak areas of CO<sub>2</sub>, O<sub>2</sub>, CH<sub>4</sub> and VAM, summarised in table (tab. A.1), conversion ( $C$ ), selectivity ( $S$ ) and space time yield ( $STY$ ) were calculated as shown below. GC results of the inert material used as reference are labelled with index 0.

Table A.1: GC peak areas measured for VAM catalyst *EX6315* and for the inert material.

	O <sub>2</sub> area	CH <sub>4</sub> area	VAM area	CO <sub>2</sub> area
VAM catalyst	9293075	13083096	33751352	7233308
KA 160 support	18132049	12684280	-	4576548

The next step was to calculate the following ratios derived from the previous GC peak areas, normalised to methane (tab. A.2).

Table A.2: GC peak areas normalised to methane.

	O <sub>2</sub> /CH <sub>4</sub>	VAM/CH <sub>4</sub>	CO <sub>2</sub> /CH <sub>4</sub>
VAM catalyst	0.71	2.58	0.55
KA 160 support	1.43	-	0.36

Based on the equations mentioned in section 3.5, the results for  $C_{O_2}$ ,  $S_{VAM}$  and  $STY_{VAM}$  are as follows:

$$C_{O_2} = \frac{1.43 - 0.71}{1.43} = 50.31 \%$$

$$C_{CO_2} = \frac{c_{CO_2, methane} - c_{CO_2, methane}^0}{c_{CO_2, methane}^0} = \frac{0.55 - 0.36}{0.36} = 53.24 \%$$

$$S_{VAM} = \frac{b}{b + a} = \frac{80.69}{80.69 + 3.99} = 95.29 \%$$

$$\begin{aligned} \text{with } b &= \frac{1}{2} \cdot F_{CO_2} \cdot \left( \frac{100 + C_{CO_2}}{100} - 1 \right) \\ &= \frac{1}{2} \cdot 15 \text{ NmLmin}^{-1} \cdot (1.5323 - 1) = 3.99 \text{ NmLmin}^{-1} \end{aligned}$$

$$\begin{aligned} \text{and } a &= 2 \left( F_{O_2} \cdot \frac{C_{O_2}}{100} - 3b \right) \\ &= 2 (104 \cdot 0.50 - 3 \cdot 3.99) \text{ NmLmin}^{-1} = 80.69 \text{ NmLmin}^{-1} \end{aligned}$$

$$STY_{VAM} = 2.58 \cdot 70 \text{ NmLmin}^{-1} \cdot 0.054 \cdot \frac{86.09 \text{ g mol}^{-1}}{22.4 \text{ L mol}^{-1}} \cdot \frac{6431}{32} \text{ L}^{-1} = 451 \text{ g}_{VAM} \text{ Lh}^{-1}$$

# Appendix B

Comparison of VAM selectivity for different catalysts to the benchmark  $B$

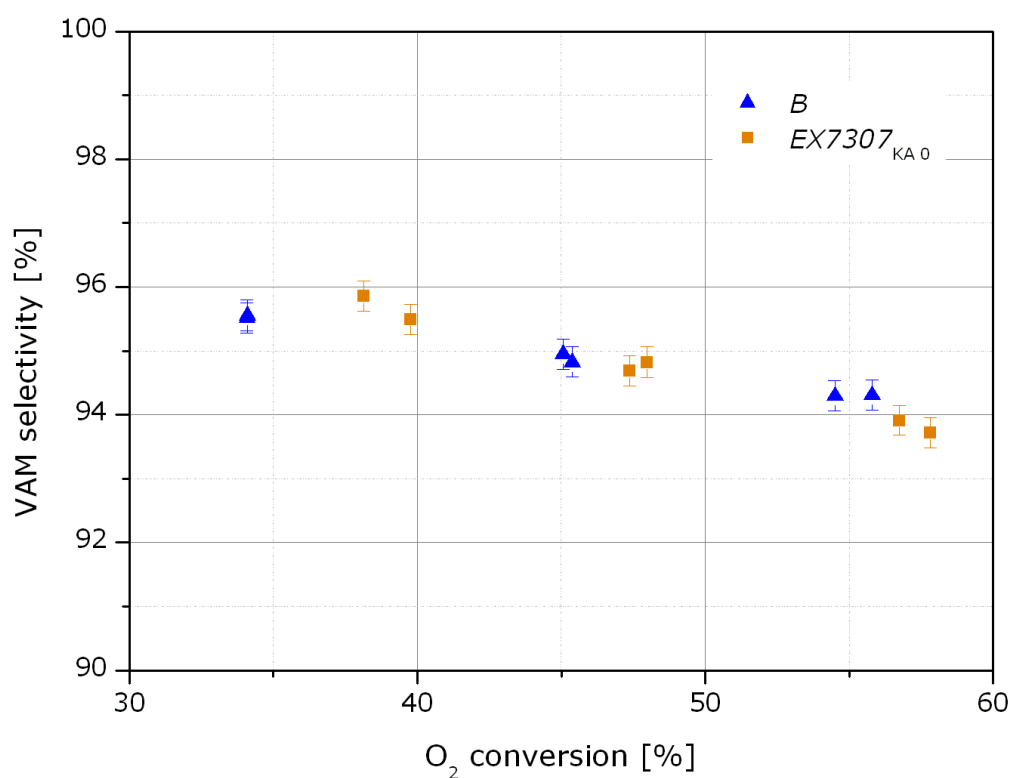


Figure B.1: Comparison of selectivity between the VAM catalyst  $EX7307$  based on the KA 0 carrier ( $BET = 106\text{ m}^2\text{g}^{-1}$ ) and the reference  $B$  synthesised with the higher surface area support KA 160 ( $BET = 161\text{ m}^2\text{g}^{-1}$ ).

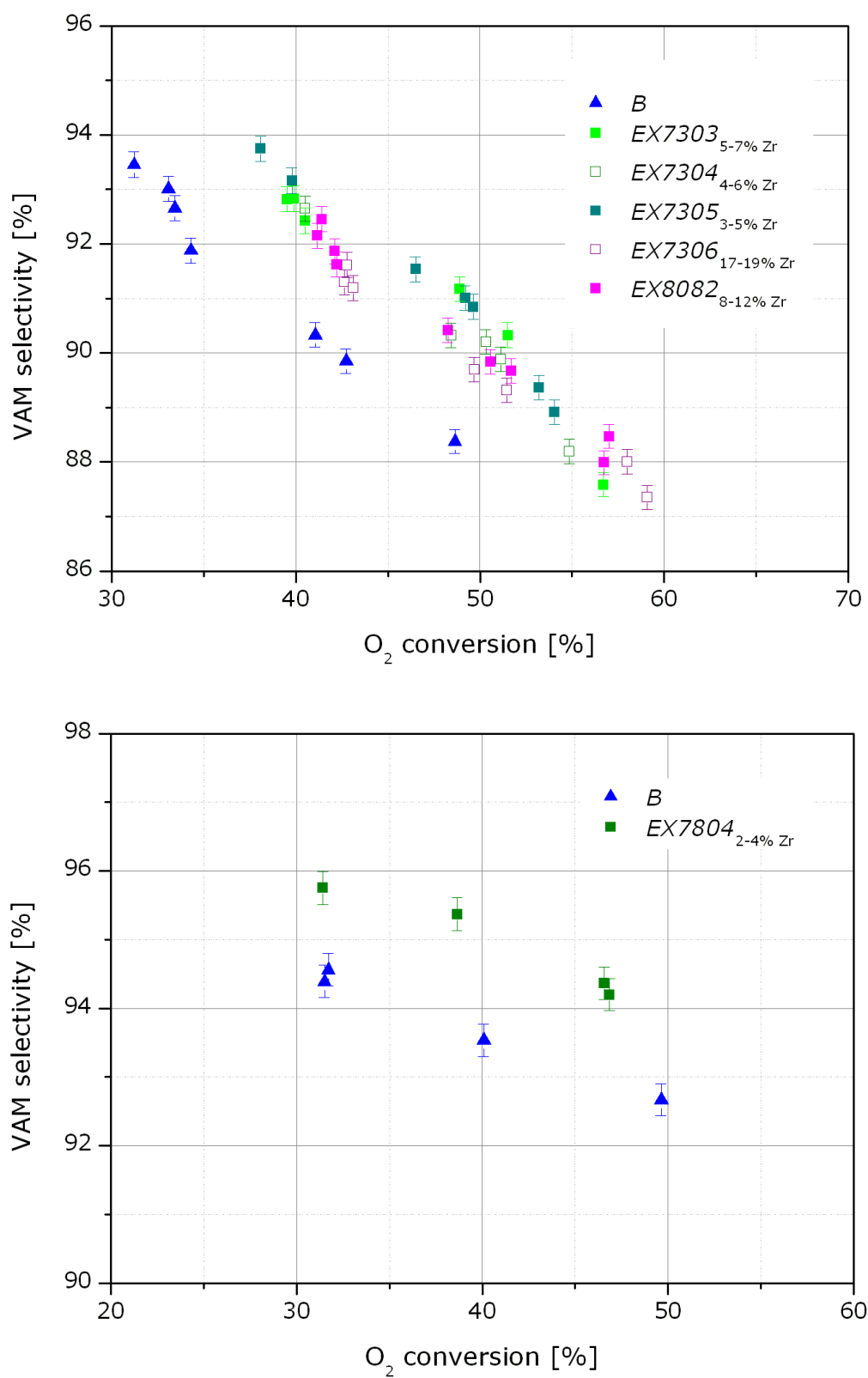


Figure B.2: VAM selectivity for several catalysts synthesised with different KA-Zr carriers compared to the performance of benchmark *B*.

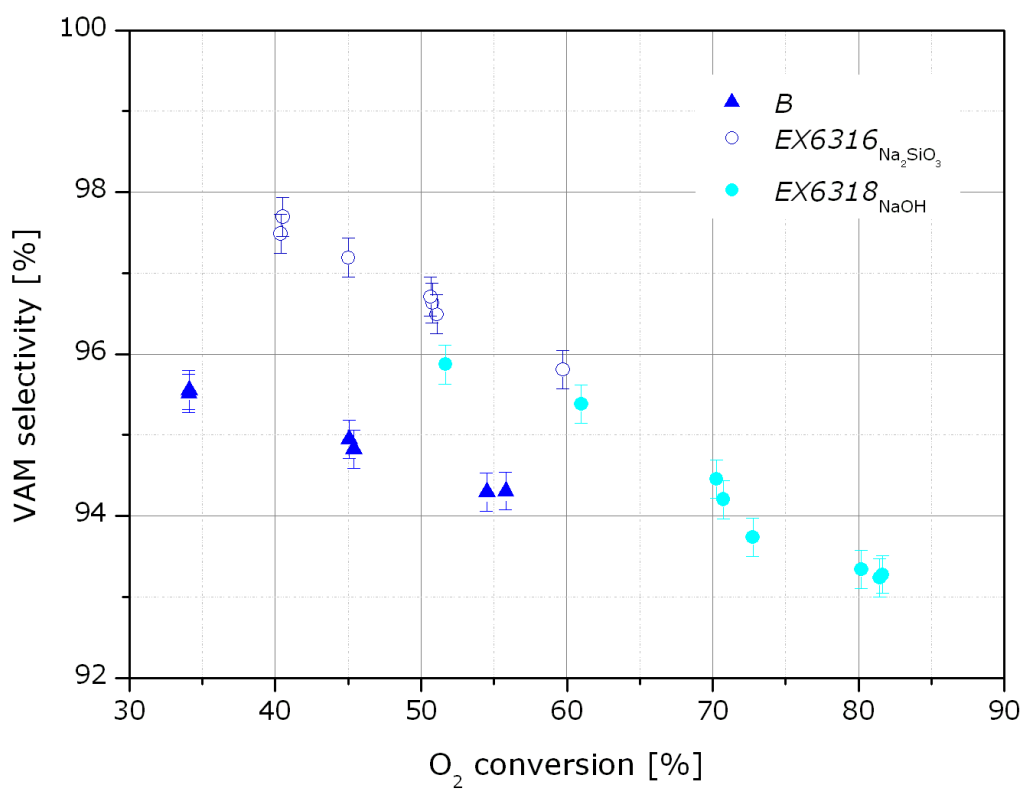


Figure B.3: Comparison of selectivity for VAM catalysts precipitated with NaOH or Na<sub>2</sub>SiO<sub>3</sub> using GPR during synthesis. The selectivity data of the benchmark *B* is also shown.

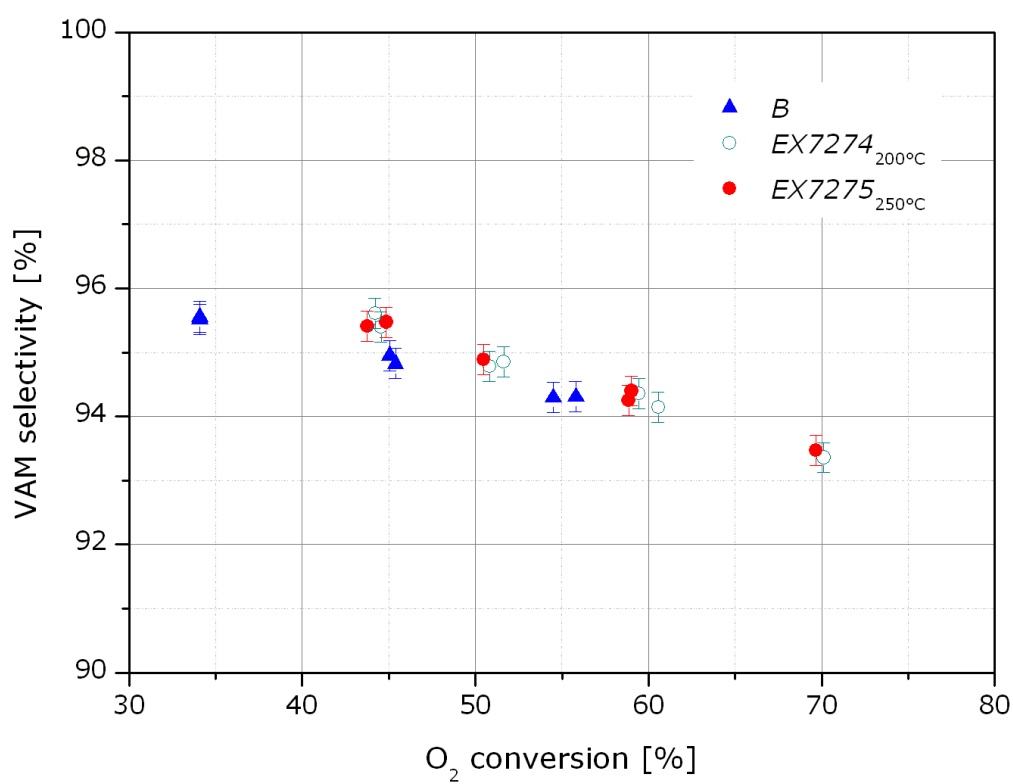
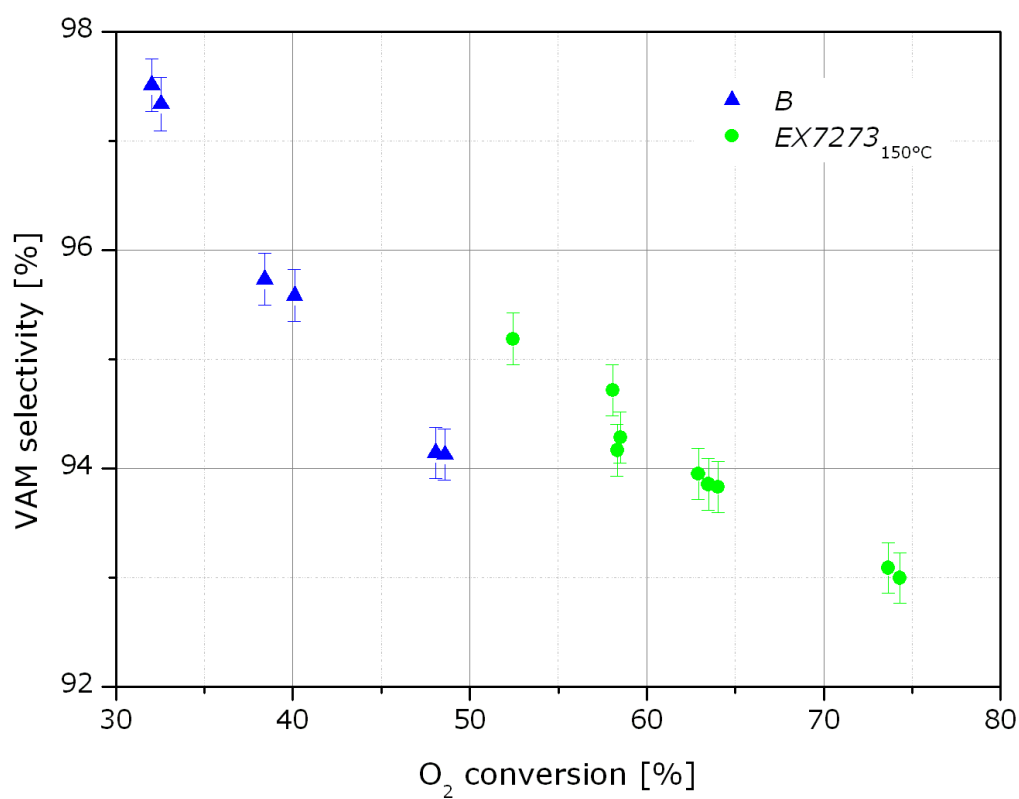


Figure B.4: VAM selectivity of catalysts reduced at different temperatures in gas phase compared to the corresponding data of benchmark *B*.

# Appendix C

Comparison of VAM space time yield for different catalysts to the benchmark  $B$

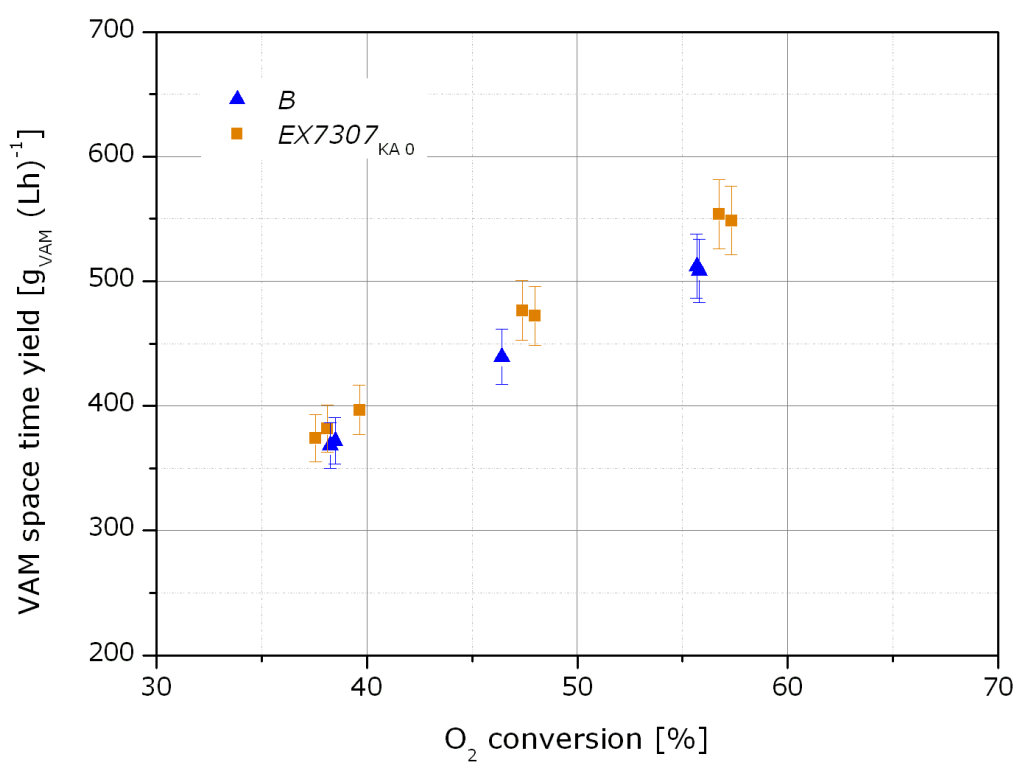


Figure C.1: Comparison of activity between the VAM catalyst  $EX7307$  based on KA 0 carrier and the reference  $B$ .

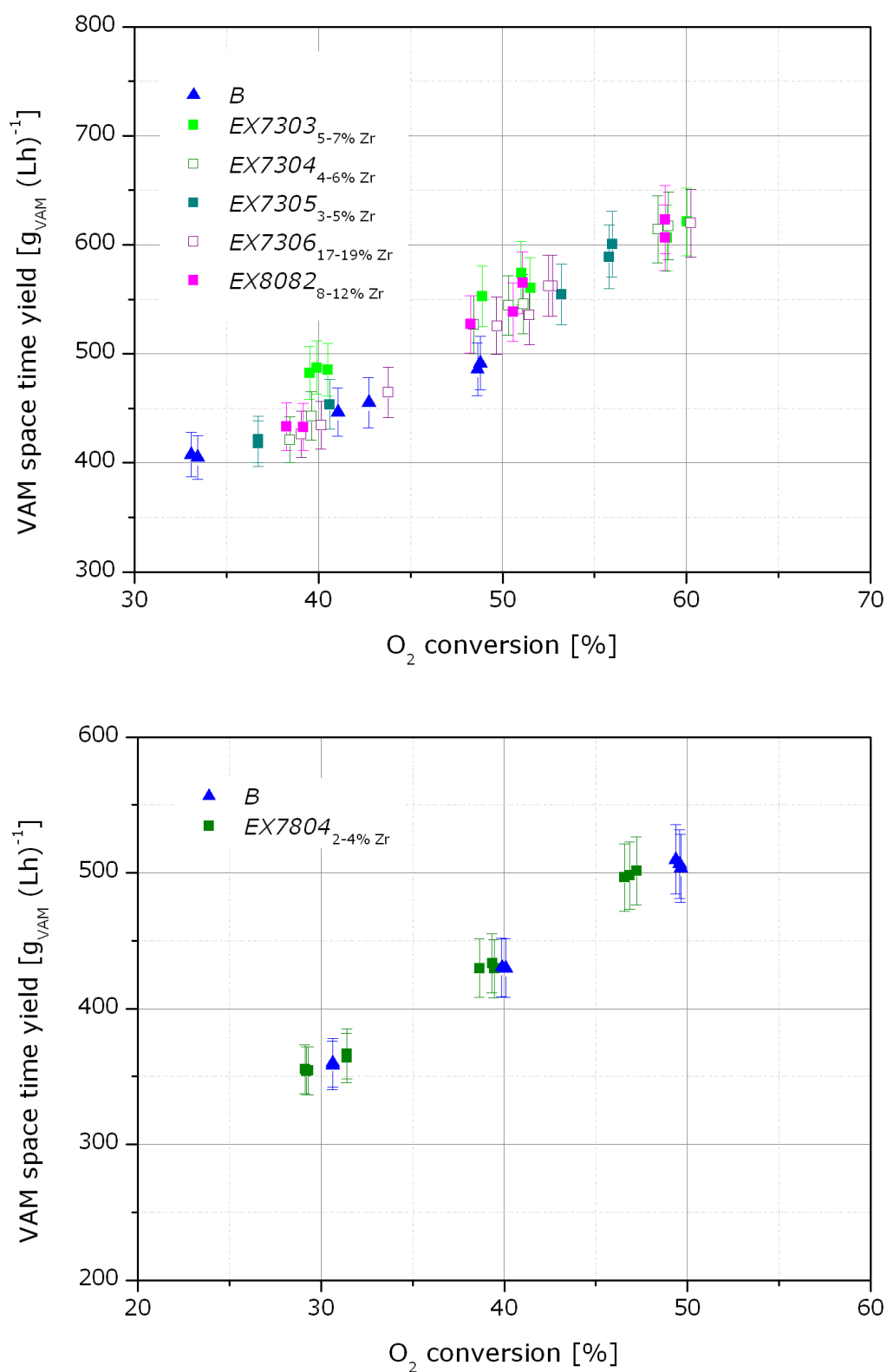


Figure C.2: VAM *STY* for catalysts synthesised with different KA-Zr carriers compared to the performance of benchmark *B*.

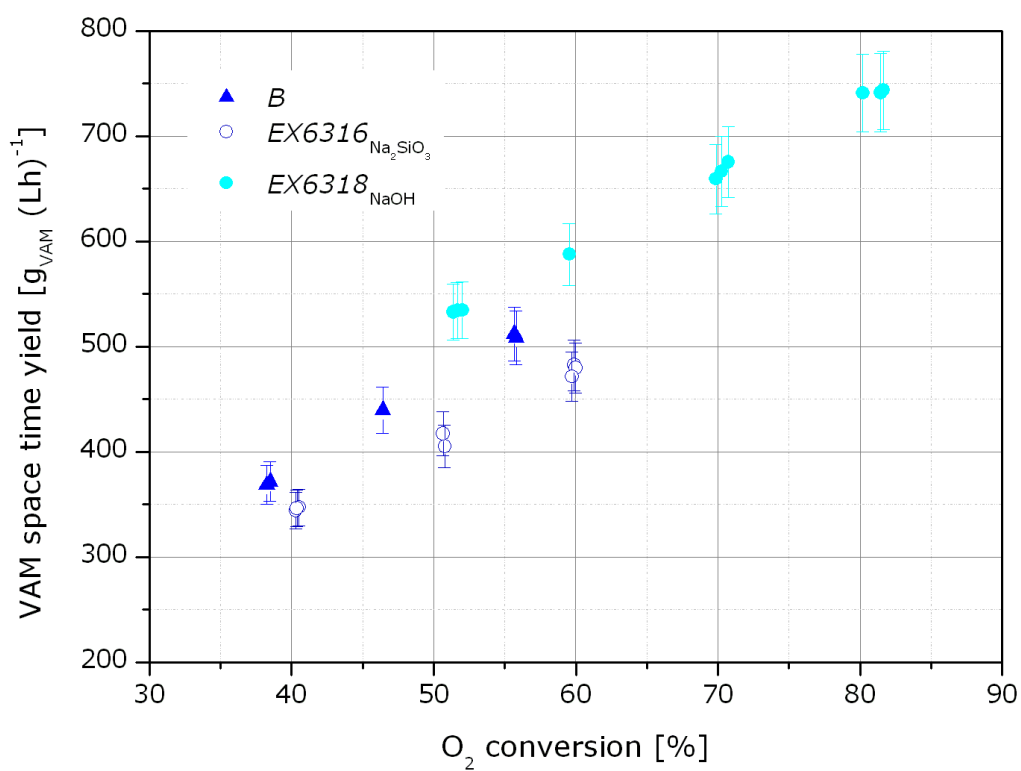


Figure C.3: Comparison of activity for VAM catalysts precipitated with NaOH or Na<sub>2</sub>SiO<sub>3</sub> using GPR during synthesis. The activity data of the benchmark *B* is also shown.

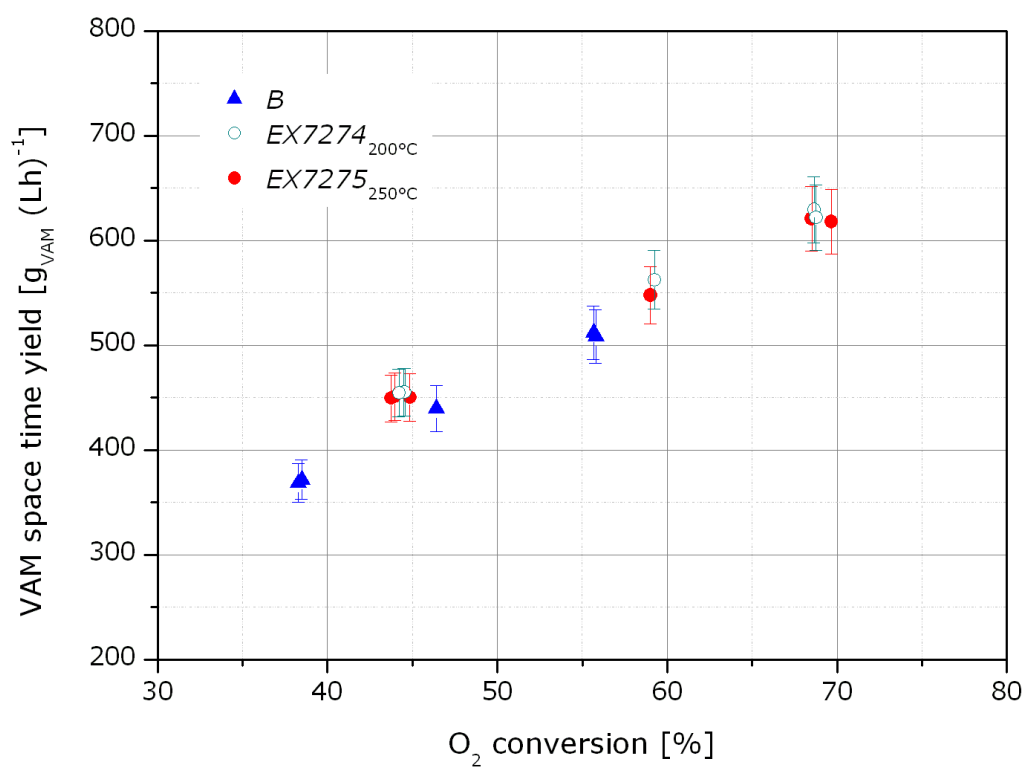
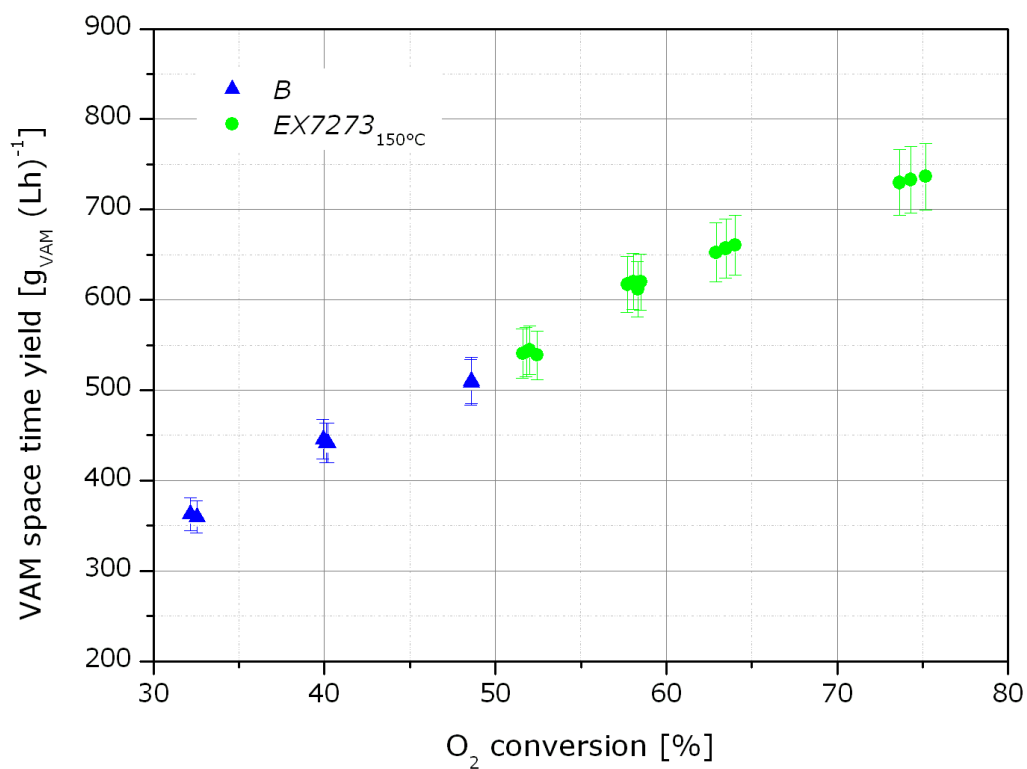


Figure C.4: VAM *STY* comparison of catalysts reduced at different temperatures in gas phase to the corresponding data of benchmark *B*.

Alice Kyriopoulos  
Otto-Mair-Ring 12  
83607 Holzkirchen

19.10.2009

### Eidesstattliche Erklärung

Ich erkläre hiermit an Eides Statt, dass ich meine Dissertation selbständig und nur mit den angegebenen Hilfsmitteln angefertigt habe.

Alice Kyriopoulos  
Otto-Mair-Ring 12  
83607 Holzkirchen

19.10.2009

### Erklärung

Ich erkläre hiermit, noch keinen Promotionsversuch unternommen zu haben.

# Curriculum Vitae

## Personal Data

Name: Alice Iwona Kyriopoulos

Born on: August 10, 1981 in Darmstadt

## Academic education

12/06 - 12/09 *PhD thesis*

Ernst-Berl-Institute for Technical and Macromolecular Chemistry

Supervisor: Prof. Dr. Peter Claus

Subject: "Development of high performance vinyl acetate monomer catalysts"

01/06 - 07/06 *Diploma*

Eduard-Zintl-Institute for Inorganic and Physical Chemistry

Supervisor: Prof. Dr. Rolf Schäfer

Subject: "Improvement of an established molecular beam apparatus used to analyse the electronic polarisability of heavy  $\text{Sn}_N$  clusters"

07/03 - 12/05 Advanced studies in Chemistry at the Technische Universität Darmstadt

09/02 - 06/03 Studies abroad at University of Bath, United Kingdom

10/00 - 09/02 Basic studies in Chemistry at the Technische Universität Darmstadt

07/91 - 06/00 Edith-Stein-Schule, Darmstadt

## Professional experience

01/07 - 07/09 Süd-Chemie AG, Heufeld

Department: Research and development oxidation catalysis

07/09 - to date Süd-Chemie AG, Munich

Department: Product management catalytic technologies

Darmstadt, 19.10.2009